A Solid-State Single Photon Source Based on Color Centers in Diamond

Dissertation at the Department of Physics
at the
Ludwig-Maximilians-Universität München

Chunlang Wang

München, June 08, 2007

TO MY PARENTS
AND FEI WANG
FOR THEIR ENCOURAGEMENT AND UNDERSTANDING

Zusammenfassung

Eine zuverlässige, effiziente und kostengünstige Einzelphotonenquelle ist eine wichtige Komponente in vielen Anwendungen der Quanteninformationsverarbeitung und Quantenkommunikation. Einzelphotonenquellen wurden schon in Experimenten der Quantenkryptographie eingesetzt und haben Vorteile gegenüber abgeschwächten Laserpulsen gezeigt. Eine Einzelphotonenquelle ist auch eine der notwendigen Voraussetzungen für einen optischen Quantencomputer nach dem Vorschlag von Knill, Laflamme und Milburn. Darüber hinaus sind einzelne Photonen der ideale Kandidat um das Grundprinzip der Quantenmechanik zu demonstrieren. Deshalb ist eine Einzelphotonenquelle auch wünschenswert für bildungszwecke. Das in dieser Arbeit untersuchte Konzept für eine Einzelphotonenquelle basiert auf Farbzentren im Diamant. Farbzentren sind eine attraktive Wahl für die praktischen Anwendungen wegen des relativ geringen experimentellen Aufwands.

In dieser Arbeit wurde das SiV (silicon vacancy) Zentrum ausführlich untersucht, weil es mehrere vorteilhafte Eigenschaften hat, z.B. das schmale Spektrum und die kurze Lumineszenzlebensdauer. Die SiV-Zentren wurden durch Silizium-Ionenimplantation im IIa-Diamant erzeugt. Einzelne SiV-Zentren wurden durch ein konfokales Mikroskop optisch adressiert. Die Emission einzelner Photonen wurde durch die Messung der Intensitätskorrelationsfunktion nachgewiesen. Allerdings zeigt ein einzelnes SiV-Zentrum eine weitaus niedrigere Photonenemissionsrate als erwartet. Das liegt auf der einen Seite an einer schlechten Quantenausbeute wegen nicht-strahlender Übergänge. Andererseits existiert ein zusätzliches metastabiles Niveau im Energieschema des SiV-Zentrums. Das metastabile Niveau wurde als der positive Ladungszustand identifiziert. Durch Manipulation des Fermi-Niveaus im Diamant durch Stickstoff-Ionenimplantation kann die Population des positiven Ladungszustands eliminiert werden. Außer dem SiV-Zentrum wurden mehrere unbekannte einzelne Farbzentren gefunden und charakterisiert.

Eine andere wichtige Aufgabe ist das effiziente Aufsammeln der Fluoreszenz einzelner Quantenemitter. In dieser Arbeit wurden zwei Methoden untersucht. Mit einer direkt auf die Probe gesetzten Diamant Halbkugellinse wurde eine Erhöhung der Aufsammeleffizienz um einen Faktor 5 erreicht. Wenn die Größe der Kristalle deutlich kleiner als die Wellenlänge der Fluoreszenz ist, tritt keine Brechung auf dem Übergang zwischen Diamant und Luft auf. Deswegen wurde einzelne SiV-Zentren auch in Diamantnanokristallen untersucht. Dabei wurde stärkere Fluoreszenzintensität observiert.

Contents

Chapter 1

Introduction

The term "single-photon state" denotes an electromagnetic field containing only one photon. Behind this quite simple notation there is actually a highly odd and nonclassical state of light, but for the purpose of an introduction it is convenient to image a single-photon state as a situation in which exactly one particle, the photon, exists for a certain time in an experimental apparatus.

The generation of single photons is of fundamental interest for the understanding of the nature of light, since a single-photon state exhibits some properties which can not be explained by classical theories. Furthermore, it is also crucial for many applications in quantum information processing [1, 2]. In recent years, considerable efforts have been made to develop single photon sources which meet requirements of the different applications, e.g. spontaneous emission of single quantum systems [3, 4, 5, 6, 7], coherent manipulations of atomic states [8, 9] or parametric down conversion [10, 11], but they all have different assets and drawbacks and a satisfactory solution for single photon generation is still not found. This thesis is devoted to the approach based on fluorescent defects (color centers) in diamond, which have some suitable properties for practical applications e.g. quantum cryptography.

1.1 Applications of single photons

The idea to transfer information by light is as old as the history of mankind. Whether it is the fire on watchtowers of the Great Wall in ancient China or laser pulses in today's optical fiber, light signals with macroscopical intensity are employed. Such signals are in principle measurable by everyone, therefore the encoded information is also accessible for unauthorized parties. The situation changes dramatically, if the information is carried by single photons.

In quantum mechanics the uncertainty principle states that the quantities of two canonical conjugate observables, e.g. the polarization of a photon in the rectilinear (vertical and horizontal) and the diagonal ($+45°$ and $-45°$) basis, can never be precisely measured simultaneously. Therefore, when measuring the polarization of a photon, the choice of the measurement basis affects all subsequent measurements. Using a pair of orthogonal states, 1 and 0 can be encoded in a single photon. If two conjugate pairs of orthogonal states are chosen randomly during the encoding, the measurements of an eavesdropper will cause perturbations to the photonic states with a probability of 50%. Therefore the presence of the eavesdropper can be detected. This is the basic idea of the BB84 protocol of quantum cryptography, which promises unconditional security in communication and thus has attracted great interest in recent years.

Nowadays, commercial quantum cryptography systems are already available, but instead of "real" single photons attenuated laser pulses are commonly used. Since the photon number in laser pulses follows the poissonian distribution, there is always a non-vanishing probability to find two or more photons within a laser pulse, even though the average photon number per pulse is set far below unity. This gives rise to a potentially important security leakage known as photon number splitting attack [12]. For a quantum channel with high loss it is possible for an eavesdropper to share almost all the information without being detected. Therefore the implementations of quantum cryptography with attenuated laser pulses are restricted by distance.

There are ingenious ways to overcome this obstacle in practical quantum cryptography by employing nonorthogonal states in additional degrees of freedom, e.g. the average photon number. Those ideas lead to the decoy state protocol [13, 14]. Recently an implementation of the decoy state protocol in free space over 144 km has been demonstrated [15]. Figure 1.1 shows the theoretical prediction of secure bit transfer rate R against loss in a quantum channel η for different protocols and experimental results with the decoy state protocol. The decoy state protocol has indeed significant advantages over ordinary quantum cryptography protocols with attenuated laser pulses, but the optimum performance can be reached only using a real single photon source.

Single photon sources have already been tested in a quantum cryptography experiments [16, 17], but in order to compete with the established systems with attenuated laser pulses, a higher single photon generation rate, a more compact setup and better control of the emitted photons are required.

Single photons are not only able to transfer quantum information, they can also be employed as quantum bits (qubits) for quantum computation, which promises large improvements in computational efficiency for certain
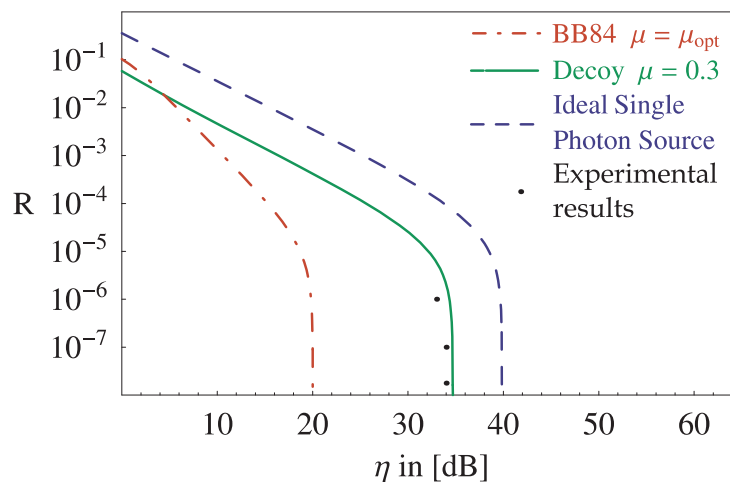
Figure 1.1: Theoretical predication of the secure bit transfer rate R in dependence of the loss in quantum channel η.

tasks. Examples include Shor's quantum algorithm for factoring large integers [18] and Grover's algorithm for accelerating combinatorial searches [19]. A qubit can be implemented using a single photon in two optical modes, such as horizontal and vertical polarization and single-qubit operations can be easily realized with linear optical components, e.g. beamsplitters and wave plates. But the main obstacle to a scalable optical quantum computer is the nonlinear coupling between optical modes. Nonlinear optical effects are usually weaker than the linear ones by several orders of magnitude, therefore it is technically extremely difficult to achieve sufficient strength of such couplings. However, in their seminal proposal E. Knill, R. Laflamme and G.J. Milburn showed that it is possible to construct an optical quantum computer efficiently with linear resources [2]. The main ingredient in the proposal is a single photon source, which is able to provide indistinguishable single photons on demand. To realize such a source is a very challenging task.

One of the most promising architectures for scalable quantum computation is not a purely optical quantum computer, but a quantum network with atoms, ions or solid state qubits as distant nodes for storing and processing of quantum information, and photons as flying qubits for communication among them [20]. For this purpose quantum information should be converted from photonic into atomic states. Therefore, the generation of single photons must take place in a coherent manner. The investigation of strong interaction between photon and atom has led to several nice concepts for single photon generation in recent years, which will be introduced in more detail in the

following section.

Quantum effects are particularly clearly to observe in optical systems with single photons, therefore single photons are of great importance for fundamental quantum optical experiments, e.g. the demonstration of complementarity [21]. Nowadays, such experiments are not spectacular breakthroughs any more, but they can be well used for educational purposes. Although quantum theory is now widely accepted, students still get into contact with it very late in their education. Due to its contra-intuitive nature, it is rather difficult to comprehend as well. If a simple and robust single photon source is available, quantum effects of light can be well demonstrated at every high school and made accessible to young students.

1.2 Implementations of a single photon source

The principle of single photon generation is quite simple, but it requires manipulations of individual quantum systems or strong nonlinear optical effects. Therefore, the implementations of a single photon source are often associated with considerable technical difficulties. While the early experiments were designed to demonstrate the nonclassical properties of light, recent research was often targeted on meeting the demands of the applications in the emerging field of quantum information processing.

The most intuitive approach is to isolate a single two-level system. The spontaneously emitted photons from the single two-level system are separated from each other by a characteristic time constant, because immediately after emission of one photon the two-level system is in the ground state and unable to emit a second photon.

In the pioneering work of H.J. Kimble *et al.* the resonance fluorescence from a sodium atomic beam was used to demonstrate photon antibunching, a signature of single photons (see §2.1) [3]. But in that experiment the number of illuminated atoms are still governed by poissonian statistics and therefore the atomic current had to be kept very low. A great progress was achieved when F. Diedrich *et al.* succeeded in storing a single ion in a Paul radio-frequency trap and measuring the second order correlation function of the fluorescence light [4]. With the continuing development of experimental techniques in quantum optics, such as the optical dipole trap and laser cooling, single neutral atoms could also be stored for several seconds [22, 23]. Nevertheless, the trap experiments must deal with micromotion in the trapping potential and the trapping time limitation. Additionally, the technical requirements such as ultra high vacuum and complex laser systems also form an obstacle for practical applications.

Systems with more promising properties for quantum cryptography were found in solids. Single dye molecules as dilute impurities in a crystalline host were first investigated at low temperature [5], and by careful selection of emitting molecules and the transparent host a room-temperature source was also realized [24]. A molecular-based single photon source needs less technical equipment than atomic systems, and is highly efficient due to the fluorescence quantum yields near unity and luminescence lifetime of only several nanoseconds. But the dye molecules suffer from low photostability. Even when protected by the liquid crystal host they can only tolerate continuous illumination for several hours. Besides that, the polarization of the single photons varies from one emitter to another.

Without additional molecules, some solids inherently possess point defects in the crystal lattice which behave optically like molecules. Those defects often determined the color of the crystals, and are therefore called color centers. Originally color centers were investigated in solid state physics only as properties of the material. They hadn't been associated with quantum optics, until the single photon character of the fluorescence from single NV (nitrogen-vacancy) centers in diamond was demonstrated in 2000 [7, 25]. The color centers in diamond excel in their unsurpassable photostability. Even after more than one week of operation, no changes were observed in emission characteristics of NV centers [7]. The extreme properties of diamond allow a very robust and simple setup at room temperature. Therefore, it was not by chance that the first single photon quantum cryptography experiment was done with NV centers. But the spectrum of NV centers shows very wide side bands at room temperature due to the coupling to phonons of diamond, and they have a luminescence lifetime of 12 ns which prevents a high repetition rate. Recently single color centers with narrow spectra and short luminescence lifetime have been reported [26, 27, 28, 29].

The impressing progresses in semiconductor physics in recent years have made it possible to perform quantum optical experiments on artificial systems. Single photon emission was demonstrated by controlled injection of carriers into a mesoscopic quantum well at low temperatures [30] and colloidal semiconductor nanocrystals at room temperature [6]. The most promising approach is using self-assembled quantum dots [31]. Although they typically work well under 10 K, they are attractive as single photon emitters for several reasons, including short luminescence lifetimes below one nanosecond, the feasibility of electrical excitation [32] and, more important, the possibility of integration into monolithic microcavities. An optical cavity can modify the properties of spontaneous emission through the Purcell effect. If a radiative transition of an emitter is in resonance with a cavity mode, the light will be emitted mainly into the cavity mode and the spontaneous emission rate will

be enhanced. Micropillars containing two distributed-Bragg-reflectors can serve as optical microcavities and the self-assembled quantum dots embedded in such mirocavites show an enhancement of the spontaneous emission rate with factors as large as 5 [33]. Higher Q-factor and smaller mode volume can be achieved using a microcavity formed by two-dimensional photonic crystals [34]. The indistinguishability between two independently created photons, one of the basic prerequisites in linear-optical quantum computation, was also demonstrated for the light spontaneously emitted by single quantum dots in a microcavity [35].

Despite the surprising variety of implementations, the idea of using spontaneous emission of isolated emitters is subject to some common restrictions. Many of the complex systems, including molecules, color centers, and quantum dots, have additional metastable states in the photoexcitation cycle [24, 7, 6, 31]. Trapped in those metastable states the systems are unable to emit photons, resulting in lower efficiency. Without the assistance of an optical cavity the propagation direction of spontaneously emitted photons is arbitrary, therefore the collection efficiency of the setups is very low, typically around one percent. Although triggered single photon emission can be realized by pulsed excitation, the low collection efficiency prevents the realization of an "on demand" source, since most of the excitations produce only vacuum states. The properties of the photons, such as polarization, spectrum and spatial-temporal mode, are determined by the emitters. A coherent transfer of quantum information between photons and atoms is also impossible, because spontaneous emission is inherently an irreversible process. Altogether, single photon sources based on spontaneous emission may suffice for applications in quantum cryptography, but for quantum computation and networking more sophisticated concepts must be developed.

If a quantum system with a three-state Λ-configuration is driven between the two ground states by a stimulated Raman process, single photons can be generated without spontaneous emission, since the excited state is never occupied during the process. This type of atom-photon interaction is intrinsically coherent and allows a complete control of the emitted single photons. To realize this idea A. Kuhn *et al.* let rubidium atoms fall through a high-finesse optical cavity [8]. When an atom is in the cavity, a laser beam illuminates the atom to excite one branch of the Raman transition, while the cavity vacuum stimulates the emission of a photon on the other branch. Further experiments were done with ions coupled to a cavity [36]. Since ions can be stored in a trap for a long time, they provide an almost ideal system for controlled generation of single photons.

Another coherent control technique of atom-photon interaction is the electromagnetically induced transparency (EIT) of dense atomic ensembles [37].

It can also be utilized to generate single photons [9]. In this approach a state of collective excitation in an ensemble of cold atoms is excited by a laser pulse (*write*), and the ensemble stays in the excited state till it is illuminated by a second laser pulse (*read*) and a photon is released. Recently it has been demonstrated, that controllable generation, transmission and storage of single photons with tunable frequency, timing and bandwidth can be realized using EIT [38].

So far, all the implementations of a single photon source are based on transitions between the energy states of quantum systems. There is still a completely different concept for a single photon source. In the spontaneous parametric down-conversion (SPDC) process a pump photon decays in a nonlinear crystal into a pair of photons with lower energy. As photons are created in pairs, the detection of one photon announces the presence of the complementary photon [10]. Single photons generated by such a way are therefore called "heralded".

Due to the perfect correlation between trigger and heralded photons in energy, timing and spacial mode, the properties of the heralded photons can be well tailored by defining the conditions for trigger photon detection. Therefore implementations with SPDC are favored for fiber-based applications. A Source operating at telecom wavelength was developed with a relatively simple setup and high efficiency [11]. Because in that source a continuous-wave pumping laser is employed, and single photons are heralded by detection of random trigger photons, it is not possible to synchronize the photon emission. To overcome this obstacle pulsed SPDC was also investigated [39]. In contrast to the cw case, the heralding efficiency in pulsed SPDC is complicated by the fact that the pumping pulses have a wider spectrum. Another issue is that the probability to create more than one pair of photons arises, while increasing the pumping power to enhance the efficiency of SPDC. There is always a tradeoff between the control of emission time and the purity of the single photons.

1.3   Subjects of this thesis

After this short overview of the diverse implementations of a single photon source, it is clear that a perfect source for all the possible applications is probably not realizable. Therefore it is reasonable to develop a source for certain tasks, improving the advantages and keeping the drawbacks acceptable for the particular applications.

The subjects of this thesis are color centers in diamond. The color centers are highly photostable at room temperature. It is not necessary to excite

them resonantly, therefore they are suitable for building a cheap and robust single photon source for applications, in which the purity of the single photons is not strongly demanded, e.g. quantum cryptography or educational demonstration of quantum optics. As already mentioned, NV centers suffer from their wide spectrum and long luminescence lifetime. There are more than 500 optical centers in diamond documented [40], which gives rise to hope for color centers with more suitable properties for single photon generation. The work in this thesis is focused on the SiV (silicon-vacancy) centers, including fabrication and characterization of single SiV centers. Another drawback of the color centers in diamond is the low collection efficiency of the fluorescence light due to the high refractive index of diamond, which can be bypassed using a solid immersion lens on bulk samples or creating color centers in diamond nanocrystals.

On the other hand, observation of an isolated system can reveal some phenomena which are hidden in measurements on ensembles. Investigations of single SiV centers show the transitions between different charge states and the dependence of the population of the charge state on the nano-environment. Those observations could give deeper insight into the electronic structure of the SiV centers and open new possibilities for manipulation of single color centers.

This thesis is organized as follows: Chapter 2 gives criterions for the characterization of a single photon source. The main utility in the investigation of single color centers, the second-order correlation function $g^{(2)}(\tau)$ of the fluorescence light, is introduced. In order to describe the color centers, the $g^{(2)}(\tau)$ of a non-resonantly driven two-level system is derived and the impact of an additional metastable level on the $g^{(2)}(\tau)$ and the efficiency of single photon generation is discussed. Chapter 3 introduces the general properties of diamond and the color centers in it. A brief description of the process of ion implantation is given as well, which is crucial for the fabrication of single SiV centers in bulk diamond. Chapter 4 describes experimental details in sample preparation, single color center detection and single photon state characterization. In Chapter 5 experimental results are presented for the optical investigation of single SiV centers. Improvements in the collection efficiency of the fluorescence light using a solid immersion lens or diamond nanocrystals are demonstrated. Chapter 6 is devoted to the other color center observed during the work. Finally Chapter 7 gives a summary of the work and discusses the perspectives of this project.

Chapter 2

Characterization of a single photon source

The merit of a single photon source is measured by the suppression of two-photon emission, purity of emitted photons and efficiency of single photon generation.

The second-order correlation function $g^{(2)}(\tau)$ can be employed to verify the single-photon emission of a source. While the classical theory predicts a lower bound of unity for $g^{(2)}(\tau)$, a single-photon state allows a minimum value of zero. Since $g^{(2)}(\tau)$ plays a central role in quantum optics, a detailed theoretic description is presented for both classical and quantum theory. The Hanbury-Brown-Twiss (HBT) interferometer is the standard way to measure $g^{(2)}(\tau)$, and is therefore discussed extensively in the framework of quantum theory.

The indistinguishability of single photons is crucial for most applications in quantum information processing with a remarkable exception of quantum cryptography. It can be proven by a Hong-Ou-Mandel type two-photon interference experiment [41, 35]. Since the purity of photons is not of the first priority for the systems studied in this thesis, only a brief introduction is devoted to this issue.

If single photons are generated by spontaneous emission, the efficiency of the source is ultimately determined by the luminescence lifetime of the single emitter, which is usually modeled as an ideal two-level system. In reality the energy level scheme of the single emitter is more complicated. A three-level system with a third level, which is metastable, describes the behavior of the investigated color centers much better than a mere two-level system. The existence of such a metastable level introduces additional fluctuations to the intensity of the emitted light. This phenomena is called emission intermittency. It decreases the efficiency of the source and can be detected

by measuring $g^{(2)}(\tau)$.

2.1   Second-order correlation function

The second-order correlation function originates from the study of optical coherence. Coherence is a concept aiming at quantifying the degree of correlations between light fields. It plays a central role in modern quantum optics. An intuitive approach to analyze the coherence properties of light is to study the interference patterns which arise from the spatial or temporal correlation between the electric field amplitudes. This is the so called first-order coherence. While dealing with phase is rather delicate, intensity correlation can be much more easily measured. The property of the intensity correlation of light fields is called the second-order coherence.

2.1.1   Classical theory

To quantify the second-order coherence, a second-order temporal correlation function is defined in classical theory as follows:

$$g^{(2)}(\tau) = \frac{\langle I(t) \cdot I(t+\tau) \rangle}{\langle I(t) \rangle^2} = \frac{\langle E^*(t)E^*(t+\tau)E(t+\tau)E(t) \rangle}{\langle E^*(t)E(t) \rangle^2}, \qquad (2.1)$$

where $I(t)$ is the time dependent intensity. $\langle \cdots \rangle$ denotes the average over a long time interval. $E(t)$ and $E^*(t)$ are the electronic field amplitude at time t and its complex conjugate, respectively. The order of field factors in the second-order correlation function follows a convention. Because in the classical theory electric field amplitudes are only complex numbers and allowed to commute, this convention has thus no consequences.

Although in eqn (2.1) the definiton of the second-order correlation function is rather general, some statements about its magnitude can still be made. The measured intensity are real numbers, thus they satisfies

$$\left\{ \frac{I(t_1) + I(t_2) + \cdots + I(t_N)}{N} \right\}^2 \leqslant \left\{ \frac{I(t_1)^2 + I(t_2)^2 + \cdots + I(t_N)^2}{N} \right\}. \quad (2.2)$$

For large N the left side approaches the square of the statistical average of intensity, and the right side the statistical average of the intensity square. Thus

$$\langle I \rangle^2 \leqslant \langle I^2 \rangle, \qquad (2.3)$$

and the second-order correlation function at $\tau = 0$ satisfies

$$g^{(2)}(0) = \frac{\langle I^2 \rangle}{\langle I \rangle^2} \geqslant 1. \qquad (2.4)$$

This argument does not apply to the case with nonzero τ, but a relation between $g^{(2)}(\tau)$ and $g^{(2)}(0)$ can be established by using the Cauchy-Schwarz inequality

$$\{\frac{I(t_1)I(t_1+\tau)+\cdots+I(t_N)I(t_N+\tau)}{N}\}^2$$
$$\leqslant \{\frac{I(t_1)^2+\cdots+I(t_N)^2}{N}\}\{\frac{I(t_1+\tau)^2+\cdots+I(t_N+\tau)^2}{N}\}. \quad (2.5)$$

The two sums on the right are equal for sufficiently many measurements. Thus the square root of the inequality in eqn (2.5) delivers

$$\langle I(t)I(t+\tau)\rangle \leqslant \langle I(t)^2\rangle, \quad (2.6)$$

and consequently

$$g^{(2)}(\tau) \leqslant g^{(2)}(0). \quad (2.7)$$

The value of the second-order correlation function can never exceed the one at $\tau = 0$ in classical theory.

2.1.2 Quantum theory

The formulation of the second-order correlation function in the framework of quantum theory requires quantization of the electromagnetic field. The standard procedure is well described in several textbooks [42, 43]. Here only the essential results of the field quantization concerning $g^{(2)}(\tau)$ are presented. In the field-free Heisenberg picture, the electromagnetic field with a given wavevector and polarization can be generally described as a superposition of the the number-states

$$|\phi\rangle = \sum_{n=0}^{\infty} c_n |n\rangle, \quad (2.8)$$

where c_n are time independent complex numbers which satisfy the normalization condition $\sum_{n=0}^{\infty} |c_n|^2 = 1$. The number states $|n\rangle$ are defined as the eigenstates of the energy operator $\hat{H}$, and the eigenvalue equation is

$$\hat{H}|n\rangle = \hbar\omega(\hat{a}^\dagger\hat{a}+\frac{1}{2})|n\rangle = (n+\frac{1}{2})\hbar\omega|n\rangle, \quad (2.9)$$

where ω is the angular frequency and n nonnegative integers. One photon has the energy of $\hbar\omega$, thus the number states $|n\rangle$ are considered to contain exactly n photons. The operators $\hat{a}^\dagger$ and $\hat{a}$ are called, respectively, the *destruction* and *creation* operators for photons because of the relations

$$\hat{a}^\dagger|n\rangle = \sqrt{n+1}|n+1\rangle \quad (2.10)$$

and

$$\hat{a}|n\rangle = \sqrt{n}|n-1\rangle. \tag{2.11}$$

From eqns (2.10) and (2.11) a fundamental commutator of the creation and destruction operators can be derived as

$$\left[\hat{a}, \hat{a}^\dagger\right] = \hat{a}\hat{a}^\dagger - \hat{a}^\dagger\hat{a} = 1. \tag{2.12}$$

The time dependent operator for the electric field is defined as

$$\hat{E}(t) = \hat{E}^+(t) + \hat{E}^-(t) = i(\hbar\omega/2\varepsilon_0 V)^{1/2}\{\hat{a}\mathrm{e}^{-i\omega} + \hat{a}^\dagger\mathrm{e}^{i\omega}\}, \tag{2.13}$$

where ε_0 is the electric permittivity, V the spacial volume of the optical system, and c the velocity of light in vacuum. The positive and negative frequency parts of the field operator, $E^+(t)$ and $E^-(t)$, are proportional to the destruction and creation operators respectively.

For the formulation of the second-order correlation function the intensity of the light field is of more interest. According to the photoelectric theory [43, pp. 173-175] the detection of a photon is equivalent to a transition between internal states of the detector. The transition amplitude is proportional to the matrix element of $\hat{E}^+(t)$. Thus the photon intensity operator is defined as

$$\hat{I}(t) = 2\varepsilon_0 c\hat{E}^-(t)\hat{E}^+(t), \tag{2.14}$$

where c is the velocity of light in vacuum. The correlated detection of one photon at time t and another at $t+\tau$ corresponds to the matrix element $\hat{E}^+(t+\tau)\hat{E}^+(t)$. Analogous to eqn (2.14), the intensity correlation is expressed as

$$\hat{I}(t) = (2\varepsilon_0 c)^2\hat{E}^-(t)\hat{E}^-(t+\tau)\hat{E}^+(t+\tau)\hat{E}^+(t). \tag{2.15}$$

These considerations lead to the the definition of $g^{(2)}(\tau)$ in quantum theory as

$$g^{(2)}(\tau) = \frac{\langle\hat{E}^-(t)\hat{E}^-(t+\tau)\hat{E}^+(t+\tau)\hat{E}^+(t)\rangle}{\langle\hat{E}^-(t)\hat{E}^+(t)\rangle\langle\hat{E}^-(t+\tau)\hat{E}^+(t+\tau)\rangle}. \tag{2.16}$$

With the definition of the field operator in eqn (2.13), the second-order correlation function is simplified for single-mode light to the form

$$g^{(2)}(\tau) = \frac{\langle\hat{a}^\dagger\hat{a}^\dagger\hat{a}\hat{a}\rangle}{\langle\hat{a}^\dagger\hat{a}\rangle^2}. \tag{2.17}$$

Unlike in classical theory the order of the creation and destruction operators has grave consequences. Using the commutator in eqn (2.12) $g^{(2)}(\tau)$ can be rewritten as

$$g^{(2)}(\tau) = \frac{\langle\hat{a}^\dagger(\hat{a}\hat{a}^\dagger - 1)\hat{a}\rangle}{\langle\hat{a}^\dagger\hat{a}\rangle^2} = \frac{\langle(\hat{a}^\dagger\hat{a})^2\rangle - \langle\hat{a}^\dagger\hat{a}\rangle}{\langle\hat{a}^\dagger\hat{a}\rangle^2}. \tag{2.18}$$

As an example we consider the value of $g^{(2)}(\tau)$ for the number state $|n\rangle$. With eqns (2.9) and (2.18) it is easy to show

$$g^{(2)}(\tau) = \frac{n^2 - n}{n^2} = 1 - \frac{1}{n} \qquad (2.19)$$

for any number states with nonzero n. If $n = 1$, $g^{(2)}(\tau)$ has the minimum value of 0. It is clearly contrary to the lower bound of 1 for $g^{(2)}(\tau)$ in classical theory shown in eqn (2.4). Since $g^{(2)}(\tau)$ is nonzero for any $n > 1$, it can be used as a benchmark for the purity of a single photon source.

The discussion of $g^{(2)}(\tau)$ above concerns only a single mode of light, therefore it is inherently restricted to the cases of time-independent fields. Since experiments of single photon generation usually deal with time-dependent light fields, theories involving two or more modes are required to describe them. With an integration over all possible modes the generalization from single-mode to continuous-mode theory is formally straightforward. The crucial consequence for $g^{(2)}(\tau)$ is that the creation and destruction operators are replaced by their time-dependent counterparts

$$\hat{a}^{\dagger}(t) = (2\pi)^{-1/2} \int_{-\infty}^{\infty} d\omega \hat{a}^{\dagger}(\omega) \mathrm{e}^{-i\omega t}. \qquad (2.20)$$

Since the frequency is defined to be positive, those Fourier-transformed operators are valid only for the case that the bandwidth of the field excitation is much smaller than the central frequency. For a stationary field the expression of time-dependent $g^{(2)}(\tau)$ thus is

$$g^{(2)}(\tau) = \frac{\langle \hat{a}^{\dagger}(t)\hat{a}^{\dagger}(t+\tau)\hat{a}(t+\tau)\hat{a}(t)\rangle}{\langle \hat{a}^{\dagger}(t)\hat{a}(t)\rangle^2}. \qquad (2.21)$$

2.1.3   Hanbury-Brown-Twiss interferometer

In the view of history, the discussion of the second-order correlation function was stimulated by a type of interferometer proposed R. Hanbury Brown and R. Q. Twiss in 1954 [44]. The original intention of Hanbury Brown and Twiss was to measure the angular diameter of radio stars [45]. Two years later they demonstrated that it can also be applied to visible light [46]. This type of interferometer, which measures the intensity correlation of a light field, is therefore called Hanbury-Brown-Twiss (HBT) interferometer. In 1977 J. H. Kimble *et al.* employed the HBT interferometer in their pioneering work to show photon antibunching, a striking nonclassical feature of light [3]. Since then, the HBT interferometer has become an important technique in quantum optics.
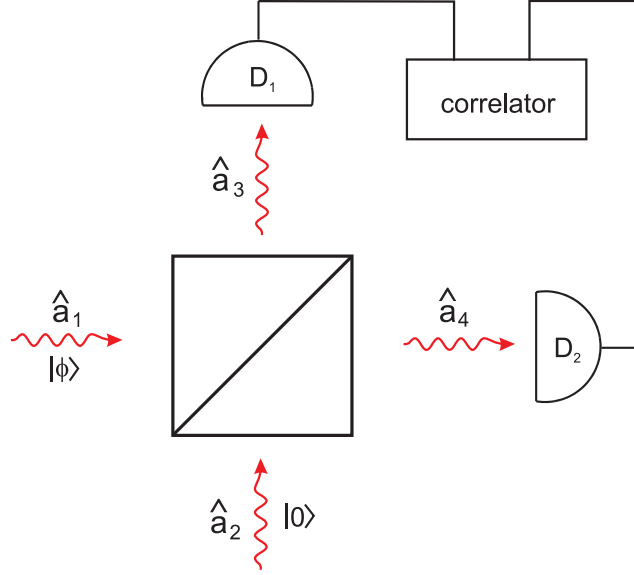
Figure 2.1: Arrangement of a Hanbury-Brown-Twiss interference experiment. The input and output arms of the beam-splitter are labeled by the destruction operators of the field.

In figure 2.1 the apparatus of a HBT interferometer is schematically depicted. Incoming light is divided by a 50:50 beam-splitter equally into two portions. The intensity of each portion is measured by the detectors D_1 and D_2. The outputs of these detectors are multiplied by one another in a correlator. The integrated value of the product over a long period provides the desired measurement of intensity fluctuation.

Since the beam splitter plays a central role in the setup, a quantum description of it is necessary to understand the HBT interferometer. The discussion in the preceding section shows that the detection of a photon is directly related to the destruction operator $\hat{a}$, therefore each arm of the beam splitter is labeled by a destruction operator. For a symmetric and lossless beam splitter the relations between inputs and outputs are expressed as

$$\hat{a}_3 = \mathcal{R}\hat{a}_1 + \mathcal{T}\hat{a}_2 \qquad \text{and} \qquad \hat{a}_4 = \mathcal{T}\hat{a}_1 + \mathcal{R}\hat{a}_2 \qquad (2.22)$$

with the reflection and transmission coefficients $\mathcal{R}$, $\mathcal{T}$. The coefficients $\mathcal{R}$ and $\mathcal{T}$ are complex numbers and vary generally with the frequency of the incident field. For simplicity, only monochromatic light is considered. Important properties of $\mathcal{R}$ and $\mathcal{T}$ are derived by considering the energy conservation between input and output arms. They satisfy the following conditions:

$$|\mathcal{R}|^2 + |\mathcal{T}|^2 = 1 \qquad \text{and} \qquad \mathcal{R}\mathcal{T}^* + \mathcal{R}^*\mathcal{T} = 0. \qquad (2.23)$$

With the use of eqns (2.22) and (2.23) it is easy to show that the boson commutation relations are also valid for the output:

$$[\hat{a}_3, \hat{a}_3^\dagger] = [\mathcal{R}\hat{a}_1 + \mathcal{T}\hat{a}_2, \mathcal{R}^*\hat{a}_1^\dagger + \mathcal{T}^*\hat{a}_2^\dagger] = |\mathcal{R}|^2 + |\mathcal{T}|^2 = 1 \qquad (2.24)$$

$$[\hat{a}_3, \hat{a}_4^\dagger] = [\mathcal{R}\hat{a}_1 + \mathcal{T}\hat{a}_2, \mathcal{T}^*\hat{a}_1^\dagger + \mathcal{R}^*\hat{a}_2^\dagger] = \mathcal{R}\mathcal{T}^* + \mathcal{T}\mathcal{R}^* = 0. \qquad (2.25)$$

In a HBT interferometer, the investigated light field $|\phi\rangle$ is in input arm 1, with input arm 2 remaining in its vacuum state, therefore the combined input is denoted by $|\phi\rangle_1|0\rangle_2$. It is straightforward to calculate the mean photon numbers for both outputs, and it follows from eqn (2.22) that

$$\begin{aligned} \langle n_3 \rangle &= {}_2\langle 0|_1\langle \phi ||\mathcal{R}|^2 \hat{a}_1^\dagger \hat{a}_1 + \mathcal{R}^*\mathcal{T}\hat{a}_1^*\hat{a}_2 + \mathcal{T}^*\mathcal{R}\hat{a}_2^*\hat{a}_1 + |\mathcal{T}|^2\hat{a}_2^*\hat{a}_2|\phi\rangle_1|0\rangle_2 \\ &= |\mathcal{R}|^2\langle n_1 \rangle \end{aligned} \qquad (2.26)$$

and

$$\langle n_4 \rangle = |\mathcal{T}|^2\langle n_1 \rangle, \qquad (2.27)$$

where

$$\langle n_1 \rangle = {}_1\langle \phi|\hat{a}_1^\dagger \hat{a}_1|\phi\rangle_1 \qquad (2.28)$$

is the mean photon number in the input 1. The mean value of the product of the photon number in the two outputs, as measured in the HBT interferometer, can be calculated analogously as

$$\begin{aligned} \langle n_3 n_4 \rangle &= \mathcal{R}^*\mathcal{R}\mathcal{T}^*\mathcal{T} \ {}_1\langle \phi|\hat{a}_1^\dagger \hat{a}_1 \hat{a}_1 \hat{a}_1^\dagger|\phi\rangle_1 + \mathcal{R}^*\mathcal{T}\mathcal{R}^*\mathcal{T} \ {}_1\langle \phi|\hat{a}_1^\dagger \hat{a}_1|\phi\rangle \\ &= |\mathcal{R}|^2|\mathcal{T}|^2 \ {}_1\langle \phi|\hat{a}_1^\dagger \hat{a}_1 \hat{a}_1^\dagger \hat{a}_1 - \hat{a}_1^\dagger \hat{a}_1|\phi\rangle_1 \\ &= |\mathcal{R}|^2|\mathcal{T}|^2 \ {}_1\langle \phi|\hat{a}_1^\dagger \hat{a}_1^\dagger \hat{a}_1 \hat{a}_1|\phi\rangle, \end{aligned} \qquad (2.29)$$

where eqns (2.12) and (2.23) are used.

A normalized second-order correlation function of the two output beams can be defined using the terms calculated above, in eqns (2.26), (2.27) and (2.29), as

$$g_{3,4}^{(2)}(\tau) = \frac{\langle n_3 n_4 \rangle}{\langle n_3 \rangle \langle n_4 \rangle} = \frac{\langle \hat{a}_1^\dagger \hat{a}_1^\dagger \hat{a}_1 \hat{a}_1 \rangle}{\langle \hat{a}_1^\dagger \hat{a}_1 \rangle^2} = g_1^{(2)}(\tau) \qquad (2.30)$$

where the subscripts denote the arms of the beam splitter. It is clear to see that a HBT interferometer measures exactly the second-order correlation function of the input light.

2.1.4 Two-level model for color centers

After the general discussion about the definition, properties and measurement of the second-order correlation function, we introduce a concrete physical
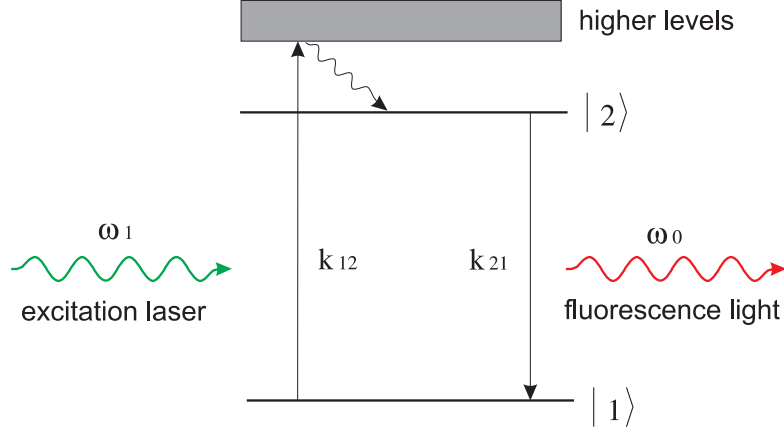
Figure 2.2: Energy-level model for color centers.

model for single color centers and derive $g^{(2)}(\tau)$ for the fluorescence light emitted by them.

A single color center at room temperature acts as an emitting dipole with strongly damped coherence, which can be modeled by a non-resonantly driven two-level system shown in figure 2.2 . The energy difference between the two lowest levels, state $|1\rangle$ and state $|2\rangle$, is $\hbar\omega_0$. This system is illuminated by a laser with a frequency ω_1, where $\omega_1 > \omega_0$. By absorbing one photon of the excitation laser, the system is excited from state $|1\rangle$ to the higher levels. From the higher levels the system relaxes very fast to state $|2\rangle$. Afterwards it decays to state $|1\rangle$ by spontaneous emssion of one photon with the frequency ω_0. The optical transition involves only the two lowest levels, therefore this system can be regarded as a non-resonantly driven two-level system.

With the assumption that the relaxation time from higher levels to the level 2 is negligible, the the pump rate coefficient k_{12} is proportional to the power of excitation laser. The fluorescent decay rate is described by the coefficient k_{21}. Neglecting the coherence, the population dynamics is governed by the rate equations

$$\dot{\rho}_1 = -k_{12}\rho_1 + k_{21}\rho_2 \qquad (2.31)$$
$$\dot{\rho}_2 = k_{12}\rho_1 - k_{21}\rho_2 \,. \qquad (2.32)$$

The populations ρ_1 and ρ_2 satisfy the condition $\rho_1 + \rho_2 = 1$. If the system is pumped by continuous wave laser, it reaches equilibrium, when $\dot{\rho}_1 = \dot{\rho}_2 = 0$. Solving the rate equations under the equilibrium condition leads to the pop-

ulation of the state $|2\rangle$ as

$$\rho_2(\infty) = \frac{k_{12}}{k_{12} + k_{21}}. \tag{2.33}$$

To verify the single photon characteristic, we derive the $g^{(2)}(\tau)$ for the fluorescence light. For this purpose it is convenient to define the transition operators for the atomic states as

$$\hat{\pi}^\dagger = |2\rangle\langle 1| \qquad \text{and} \qquad \hat{\pi} = |1\rangle\langle 2| \,. \tag{2.34}$$

The operator $\hat{\pi}^\dagger$ shifts the system from state $|1\rangle$ to state $|2\rangle$ and $\hat{\pi}$ produces the reverse transition. The time dependent destruction operator of the fluorescence light field is directly related to the atomic transition operator and can be expressed as [43, pp. 328-331]

$$\hat{a}(\vec{r}, t) \propto \hat{\pi}(0, t - r/c). \tag{2.35}$$

This relation can be understood by considering that the atomic transition from state $|2\rangle$ to state $|1\rangle$ must take place at time $t - r/c$, if at time t one photon is detected by a detector, which is located at the position with a distance r to the atomic system. The expectation value of the operator $\hat{\pi}^\dagger\hat{\pi}$ corresponds to the population of the state $|2\rangle$. Thus the $g^{(2)}(\tau)$ in eqn (2.21) can be rewritten in terms of atomic transition operators as

$$g^{(2)}(\tau) = \frac{\langle \hat{\pi}^\dagger(t)\hat{\pi}^\dagger(t + \tau)\hat{\pi}(t + \tau)\hat{\pi}(t)\rangle}{\langle \hat{\pi}^\dagger(t)\hat{\pi}(t)\rangle^2}, \tag{2.36}$$

where τ is assumed to be positive. The time interval, over which the experimental results are averaged, is considered to be long enough that the atomic system and the field have arrived at steady states and the fixed time difference r/c can be ignored.

In order to evaluate the second-order correlation function, the expectation value of a product of operators at different times has to be calculated. This can be obtained with the help of the *quantum regression theorem* [47]. Suppose the expectation value of any operator $\hat{A}$ at time $t + \tau$ is related to the expectation value of a set of operators $\hat{A}_i$ at an earlier time t according to

$$\langle \hat{A}(t + \tau)\rangle = \sum_i \alpha_i(\tau)\langle \hat{A}_i(t)\rangle, \tag{2.37}$$

the regression theorem proves that

$$\langle \hat{B}(t)\hat{A}(t + \tau)\hat{C}(t)\rangle = \sum_i \alpha_i(\tau)\langle \hat{B}(t)\hat{A}(t)\hat{C}(t)\rangle, \tag{2.38}$$

where $\hat{B}(t)$ and $\hat{C}(t)$ are arbitrary operators. From the definition of the atomic transition operators in eqn (2.34), it is obvious that the expectation value $\langle\hat{\pi}^{\dagger}(t)\hat{\pi}(t)\rangle$ is equal to the population of the state $|2\rangle$. The solution of $\rho_2(t+\tau)$ for a given $\rho_2(t)$ is obtained by solving the rate equations as

$$\rho_2(t+\tau) = \frac{k_{12}}{k_{12}+k_{21}}[1 - \mathrm{e}^{-\tau/\tau_0}] + \rho_2(t)\mathrm{e}^{-\tau/\tau_0} \tag{2.39}$$

with

$$\tau_0 = \frac{1}{k_{12}+k_{21}}. \tag{2.40}$$

Thus it follows from the eqn (2.39) with the use of the quantum regression theorem that

$$\begin{aligned}\langle\hat{\pi}^{\dagger}(t)\hat{\pi}^{\dagger}(t+\tau)\hat{\pi}(t+\tau)\hat{\pi}(t)\rangle &= \frac{k_{12}}{k_{12}+k_{21}}[1 - \mathrm{e}^{-\tau/\tau_0}]\langle\hat{\pi}^{\dagger}(t)\hat{\pi}(t)\rangle \\ &\quad + \mathrm{e}^{-\tau/\tau_0}\langle\hat{\pi}^{\dagger}(t)\hat{\pi}^{\dagger}(t)\hat{\pi}(t)\hat{\pi}(t)\rangle \\ &= \frac{k_{12}}{k_{12}+k_{21}}[1 - \mathrm{e}^{-\tau/\tau_0}]\langle\hat{\pi}^{\dagger}(t)\hat{\pi}(t)\rangle, \quad (2.41)\end{aligned}$$

where $\langle\hat{\pi}^{\dagger}(t)\hat{\pi}^{\dagger}(t)\hat{\pi}(t)\hat{\pi}(t)\rangle = 0$ is used. Now the only term unknown in the eqn (2.36) is $\langle\hat{\pi}^{\dagger}(t)\hat{\pi}(t)\rangle$. This average value can be interpreted as the population of the state $|2\rangle$ in equilibrium, since the whole system is in steady states. Thus

$$\langle\hat{\pi}^{\dagger}(t)\hat{\pi}(t)\rangle = \rho_2(\infty) = \frac{k_{12}}{k_{21}+k_{12}}. \tag{2.42}$$

Inserting eqns (2.41) and (2.42) into eqn (2.36) leads to the second-order correlation function for the fluorescence light of a single color center modeled by a driven two-level system:

$$g^{(2)}(\tau) = 1 - \mathrm{e}^{-\tau/\tau_0}. \tag{2.43}$$

The zero value of $g^{(2)}$ at $\tau = 0$ reflects the inability of a single color center to emit more than one photon simultaneously. The emitted photons are separated by a time constant τ_0, therefore such a driven two-level system is able to generate single photon states.

2.2   Two-photon interference

If photons enter a 50:50 beam-splitter from both input arms, they tend to leave the beamsplitter both in one output arm as a result of the Bose-Einstein

statistics of photons. The strength of this effect depends on the overlap of the photon wave packets. It was first predicted and observed by Hong, Ou and Mandel in 1987 for photon pairs produced by spontaneous parametric down-conversion [48].

The state with one photon in each input arm can be expressed using the time-dependent creation operator defined in eqn (2.20) as

$$|1\rangle_1|1\rangle_2 = \int dt \int dt' \xi_1(t)\xi_2(t')\hat{a}_1^\dagger(t)\hat{a}_2^\dagger(t')|0\rangle, \qquad (2.44)$$

where the numerical subscripts indicate the beam splitter arms as shown in figure 2.1, and the wave packet amplitudes $\xi_i(t)$ satisfy the normalization conditions

$$\int dt \xi_i(t) = 1. \qquad (2.45)$$

Substitution of the input operators by output operators using the input-output relation of a beam splitter defined in eqn (2.22) gives

$$|1\rangle_1|1\rangle_2 = \int dt \int dt' \{\mathcal{RT}\xi_1(t)\xi_2(t')\left[\hat{a}_3^\dagger(t)\hat{a}_3^\dagger(t') + \hat{a}_4^\dagger(t)\hat{a}_4^\dagger(t')\right]$$
$$+ \left[\mathcal{R}^2\xi_1(t)\xi_2(t') + \mathcal{T}^2\xi_1(t')\xi_2(t)\right]\hat{a}_3^\dagger(t)\hat{a}_4^\dagger(t')\}|0\rangle, \quad (2.46)$$

where suitable exchange of the time variables is used for the arrangement on the right-hand side of the equation.

The last term of the integrand describes the output state where one photon exists in each output arm. The probability to observe such a state is given by the coefficient of this term as

$$P(1_3, 1_4) = \int dt \int dt' \left|\mathcal{R}^2\xi_1(t)\xi_2(t') + \mathcal{T}^2\xi_1(t')\xi_2(t)\right|^2. \qquad (2.47)$$

Further use of the normalization in eqn (2.45) and the standard beam splitter properties in eqn (2.23) leads to

$$P(1_3, 1_4) = 1 - 2|\mathcal{R}|^2|\mathcal{T}|^2(1 + J) \qquad (2.48)$$

with

$$J = \left|\int dt \xi_1^*(t)\xi_2(t)\right|^2. \qquad (2.49)$$

If the overlap of the photon wave packets is perfect, i.e. $J = 1$, $P(1_3, 1_4)$ disappears for a 50:50 beam splitter with $|\mathcal{R}|^2 = |\mathcal{T}|^2 = 0.5$. In experiments the reduction in coincidence rate of the detectors D_1 and D_2 gives a measure of the indistinguishability of the single photons.

2.3   Efficiency of a single emitting dipole

The discussion about the efficiency of a single photon source depends strongly on the operating principles of the source. In this section, only the intrinsic efficiency of a single emitting dipole is discussed, regardless of specific experimental setups.

In experiments which aim at building a simple single photon source the exact electronic configuration of the emitting dipoles is often not of interest. Simplified energy-level models are commonly employed to describe these systems. First we consider the two-level model shown in figure 2.2. The relation between the pump rate coefficient k_{12} and the excitation power P_e is assumed as

$$k_{12} = aP_e \, ,\tag{2.50}$$

where a is a constant. The photon emission rate R is equal to $k_{21}\rho_2$. Using eqns (2.33) and (2.50) R can be expressed for the case of equilibrium in dependence of the excitation power as

$$R(P_e) = \frac{k_{21}P_e}{P_e + k_{21}/a} = \frac{k_{21}P_e}{P_e + P_{sat}} \, ,\tag{2.51}$$

with a constant $P_{sat} = k_{21}/a$, which is called saturation power. If $P_e \ll P_{sat}$, R increases linearly with the excitation power. In case $P_e \gg P_{sat}$, R approaches a constant equal to k_{21}. This behavior is called saturation. The coefficient k_{21} is the only physical limitation of the photon emission rate, therefore color centers with a short luminescence lifetime which is equal to $1/k_{21}$ are advantageous for a single photon source.

As far as the efficiency of an emitting dipole is concerned, it is reasonable to define a quantity which is independent of the excitation power. We consider $E_s = R(P_e = \infty)$ as a measure of the source efficiency, since it represents the ultimate limitation of the single photon generation rate of a source. For the two-level model, it applies

$$E_s = k_{21} \, .\tag{2.52}$$

In reality the electronic configuration of color centers are more complicated. There are often additional levels involved in the pump-and-decay circle. If the system is trapped in such a metastable state, commonly denoted as "shelving level", it is unable to emit photons until it relaxes back to the excited or the ground level. Obviously the existence of a shelving level decreases the efficiency of the source.

Such a metastable state is denoted as $|3\rangle$ in figure 2.3(a). Again only level populations ρ_i are considered due to the fast damping of coherence. The

system is allowed to decay from the state $|2\rangle$ to $|3\rangle$ with the rate of k_{23}, and from $|3\rangle$ to $|1\rangle$ with k_{31}. The transitions involving the state $|3\rangle$ are assumed to be non-radiative. It is also possible that the system has a transition from $|3\rangle$ to $|2\rangle$. This "deshelving" has been observed experimentally [49], and may be important under strong pumping conditions. But this transition has similar effects on the system as the transition from $|3\rangle$ to $|1\rangle$. Additionally, a thermal transition from $|3\rangle$ to $|2\rangle$ is probably negligible for SiV centers, since luminescence lifetime measurements show monoexponential decay of the fluorescence intensity over at least one and a half decades [50]. Therefore this transition is not considered here for simplicity.

The rate equations in eqn (2.31) and (2.32) can be extended to the three-level system straightforwardly as

$$\dot{\rho}_1 = -k_{12}\rho_1 + k_{21}\rho_2 + k_{31}\rho_3 \qquad (2.53)$$
$$\dot{\rho}_2 = k_{12}\rho_1 - (k_{21} + k_{23})\rho_2 \qquad (2.54)$$
$$\dot{\rho}_3 = k_{23}\rho_2 - k_{31}\rho_3 . \qquad (2.55)$$

Those equations can be solved analytically. The equilibrium population of state $|2\rangle$ is calculated as

$$\rho_2(\infty) = \frac{k_{12}}{(1 + \frac{k_{23}}{k_{31}})k_{12} + k_{21} + k_{23}} . \qquad (2.56)$$

The photon emission rate can be expressed in dependence of the excitation power analogously as for the two-level model in eqn (2.51) as

$$R(P_e) = \frac{\xi k_{21} P_e}{P_e + P_{sat}}, \qquad (2.57)$$

where

$$\xi = \frac{1}{1 + \frac{k_{23}}{k_{31}}}, \qquad (2.58)$$

and

$$P_{sat} = \xi(k_{21} + k_{23})/a. \qquad (2.59)$$

It is obviously that

$$E_s = \xi k_{21}. \qquad (2.60)$$

If $k_{23} = 0$, ξ is equal to unity, and consequently the three-level model is reduced to the two-level model discussed above. Usually k_{23} is small compared to k_{21}. However, ξ can decrease E_s drastically even for a small k_{23}, if $k_{23} \gg k_{31}$.
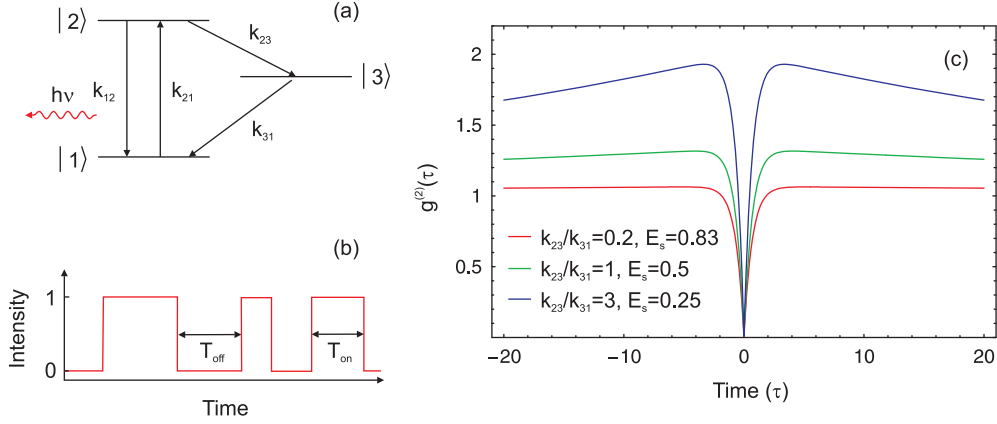
Figure 2.3: (a) Three-level model for color centers. The fluorescence is collected from the transitions between the states $|2\rangle$ and $|1\rangle$, and the state $|3\rangle$ is a metastable state. (b) Schematic presentation of the intensity fluctuation of the fluorescence light of the three-level system. (c) $g^{(2)}(\tau)$ calculated for $k_{12} = 0.5$, $k_{21} = 1$, $k_{31} = 0.01$ and $k_{23}/k_{31} = 0.2$ (red), 1 (green), and 3 (blue).

On the other hand, the existence of such a shelving level introduces additionally fluctuations to the fluorescence intensity, therefore it is also reflected in the second-order correlation function of the fluorescence light. $g^{(2)}(\tau)$ contains valuable information about the transition rate coefficients between the energy levels. In an analogous manner, an expression of $g^{(2)}(\tau)$ is obtained by normalizing $\rho_2(t)$ to $\rho_2(\infty)$ resulting in

$$g^{(2)}(\tau) = 1 + c\,e^{-\tau/\tau_1} - (1+c)\,e^{-\tau/\tau_2}, \qquad (2.61)$$

where τ_1, τ_2 and c are given by

$$\tau_{1,2} = 2/(A \pm \sqrt{A^2 - 4B}) \qquad (2.62)$$

$$c = \frac{1 - \tau_1 k_{31}}{k_{31}(\tau_1 - \tau_2)}, \qquad (2.63)$$

with

$$A = k_{12} + k_{21} + k_{23} + k_{31} \qquad (2.64)$$

$$B = k_{12}k_{23} + k_{12}k_{31} + k_{21}k_{31} + k_{23}k_{31}. \qquad (2.65)$$

This lengthy expression is not very illuminating. To achieve a descriptive understanding of the impact of the shelving level on $g^{(2)}(\tau)$, we assume an

ideal photon detector which measures the photon flux without interruption. This detector registers the intensity of the fluorescence light in dependence of time. If k_{23} and k_{31} are small compared to k_{12} and k_{21}, the results can be schematically illustrated as in figure 2.3(b). In the on-periods, the source acts as a two-level system, therefore the possibility to detect two photons separated by a time difference $\tau \ll \overline{T}_{on}$ is determined only by k_{12} and k_{21}, where $\overline{T}_{on}$ is the average length of the on-periods and equal to $1/k_{23}$. Therefore $\langle \hat{a}^\dagger(t)\hat{a}^\dagger(t+\tau)\hat{a}(t+\tau)\hat{a}(t) \rangle$ is independent of k_{23} and k_{31} for a short τ. If the system is trapped in the shelving level, the source is turned off. No photons are detected during the off-periods which has an average length of $\overline{T}_{off} = 1/k_{31}$. Considering the average intensity of the fluorescence light it applies

$$\langle \hat{a}^\dagger(t)\hat{a}(t) \rangle \propto \overline{T}_{on}/(\overline{T}_{on} + \overline{T}_{off}) = \frac{1}{1 + k_{23}/k_{31}}. \qquad (2.66)$$

Thus $\langle \hat{a}^\dagger(t)\hat{a}(t) \rangle$ decreases, if the ratio k_{23}/k_{31} increases. According to the definition of the second-order correlation function in eqn (2.21), $g^{(2)}(\tau)$ then has higher values for larger k_{23}/k_{31}.

If the value of $g^{(2)}$ exceeds 1, we speak of correlated emission. In order to illustrate the relationship between the efffect of correlated emission and the source efficiency, three theoretic curves of $g^{(2)}(\tau)$ are plotted in figure 2.3(c) with constant k_{12}, k_{21} and k_{31} but variable k_{23}. The calculated values E_s are also presented in this figure. It is clear to see that at a constant excitation the effect of correlated emission becomes stronger with increasing k_{23}/k_{31}, while the source efficiency decreases. Hence, information about the source efficiency of a color center may as well be derived from $g^{(2)}(\tau)$.

Chapter 3

Diamond and its defects

As an extreme form of atomic aggregation in nature, diamond possesses numerous extreme properties. Although diamond is primarily a desirable gem stone to the public, those extreme properties make it a fascinating object both for science and industry. Since natural diamond is one of the rarest and most expensive minerals, no industrial use of diamond had been possible, before synthesis methods were found. Thus we give a brief introduction about the production of synthetic diamonds. Nowadays synthetic diamonds are finding applications in various areas, such as material science, medicine, electronics and optics.

Properties of diamond are not only determined by its lattice structure. Defects in diamond also play a vital role. For example, natural diamond is classified according to the type and content of the defects in it. During the last decades, a series of experimental methods have been developed for investigation of defects in diamond, and some of them are presented in this chapter. Some of the defects are luminescent, and thus are able to determine the color of diamond. Those defects are called color centers. Since the single photon source investigated in this thesis is based on color centers, we discuss the properties of them in detail.

Ion implantation is an important technique to modify the properties of diamond by creating artificial defects. In this thesis it is employed to fabricate single color centers. The mechanism of ion implantation and the subsequent annealing is vital for the sample preparation and is outlined in this chapter.

3.1 Diamond in science and industry

3.1.1 Properties of diamond

The diamond crystal is formed by sp^3-bonded carbon atoms arranged in the so called "diamond lattice", which consists of two face-centered cubic lattices shifted by a vector $(a/4, a/4, a/4)$. The lattice parameter a is 3.56683 Å. Diamond has the greatest number density, i. e. atoms per unit volume, of any known substance. This, combined with the strength of the carbon-carbon bond, gives rise to an extraordinarily high bond energy density, therefore diamond exhibits extreme mechanical properties, e.g. hardness and bulk modulus. Diamond is the hardest known natural material, scoring 10 on the old Mohs scale of mineral hardness. The hardness and wear resistance increase with impurity content, and the physical mechanism responsible for that is believed to be the hindering of dislocation movement by impurities. The high bond energy density also leads to the chemical resistance to most acids and alkalis.

At room temperature, diamond has a thermal conductivity roughly four times superior to that of copper, although it is an excellent insulator. The reason for this unusual combination of properties is that heat is transported in diamond by phonons instead of electrons. The rigidity of the diamond lattice results in unusually small phonon interactions and consequently large mean path length of phonons. The presence of defects causes additional phonon scattering, therefore the thermal conductivity of diamond depends on the crystal quality. Due to the high lattice vibration frequency, most phonons in diamond freeze out already at liquid nitrogen temperature. It is a convenient feature for optical measurements.

Diamond can also be treated as a semiconductor with a wide band gap of 5.5 eV. Due to the wide band gap, diamond is transparent for the spectral range from the deep UV to far IR. The brilliance of a diamond crystal is owing to its high refractive index. With a value of about 2.4 it is the highest of any transparent substances for visible light. The wide band gap grants diamond a very low or negative electron affinity, i. e. it is able to emit electrons from its surface with very little applied voltage.

3.1.2 Methods of diamond synthesis

Already at the turn of 19th century, it was established that diamond was an allotrope of carbon. Since then, many attempts have been made to synthesize diamond. Thermodynamic calculations suggest that the stable phase of carbon form is graphite rather than diamond at ambient pressure and tem-
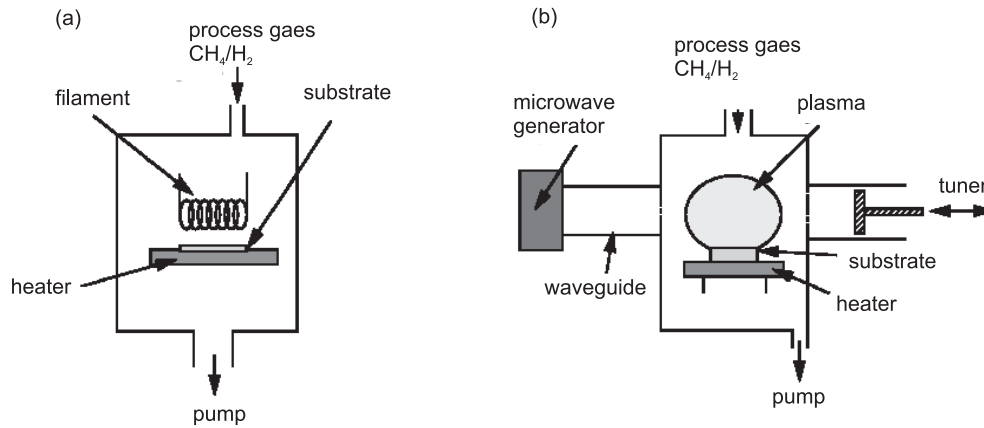
Figure 3.1: Examples of two of most common types of low pressure CVD reactor. (a) Hot filament reactor, after [53]. (b) Microwave plasma enhanced reactor, after [54].

perature, therefore it is possible to convert graphite into diamond under high pressure and high temperature (HPHT), where diamond is the stable form. This idea leads to the method of HPHT synthesis.

In the HPHT synthesis method [51, chap. 10], hydrostatic pressure of some hundreds of kbar and a temperature of the order of 2000 °C are applied to graphite for times from minutes to hundreds of hours. The detailed arrangement of a HTHP setup differs between manufacturers and is subjected to commercial secrecy. Merely subjecting graphite to high pressures and temperatures does not necessarily result in transformation to diamond, since a large activation energy is required to break carbon-carbon bonds. Molten transition metals of group VIII of the periodic table are widely used commercially as solvent and catalysts for the growth of synthetic diamond, e.g. iron, nickel, and cobalt or alloys of those elements. The morphology of the grown crystals is determined by the pressure and temperature. The rate of growth of diamond depends on the solubility difference of carbon at the graphite-metal and metal-diamond interfaces at a fixed temperature. Diamond of approximately 1 mm size can be grown. Large diamonds are best grown using the reconstitution technique, where diamond is used as the source of carbon [52].

Diamond can also be grown at metastable conditions by chemical vapor deposition (CVD) method as well. During the CVD process, a gas-phase chemical reaction occurs above a solid surface, which causes deposition onto that surface. For the activation of the carbon-containing precursor molecules

a high temperature of the gas, typically above 2000 °C, is required. To achieve this, several techniques can be employed, including thermal (e.g. hot filament) or plama (DC or microwave) activation, or use of combustion flame (oxyacetylene or plasma torches). Two of the most popular experimental setups are illustrated in figure 3.1. High gas temperatures combined with substrate temperature below the graphitization limit of diamond (< 1500 °C) lead to high growth rate [55]. Not only the gas temperature, but also the gas composition is crucial for the growth rate and crystal quality. Typically a mixture of CH_4 and H_2 is used. The fact that diamond instead of graphite, the stable carbon form, is grown by CVD method is inextricably linked to the presence of hydrogen atoms generated via dissociation of H_2 and hydrocarbon molecules. The hydrogen atoms are believed to play a number of crucial roles in the CVD process [56]. They undergo hydrogen abstraction reactions with stable gas-phase hydrocarbon molecules, so that highly reactive carbon radical species are produced, which are necessary for forming C-C bonds. Hydrogen atoms can also terminate the dangling carbon bonds on the growing diamond surface and prevent them from reconstructing to graphite-like surface. Most important, atomic hydrogen etches both diamond and graphite but, under typical CVD conditions, the rate of diamond growth exceeds its etch rate whilst for other forms of carbon the inverse is true.

Depending on the type of substrate there are two principal synthesis varieties: growth of diamond on diamond (homoepitaxy) and on non-diamond substrates (heteroepitaxy). Homoepitaxy results in monocrystalline layers with superior properties. However, the growth rate is slow due to the low surface chemical activity of diamond. Additionally the diamond substrate is expensive and limited in size. Heteroepitaxy films may consist of oriented or non-oriented grains. They contain numerous defects, like grain boundaries and amorphous carbon, but they can be grown to large sizes.

Intentional doping during the CVD process is usually achieved by addition of dopant gases. It is widely used to modify the electric properties of diamond to *p*-type or *n*-type semiconductor [57]. But it is hardly possible to create desired color centers in CVD diamond film in such a low density that single ones can be addressed by optical microscopes, just as required for optical investigation of single color centers. The situation is changed, if the CVD process is aborted just after the nucleation of diamond grains of tens of nanometers size. Due to the small size it is probable to find diamond nanocrystals containing only one single color center [27].

3.1.3 Applications of diamond

The research efforts in diamond synthesis are rewarded by its unique properties which are useful for many applications.

Due to the extreme hardness, diamond is used in material science as a hardness indenter or as pressure amplifiers to produce extraordinarily high pressures [51, pp. 622-624]. In industry, diamond is widely employed for machining of non-ferrous material. This is most commonly done by distributing micrometer-size diamond in a metal matrix, usually cobalt, to harden it [51, p. 648]. In recent years, CVD diamond coated tools are also commercially available. The phrase "non-ferrous" is worth emphasizing, since it points out a major limitation of diamond that it reacts with iron at high temperature and dissolves. Additionally, diamond surfaces have low friction against living cell, and the strong atomic bond leads to sharper edges than for other materials. Therefore surgical blades made of diamond have much higher performance than that of steel [51, p. 629].

The high thermal conductivity and electric resistivity make diamond an ideal heat sink for electric circuits. Active devices mounted on diamond chips can operate at higher power or be packed more tightly without overheating. For microwave diodes and semiconductor laser diodes, diamond heat sinks are widely used [51, pp. 608-613].

As a semiconductor, diamond has various advantages for electronics. Due to the band gap, it is inherently suitable to emit or detect UV light. The low electron affinity allows electron emission at low temperatures. Devices based on diamond readily work at harsh conditions, e.g. under radiation or chemical corrosion. UV-sensors [58], light emitting diodes [59], cold cathode [60], metal-semiconductor FETs [61] and electro-chemical electrodes [62] have all meanwhile been implemented using diamond. There are however a number of problems to be overcome. The major obstacle is the growth of high quality crystals of considerable size at reasonable cost. Another outstanding challenge is the difficulty in realizing of n-type doping. While a good p-type conductivity can be straightforwardly achieved by boron doping, an effective method to produce n-type diamond is still lacking despite numerous attempts with dopants such as phosphorous, sulfur and lithium. The rigidity of the lattice and small atomic radius of carbon render doping with larger atoms a challenging task [56].

For optical applications, components made of diamond benefit from the remarkable wide transmission range and high refractive index. Combined with high thermal conductivity, hardness, wear resistance and chemical inertness, it is the material of choice for high power laser, spacecraft and fiber optic backbones. Windows, lenses, prisms and beam-splitters made of dia-

mond are now commercially available.

3.2   Defects in diamond

Pure diamond crystal is colorless and an excellent insulator. However, many
diamond crystals exhibit some electrical conductivity, particularly at high
temperatures, and most diamond crystals show absorption in the visible re-
gion. The reason is that diamond contains defects. There is a huge variety of
defects in diamond. They can be divided into two groups: intrinsic defects
and impurity-related defects. Intrinsic defects include vacancies, interstitials
and extended structural defects such as dislocations. Small foreign elements,
such as boron and nitrogen, can appear as single atoms at lattice sites, while
large impurity atoms tend to form complexes with other impurities or va-
cancies. In general it is believed that incorporation of impurity is difficult
for diamond. Nevertheless, more than 300 optical and ESR (electron spin
resonance) centers due to the elements H, He, Li, B, N, O, Ne, S, Si, P, Ti,
Cr, Co, Ni, Zn, As, Zr, Ag, Xe, Ta, W, Tl in diamond are documented [40].

3.2.1   Classification of diamond

Depending on the production method, nowadays one commonly distinguishes
natural, HPHT and CVD diamond. Natural diamond can be traditionally
subdivided into four types, i.e. Ia, Ib, IIa and IIb, according to the dominant
type of defects present.

   More than 95% of all natural diamonds belong to the type Ia. Diamonds
of this type have the highest concentration of nitrogen (up to 3000 ppm).
The nitrogen is present in aggregations, two major forms of which are the
A- and B-center. The A-center consists of a pair of substitutional nitrogen
atoms in nearest neighborhood, while the B-center occurs as a complex of
four substitutional nitrogen atoms surrounding a lattice vacancy. The name
of the nitrogen aggregations originates from IR absorption measurements, in
which the corresponding absorption bands are named group A and B.

   In the rare natural type Ib diamonds, the concentration of nitrogen is
still considerable, ranging between 150 and 600 ppm. However, the nitrogen
is dominantly in single-substitutional form. Single substitutional nitrogen
atoms are donor centers in diamond with a thermal and optical ionization
energy of 1.7 and 2.2 eV, respectively [63, p. 36]. The optical absorption of
them gives rise to the slightly yellow color of Ib diamonds.

   A type II diamond is defined as one in which the concentration of nitro-
gen impurity is below the IR absorption sensitivity ($\sim$ 1 ppm). While IIa

refers to the purest crystals, in IIb diamonds boron is the dominant impurity. The only known boron-related defect is a single substitutional acceptor with an energy level 0.37 eV above the valence band. Therefore IIb diamond exhibits p-type conductivity at room-temperature. Optical absorption produced by ionization of the acceptors begins from infrared and continues to visible region, which gives IIb diamond the characteristic blue color.

This classification is also used for HPHT diamond. Nitrogen is the most common contamination during the HPHT Synthesis. At the HPHT conditions of diamond growth, the nitrogen impurity is incorporated into diamond as single atoms, and consequently, most as-grown HPHT diamonds are of the type Ib. Type IIb diamond can be produced, if boron is intentionally added into the growth chamber and the nitrogen content is reduced. High-temperature annealing leads to aggregation of single substitutional nitrogen to A (at $T > 1500°C$) then to B (at $T > 2000°C$) complexes [64], and consequently the conversion of Ib into Ia diamond. CVD diamonds contain much more elements as impurity, depending on the the substrates and gas mixture used. Thus the classification usually does not apply to them.

3.2.2 Experimental analysis of defects

The investigation of defects is a major subject in diamond research. Defects in diamond can be identified and characterized by electrical, optical and nuclear techniques. Usually, a combination of several techniques is necessary to give a conclusive description of a defect. Some of them, which are of importance for this thesis, are introduced here.

Raman spectroscopy. The vibration energy of atoms in a crystal lattice is quantized as quasi particles, the phonons, with the energy of $\hbar v_{phonon}$. The frequencies of the phonons are very sensitive to the nature of atomic bonds, type of atoms and their mutual distance, therefore measurements of the phonon frequencies reveal different phases and internal stress in a material. The Raman effect is based on inelastic light scattering arising from interaction between photons and phonons. A monochromatic incident light field with the frequency v_{in} can be either create or destroy phonons, which gives rise to the Stokes Raman line with frequency $v_{out} = v_{in} - v_{phonon}$ and anti-Stokes Raman line with frequency $v_{out} = v_{in} + v_{phonon}$. The anti-Stokes line is much weaker than the Stokes line and vanishes at low temperatures, since phonons can only be destroyed if they already exist in the crystal. Therefore the Stokes line is commonly used for Raman spectroscopy.

The diamond Raman spectrum consists of a sharp first-order peak at 1332 cm^{-1}, while graphite gives rise to a broader peak at 1580 cm^{-1}. The ratio of intensities of the two peaks indicates how much of each phase is present.
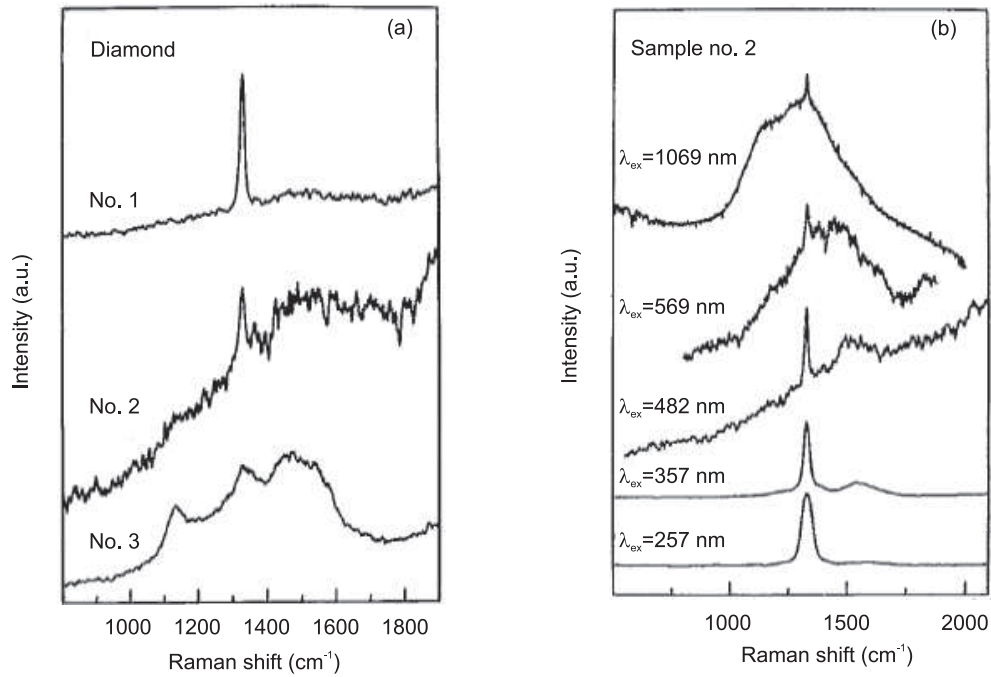
Figure 3.2: (a) Raman spectra of different CVD diamond films excited at 532 nm; Sample no.1 is of the highest quality and no.3 the lowest. Redrawn after [65]. (b) Raman spectra measured for the sample no.2 in (a) with different excitation wavelength. Redrawn after [65]. The curves have been displaced vertically for clarity.

The width of the 1332 cm^{-1} line reveals how much random stress exists in the sample. Figure 3.2(a) shows the Raman spectra of three different CVD diamond films. The quality of them is clearly distinguishable. The form of Raman spectra is greatly influenced by the excitation wavelength [65]. As shown in figure 3.2(b), the Raman spectrum measured with UV excitation suggests a fairly good quality. However, if IR light is used, some non-diamond components emerge in the spectrum. IR light is more sensitive to scattering from the sp^2-bonded carbon.

The Raman scattering is often measured together with photoluminescence (PL). Normalization of PL intensity to the integrated diamond Raman peak provides certain quantitative comparison of PL from different measurements, since the intensity of Raman line contains information about the system response and intensity of incident light.

Electron spin resonance. Unpaired electrons in solids have a non-vanishing spin which is associated with a magnetic moment. Consequently in a magnetic field the spin states have different energies. Transitions may be

caused between those states by resonant absorption of electromagnetic radiation. The phenomenon is known as ESR. At defect sites, unpaired electrons are localized in a region of a discrete crystal lattice. The paramagnetism of these electrons reflects the interaction of electrons with their environment, and gives rise to a characteristic ESR signal. For defects in diamond the most common spin Hamiltonian can be written in the form [66]:

$$\mathcal{H} = \mu_B \hat{\boldsymbol{H}} \cdot g \cdot \hat{\boldsymbol{S}} + \hat{\boldsymbol{S}} \cdot D \cdot \hat{\boldsymbol{S}} + \hat{\boldsymbol{S}} \cdot A \cdot \hat{\boldsymbol{I}}. \qquad (3.1)$$

The first term represents the electronic Zeeman interaction with the magnetic field $\hat{\boldsymbol{H}}$, the second the interaction of the electron spin with the crystal field produced by the surrounding of the paramagnetic center, and the last is the magnetic hyperfine interaction. $\hat{\boldsymbol{S}}$ and $\hat{\boldsymbol{I}}$ are operators of electronic and nuclear spin, respectively, and g, D and A are tensors which can be determined experimentally.

Besides the identity of the defects the ESR spectra contain a lot of information about them. The magnitude of a certain line indicates the concentration of the corresponding defect and the number of lines immediately show the spin state. Information about nuclear spins associated with the defects can be derived from the hyperfine components in the lines. The anisotropy of the spectra as the crystal is rotated in an external magnetic field reveals the symmetry properties of the defect. Finally, the width of the lines gives information about magnetic and exchange interactions between defects and about spin-lattice relaxation effects.

Natural and synthetic diamond has been extensively studied by ESR. Now, this method is gaining new attention due to the possibility to use the spin states in the NV (nitrogen-vacancy) center to implement a solid state qubit at room-temperature [67].

Optical absorption and luminescence. Infrared light absorption occurs in diamond due to lattice vibration. For symmetry reasons, one-phonon absorption is forbidden in homopolar lattices such as diamond [69]. Therefore the IR spectrum of high purity diamond is dominated by the two-phonon absorption bands around 2000 and 2500 cm^{-1}, as shown in figure 3.3. However, the existence of defects breaks the symmetry and thus enables one-phonon absorption. For example, the absorption band A in figure 3.3 is induced by the A-centers.

The detailed shape of the absorption band depends on the specific nature of the defect. The strength of the characteristic IR absorption is associated with the concentration of a certain defect. For example, the concentration of single substitutional nitrogen atoms has been measured in synthetic Ib diamond by two independent methods, namely ESR and infrared absorption. The results agree within better than 7% [70].
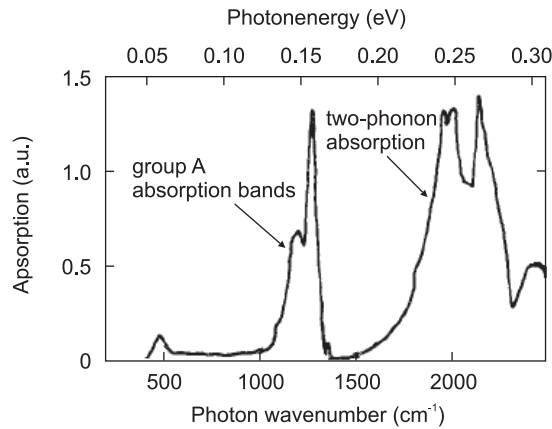
Figure 3.3: Infrared absorption of a type Ia diamond. Below 0.2 eV are the impurity-induced group A absorption bands; above 0.2 eV the lattice bands due to two-phonon absorption. After [68].

Absorption and luminescence in the visible region are of electronic nature. Absorption can take place due to transitions between a defect level and the valence or conduction band, and radiation due to transitions between two defect levels or two bands of defect levels inside the diamond band gap. Results of those experiments are often combined with thermal or photoconductivity measurements to determine the position of the defect levels within the band gap. Another mechanism of absorption and emission can also be observed from transitions between excited and ground states of a defect center. This is more of interest for the investigation of a certain defect.

Luminescence can be excited by either an electron beam or light. The methods are called cathodoluminescence (CL) and photoluminescence (PL), respectively. While using CL the investigation is restricted to the surface region owing to the limited penetration depth of electron beam, PL can take place all over in the whole sample, since diamond has a wide transmission window for visible light. Additionally, electron beam excites different optical centers at the same time, which leads to complications in interpretation of the spectra. By contrast, selective excitation is allowed in PL by choosing proper excitation wavelengths.

Commonly, the optical centers studied in diamond are vibronic centers - an interaction between vibrational and electronic transitions. Therefore the absorption and luminescence spectra consist of a sharp "zero-phonon line" corresponding to the purely electronic transition and a broad vibronic band caused by transitions involving phonons (see §3.2.3). The zero-phonon line (ZPL) is broadened at high temperatures, and thus most absorption

and luminescence spectra involving zero-phonon lines are recorded at liquid nitrogen temperature and conventionally the position and width of a ZPL are given for 77 K. The spectral shape of the electron-phonon transitions is unique for each optical center, and is used for defect identification.

3.2.3 Color centers

If the excited and ground states of a defect are both located within the band gap and an optical dipole transition is allowed between them, this defect is luminescent under excitation. Those defects give the crystal a characteristic color, and are thus called color centers. The wide band gap of diamond gives rise to the presence of more than 100 different color centers. A significant fraction has been analyzed in detail so that their charge and spin states are known under equilibrium conditions [71].

As discussed in the introduction of absorption and luminescence experiments on diamond, most color centers are vibronic centers. The optical spectra of them can be explained by the configuration coordinate diagram (figure 3.4(a)) [68]. At low temperatures, only the lowest vibronic level of the ground state is populated. With absorption of a photon, a transition to nth level of the excited state takes place, which leads to an absorption peak at $E = E_0 + n\hbar\omega$ with E_0 the energy difference between ground and excited state and ω the phonon frequency. The most probable transition is the vertical one, A $\rightarrow$B in figure 3.4(a), with $n = S$. The color center can then relax to C by emission of S phonons, decay to D by emission of a photon, and relax back to A by emission of another S phonons.

A very important transition occurs between the levels $m = 0$ and $n = 0$. This is the zero-phonon line (Z in 3.4(a)). It is a purely electronic transition, and, in principle, its width is determined by the luminescence lifetime. In practice it is broadened by random strains in crystal. Nevertheless, it is considerably sharper than the phonon-assisted transitions. With increasing temperature, transitions between the vibronic levels with the same but nonzero quantum number begin to contribute to absorption and luminescence. Those transitions have a similar energy as the ZPL but a much broader line width. Thus the width of the ZPL increases with temperature. At high temperatures or strong electron-phonon coupling the ZPL is weak compared to the phonon sidebands.

In absorption the phonon-assisted transitions occur at higher energies than the ZPL, whereas in emission they are at lower energies, which leads to a mirror symmetry relative to the ZPL. As an example, luminescence and absorption spectra of the NV^- center measured at 80 K are shown in figure 3.4(b) and (c). If there is non-linear coupling or the Jahn-Teller effect, such
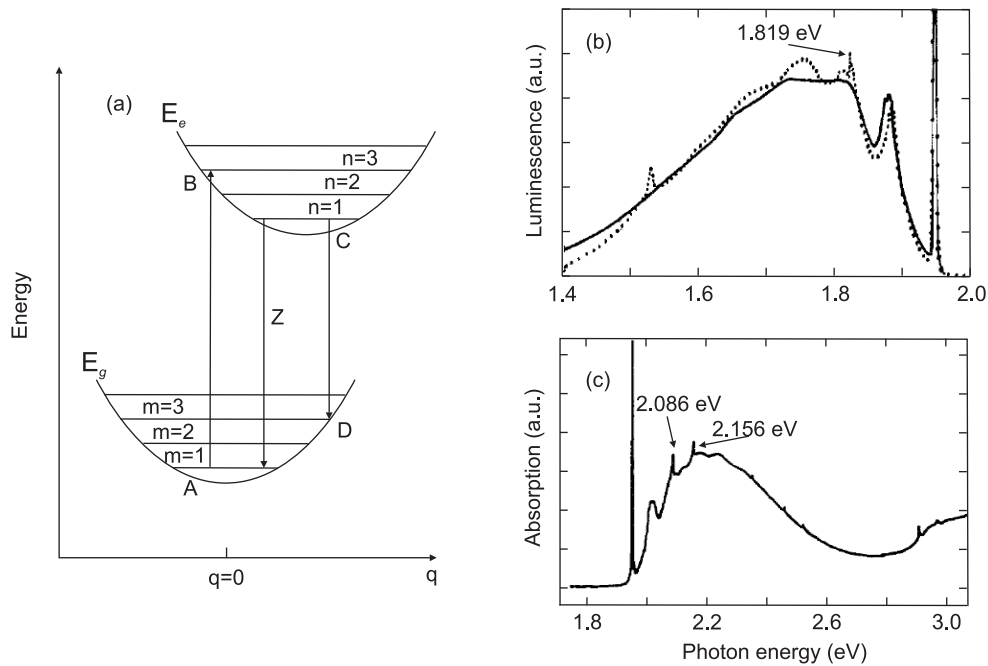
Figure 3.4: (a) A configuration coordinate diagram showing the ground (E_g) and excited (E_e) electronic states with their vibrational levels. After [68]. (b) Measured 80 K luminescence spectrum (dots) of NV^- center compared with luminescence spectrum calculated from the absorption spectrum (full curve). (c) Measured 80 K absorption spectrum. In (b) and (c) some independent zero-phonon lines are also present. After [72].

symmetry is destroyed.

The PL lifetime of a color center is primarily determined by the optical dipole moment. It can also be influenced by the existence of competitive non-radiative channels or strains in lattice. For this reason, the PL lifetime of SiV centers is significantly shorter in polycrystalline than in monocrystalline samples [50]. Due to the involvement of phonons, the PL lifetime generally decrease with temperature.

Charge states are another important property of a color center. Generally, different charge states give rise to completely different spectra. For example, while the neutral NV center produces an emission band with a ZPL at 575 nm, the ZPL of negatively charged NV center lies at 638 nm [73]. In semiconductors with shallow donors and acceptors the equilibrium charge states of defects are determined by the position of the Fermi-level. However, in an insulating material like diamond, the correct charge state of an individual color center does not merely depend on the calculated position of the Fermi-level. Instead, the charge state is influenced by the proximity of the

color center to a donor (or acceptor). Therefore the charge state of a color center depends on the concentration of isolated substitutional nitrogen and boron. Many color centers can be present in two different charge states in the same diamond [74].

Some color centers have non-degenerate spin states. If the luminescent transition is spin selective, a fast detection of single electron spin state is possible via fluorescence of a single color center, which leads to applications of single color centers in quantum information processing [75]

3.3   Ion implantation

Ion implantation is a technique in which accelerated ions are forced into a solid target. It allows to introduce any impurities into any desirable materials thus modifying its properties, regardless of the phase diagram, solubility and thermodynamic equilibrium considerations. However, the implanted impurities are restricted to the region close to the surface, and consequently the achievable effects are localized. Since the ion energies exceed typical binding energies in a solid by many orders of magnitude, ion implantation is always accompanied by severe damage to the target. In most cases, such damage is undesirable and needs to be removed by annealing.

Ion implantation is the only technique to effectively modify diamond after its growth. It is widely used to realize *p*-type and *n*-type doping of diamond [76]. It is also employed for micro-machining of diamond [77]. Below, the general processes involved in ion implantation and the peculiarity of diamond are discussed.

3.3.1   General concepts

An energetic ion penetrating any solid loses its kinetic energy through scattering events due to the Coulomb interaction of the ion with the nuclei and electrons. The energy loss determines the final penetration depth of the projectile and the amount of damage of the lattice. A detailed theoretic description of energy loss of ions in solid is given by Lindhard *et al.* in the commonly called LSS theory [78].

Generally, the slowing-down of an ion is treated in terms of the "stopping power" $\mathrm{d}E/\mathrm{d}z$, defined as the energy loss of an ion traversing a distance $\mathrm{d}z$ into the solid. It is given by

$$\frac{\mathrm{d}E}{\mathrm{d}z} = N \int T \mathrm{d}\sigma, \tag{3.2}$$
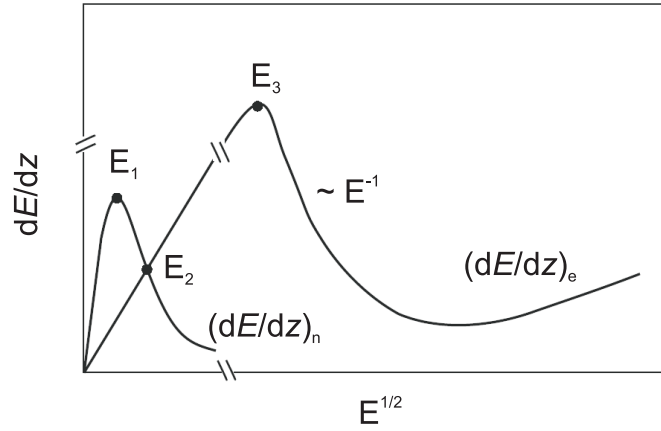
Figure 3.5: Qualitative dependence of stopping powers on the kinetic energy of ions. $(dE/dz)_e$ for electronic processes and $(dE/dz)_n$ for nuclear processes. Redrawn after [79, p. 4].

where $d\sigma$ denotes the collision cross-section, T is the energy lost by the ion in the course of a collision event, and N is the density of scattering centers of the host material.

The total stopping power is due to both electronic and nuclear processes and can be written as

$$\frac{dE}{dz} = \left[\frac{dE}{dz}\right]_e + \left[\frac{dE}{dz}\right]_n, \tag{3.3}$$

where $[dE/dz]_e$ and $[dE/dz]_n$ are the contributions of electronic and nuclear processes, respectively. Figure 3.5 shows the quantitative dependence of both stopping powers on the kinetic energy of the ion, where E_1, E_2 and E_3 denote the three characteristic energies . The electronic processes are dominated by inelastic scattering. The LSS theory treats the electrons in solids as a free-electron gas which is affected by the positive charge of the projectile. This approach gives rise to an electronic stopping power proportional to the ion velocity. Above E_3, transitions of atomic states in the target must be considered for the electronic stopping, therefore an adequate description is by the Bethe-Bloch theory in the framework of quantum mechanics [80]. For ion implantation the energies of interest are usually below E_3. The LSS theory does not allow deviation of the projectile trajectory due to ion-electron interaction. In contrast, the ion-nucleus interaction results in both energy loss and significant change of the projectile trajectory. The nuclear processes are mainly elastic scattering, and the cross-section for the ion-nucleus interaction is given by the Rutherford cross-section. As illustrated in figure 3.5, nuclear stopping is dominant at low energies of the projectile,

while electronic stopping dominates at high energies. Since the disorder of host atoms is mainly caused by the ion-nucleus interaction, damage to the lattice typically occurs at the end of the ion range.

From the energy loss, the longitudinal ion distribution in target, the so called ion range, can be calculated as follows

$$R = \int_{E_{in}}^0 \frac{\mathrm{d}E}{\mathrm{d}E/\mathrm{d}z}, \tag{3.4}$$

where the integration limits are from the initial ion energy to zero. The slowing-down of an ion is a statistical process. Thus the final locations of ions are also of statistical nature. In order to obtain a simple physical picture, the Gaussian approximation is commonly used for the ion range as

$$n(z) = \frac{\phi}{\sigma_p \sqrt{2\pi}} exp\left[-\frac{(z - R_p)^2}{2\sigma_p} \right], \tag{3.5}$$

where z is measured along the beam direction, ϕ is the ion dose, R_p the mean penetration depth and σ_p its standard deviation (also referred to as the ion range straggling) [81].

More realistic information about the ion range and the related damage is obtained from computer simulations. The most commonly used code is the TRIM program (TRansport of Ion in Matter) developed by Beirsack and Haggermark [82]. The input parameters to TRIM are the experimental conditions, such as ion type and energy, target material, composition and density, and an intrinsic parameter, the displacement energy E_d which is the energy required to remove a target atom from its lattice site. The program is a Monte-Carlo simulation and follows the trajectory of an ion. The target is assumed to have a homogeneous distribution of atoms and a collision event with a target atom is generated randomly according to the type and density of the target. If a target atom gains a kinetic energy exceeding E_d after a collision, the calculation of the ion motion is temporarily stopped and the program traces the target atom cascades till all target atoms come to rest. Then the ion may proceed with its new energy and direction of motion until another statistically selected collision occurs. This procedure continues until the ion loses all its kinetic energy. With the best-known semi-empirical values for the stopping powers, the TRIM program is able to calculate both the final 3D distribution of the ions and also all kinetic phenomena associated with the ion's energy loss, including target damage, sputtering, ionization, and phonon production.

The TRIM simulations of damage cascades created by a single light (C) and a single heavy (Xe) ion with comparable energy are shown in figure 3.6.
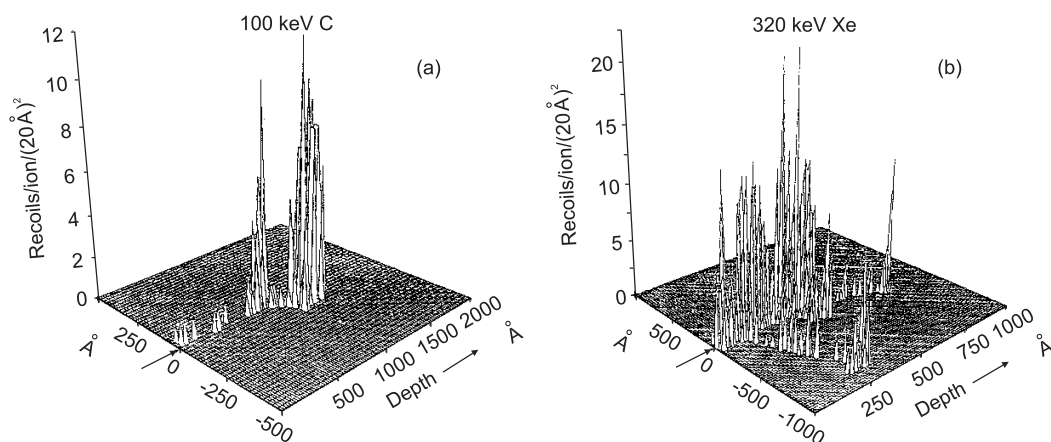
Figure 3.6: Collision cascades following the penetration into diamond of a single 100 keV C ion (a) and a single 230 keV Xe ion (b). After [81].

It is clear to see that the amount and density of damage caused by heavy-ion implantation are much larger than for light-ion implantation.

Although TRIM provides excellent insight into the implantation process and offers valuable information on the state of a target after ion implantation, it ignores some important features in the real implantation. For example, effects due to the periodicity of atoms in a crystal, such as channeling, are neglected by the program. Since recombinative annihilation of defects is not considered in the program, TRIM tends to overestimate the absolute amount of damage.

In most cases the damage induced by ion implantation needs to be annealed. The removal of the elementary defects, the vacancies and interstitials, is achieved by imparting sufficient energy. At high temperatures effective diffusion of the defects is allowed so that they can move and annihilate, or disappear at the surface. Energy is also required to break up complex defect agglomerates, such as dislocation loops. Annealing is usually realized by heating the sample to high temperatures. It can be carried out after implantation in furnaces or during the implantation. In the latter case the formation of some defects is inhibited from the very beginning.

3.3.2   Damage in diamond and its annealing

A peculiarity of diamond is that the diamond crystal with its sp^3 bonded carbon atoms is in a metastable form at ambient conditions, while the stable form is sp^2 graphitic binding. The natural transformation of diamond into graphite occurs at an extremely low rate. However, this process can be

strongly enhanced if sufficient sp^3 bonds are broken.

As discussed above, a lot of damages are induced by ion implantation, which can lead to changes in the bonding configuration resulting in drastic changes in physical and chemical properties. By detection of the occurrence of sp^2 bonds after ion implantation, the basic physics of the passage of ions through matter can be beautifully studied through the particular case of diamond. Nevertheless, for most applications, especially diamond doping, it is desirable to restore the diamond lattice after ion implantation. The most critical issue is avoiding graphitization. The occurrence of graphitization depends on the density of broken sp^3 bonds. The damage threshold , beyond which graphitization occurs during annealing, was found to be 10^{22} vacancies/cm^3 for room temperature implantations [83]. For MeV ion implantation the damage threshold becomes higher, since the damage layer is deeply buried below a relatively undamaged diamond cap, which keeps the damaged region under high pressures and thus retains it from relaxing to graphite [84].

The two elementary damage products - vacancies and interstitials - have different diffusitivies. Carbon interstitials seem to become mobile in diamond at about 50 K, while vacancies probably start to diffuse only at about 700 K [81]. This leads to an imbalance between interstitials and vacancies in the vacancy-rich region. In order to achieve optimal annealing of the crystal, extra carbon atoms may be supplied to the vacancy-rich region.

Generally, annealing of diamond is carried out in vacuum or under protective gas to avoid the reaction with oxygen. Several annealing schemes have been proposed and implemented aiming at achieving electrical activation of implanted potential dopants, such as hot implantation, furnace annealing, pulsed-laser annealing and cold implantation followed by rapid annealing (CIRA) [81]. The last scheme is the most successful. The idea behind relies on freezing-in the point defects by employing low-temperature implantation and effective recombination of interstitials and vacancies by rapid heating to the temperature at which both elementary defects are mobile.

Chapter 4

Experimental setup

This work deals with optical spectroscopy of single color centers in diamond. The most critical point of the experiments is the isolation of a single color center, which is realized by preparing desired color centers in a sufficiently low concentration so that it is possible to address individual centers optically. This optical addressing was performed by using a high-resolution scanning confocal microscope. After a single center had been localized, it was characterized mainly via optical methods. Spectra recorded by a grating spectroscope were used for identification of the color center, and the second-order correlation function $g^{(2)}(\tau)$ was measured with a HBT-Interferometer for verification of the single photon characteristics. In this chapter a detailed description of the experimental setup is given.

4.1   Confocal microscope

The principle of a confocal microscope is to use both point-wise illumination and detection. In practice it is realized by forming the images of an illumination pinhole and a detection pinhole in their common image plane, the object plane. The improvement of resolution of a confocal microscope compared to a conventional light microscope can be simply explained by a principle given by Lokusz [85], which states, in essence, that the resolution can be increased at the expense of the field of view. The field of view is then increased by scanning. The experimental implementation of the confocal principle is illustrated in figure 4.1, where the two pinholes are replaced by single mode fibers with a mode field diameter of 4.6 μm, and their images are formed by the same microscope.

   For clearness, we follow the optical path and begin with the excitation, which is provided by a laser diode. For the choice of the excitation wave-
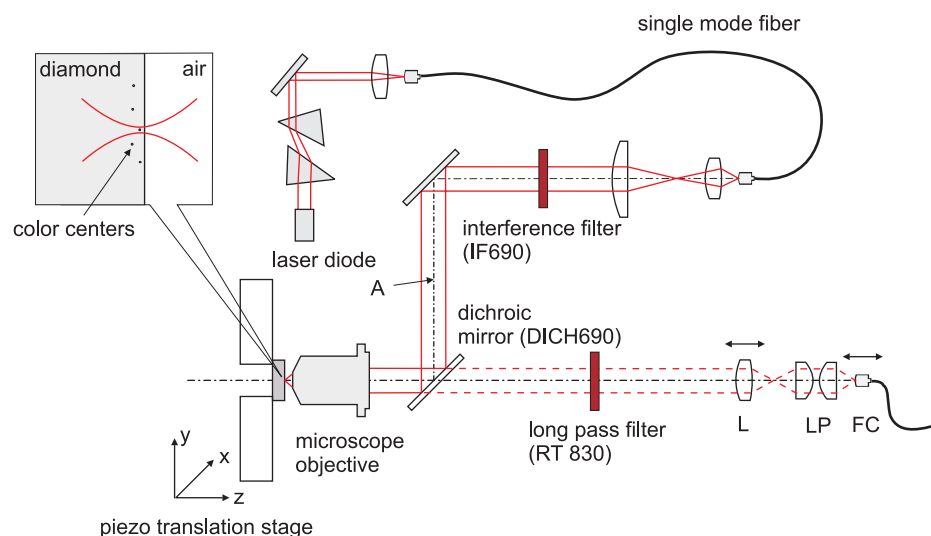
Figure 4.1: Home-made scanning confocal microscope. The red line indicates the optical path of excitation laser and the dashed read lines that of fluorescence light.

length several factors were considered. The confocal microscope is designed to investigate the SiV center which has a ZPL at 738 nm, therefore the excitation wavelength should be shorter than 738 nm. If the SiV centers are fabricated by ion implantation, there are inherently high concentrations of NV centers in the sample. To avoid the fluorescence of NV centers, an excitation wavelength longer than the ZPL of NV centers at 637 nm is necessary. If SiV centers are prepared in a bulk sample, the Raman scattering of diamond lattice should also be taken into account and should not overlap with the SiV spectrum. Finally, the availability of laser diodes led to the choice of a laser diode operating at 690 nm with an output power of 30 mW. Spectral positions of the laser and Raman line are shown in figure 4.2(a), and it can be clearly seen that there is no disturbing light in the main spectral range of the SiV center located around 740 nm.

The profile of the laser diode beam is transformed from elliptic into nearly circular by a prism pair to achieve optimal coupling into the fiber. After leaving the fiber the laser beam is collimated to a beam diameter matching the objective rear aperture. The spectrum of a laser diode consists of a sharp laser line and broad background emission. Although the background emission is negligibly weak compared to the laser line, it is much higher than the fluorescence of a single quantum emitter. To avoid the background emission in the spectral range of interest, an interference filter (IF690) with
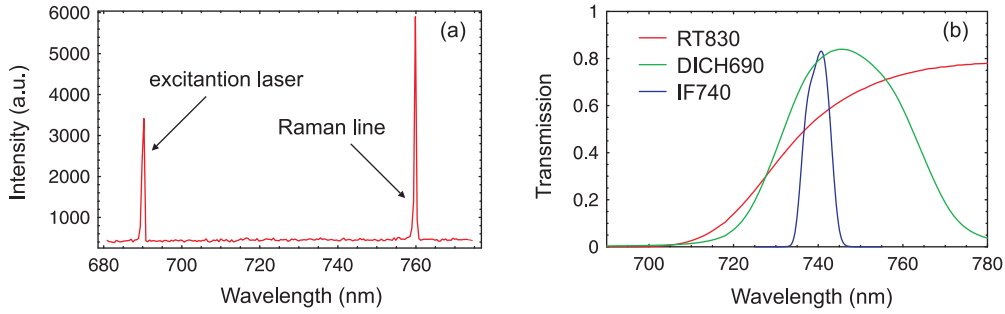
Figure 4.2: (a) Spectrum of the excitation laser and diamond Raman line, where the laser line is strongly attenuated. (b) Transmission of the used optical filters in the setups.

a central wavelength at 690 nm and a FWHM of 10 nm is inserted into the laser beam. At position "A" the excitation power is measured. By adjusting the coupling of laser light into the fiber, continuous tuning of the excitation power from zero to about 10 mW can be achieved.

The laser beam is reflected by a dichroic mirror (DICH690), before it enters the microscope objective. Ideally a dichroic mirror is a long pass filter with an incident angle of 45°. However, such a mirror was quite difficult to fabricate, therefore a band pass filter was used with a transmission window from 720 nm to 780 nm, as shown in figure 4.2(b).

The light is focused by a "PL Fluotar L" microscope objective from Leica Microsystem. It is an infinity-corrected objective with a magnification of 100 and a numerical aperture of 0.75. A decisive reason for choosing this objective is the working distance of 4.7 mm, which allows for the insertion of a solid immersion lens between objective and sample. The size of the focus and consequently the resolution of the confocal microscope are primarily determined by the numerical aperture and wavelength of the light. If the objective is modeled as an ideal focusing lens with an entrance aperture of radius R, the waist of a Gaussian beam at the focus can be calculated as [86, p. 26]

$$w_0 = \frac{R\lambda}{\pi w_e tan(sin^{-1}(\mathrm{NA}))}, \tag{4.1}$$

where λ is the wavelength, w_e the waist of the Gaussian beam at the rear aperture and NA the numeric aperture. In this setup $w_e/R = 0.8$ was chosen, which leads to a w_0 equal to 260 nm. In experiments, the diffraction-limited size of the fluorescence image of a point emitter is conventionally characterized by its full width of half maximum (FWHM), which can be calculated

using the value of w_0 as

$$\text{FWHM} = 2w_0\sqrt{2ln2} = 612 \text{ nm}. \tag{4.2}$$

The measurements of single color centers reveal a FWHM of 625 ± 25 nm which agrees quite well with the theoretic value (see §5.2).

At the position of the focus the diamond samples are mounted on a piezo translation stage which performs the scanning in three spatial directions. This xyz-positioner of the model "TRITOR 102 SG" from Piezosystem Jena operates in closed-loop mode and allows a motion of 80 μm in each direction with a resolution of 2 nm. If a single color center is moved into the focus, it begins to fluoresce. Part of the fluorescence light is collected by the objective and passes through the dichroic mirror.

Finally the fluorescence light is coupled into a single mode fiber and thereby guided to the HBT interferometer or to the spectrometer. Due to the confocal principle collection of stray light is strongly suppressed, however, in case the color centers are located near the surface, a considerable amount of excitation light can still be collected despite the high reflectivity of the dichroic mirror. To reject the excitation light a color glass filter (RT830) was used, whose transmission curve is shown in figure 4.2(b).

One interesting question is how to couple the fluorescence light optimally into the the single mode fiber. The considerations to this question are illustrated in figure 4.3(a), where the objective is again represented as an ideal lens with a focus length of f and an entrance aperture of radius R.

At the focus of the lens there is a point emitter and the emitted light is assumed to be a spherical wave. We consider the electric field on the lens plane. Due to cylindrical symmetry, this problem can be reduced to one dimension with the parameter r. The spherical wave leads to an electric field on the left side of the lens plane as

$$E_l(r) = \frac{E_0}{\sqrt{f^2 + r^2}} e^{-ik\sqrt{f^2 + r^2}}, \tag{4.3}$$

where E_0 is a constant and k the wave vector of the light. According to geometric optics, collimated light is expected on the right side of the lens plane. This means the wave front is transformed from spherical to plane. Therefore, the function of the ideal lens is to eliminate the complex phase factor in eqn (4.3). In contrast, the amplitudes of the electric field are kept unchanged due to energy conservation. Thus the electric field on the right side of the lens plane can be expressed as

$$E_r(r) = E_0\sqrt{\pi/f} \cdot p_1(r) = E_0\sqrt{\pi/f}\frac{1}{\sqrt{\pi/f}\sqrt{r^2 + f^2}}, \tag{4.4}$$
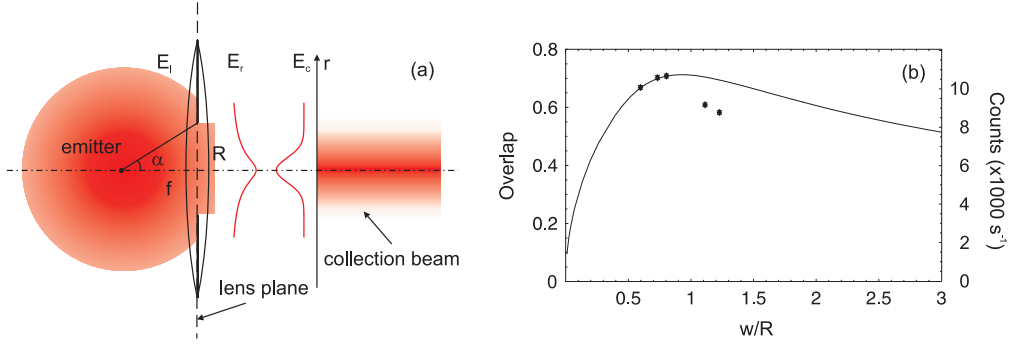
Figure 4.3: (a) Schematic presentation of the situation of coupling fluorescence light into a single mode fiber. (b) Theoretical prediction of the coupling efficiency (line) and measured SiV fluorescence intensity (dots) in dependence of the waist of the Gaussian collection beam.

where the factor $\sqrt{\pi/f}$ is introduced to satisfy the normalization condition $\int_{-\infty}^{\infty} p_1^2(r)\mathrm{d}r = 1$.

The light field which can be coupled into a single mode fiber has a Gaussian profile. We assume a nearly plane wave front for the collection beam so that the coupled electric field can be written as

$$E_c(r) = E_0' \cdot p_2(r) = E_0' \frac{1}{\sqrt{2\pi}w} e^{-\frac{r^2}{2w^2}}, \tag{4.5}$$

where w is the waist of the Gaussian beam at the entrance aperture. It is obvious that $\int_{-\infty}^{\infty} p_2^2(r)\mathrm{d}r = 1$.

The possibility of coupling the fluorescence light into the single mode fiber is considered as the overlap of the electric fields E_r and E_c. Thus a coupling efficiency η is defined as

$$\eta = \int_{-R}^{R} p_1(r)p_2(r)\mathrm{d}r, \tag{4.6}$$

where $R = f \cdot tan\alpha$ is radius of the rear aperture of the microscope objective. Since $p_1(r)$ and $p_2(r)$ are both normalized, η has a value between 0 and 1. With the given parameters of the objective, η was calculated in dependence of w/R, and the results are illustrated by the line in figure 4.3(b). There is a maximum at $w = 0.93R$. In the considerations above electric fields are treated as scalar fields. This is justifiable, because only electric fields with parallel wave fronts are involved and there is no preferred polarization in the system.

For an experimental investigation an aspheric lens L and a lens pair LP were inserted in front of the fiber coupler FC, as shown in figure 4.1. L

and FC are mounted on translation stages so that they can be moved along the optical axis. With the proper adjustment of the positions of L and FC, a Gaussian beam with nearly plane wave front and tunable waist can be defined. A sample with high SiV center concentration was mounted into the confocal microscope, and at a certain spot the fluorescence intensity was registered for five sets of positions of L and FC. Afterwards, laser light of 730 nm was coupled into the fiber from the other end to simulate the collection beam. The corresponding waist was measured at the objective rear aperture for each adjustment. The results are represented in figure 4.3(b) by the dots. The magnitudes of intensity are scaled to match the theoretical curve. It can be clearly seen that the maximal light collection efficiency occurs at the predicted position. With increasing waist the beam diameter becomes comparable with the size of the aspheric lenses, thus considerable part of the beam can be cut off. This is probably the reason for the deviation of the measured values from the theoretical predictions.

Besides the optical resolution, the overall detection efficiency is also a crucial issue of the confocal microscope. Since we do not have a point emitter with known quantum yield for calibration, we give an estimation for the upper bound of the detection efficiency. Diamond has a refractive index n_d of 2.41, which hinders the collection of the light emitted in a bulk sample in two ways: reducing the numeric aperture of the microscope objective by a factor of n_d and causing reflection at the diamond surface. Considering that photons are emitted in all directions in spontaneous emission, the ratio of the photons which can be collected by the microscope objective to the whole emission is calculated as

$$\frac{1 - cos(sin^{-1}(\mathrm{NA}/n_d))}{2} = 0.0497. \tag{4.7}$$

The reflectivity of the diamond surface is estimated using the Fresnel formula of reflection for perpendicularly incident light to be

$$\frac{(n_a - n_d)^2}{(n_a + n_d)^2} = 0.17, \tag{4.8}$$

where the diffraction index of air $n_a = 1$ is used.

According to manufacturer information the microscope objective has a transmission of about 0.7. The transmissions of the dichroic mirror (DICH690), color glass filter (RT830) and interference filter (IF740) at 740 nm were determined as 0.8, 0.6 and 0.8 (see figure 4.2(b)). Finally, the detection efficiency of the APDs used is estimated to be 0.56 [87]. The only unknown factor is the efficiency of coupling the light collected by the microscope objective into the single mode fiber. The theoretic curve shown in figure 4.3(b) suggests an upper bound of 0.7 for it. By multiplying all factors together, we come to
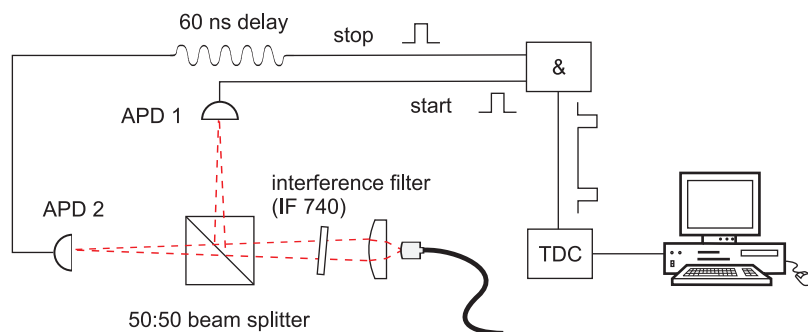
Figure 4.4: Experimental setup of a HBT interferometer.

an overall detection efficiency of 0.35%. Due to experimental imperfections and additional reflection at the lenses used, the real efficiency of the setup is slightly below this value.

4.2 HBT setup

The experimental implementation of an HBT interferometer is sketched in figure 4.4. The fluorescence light is coupled into the interferometer via a single mode fiber. It is split up by a 50:50 beam splitter. At each output arm of the beam splitter there is an actively quenched Si-APD from Perkin-Elmer. The dark counts of APD 1 and APD 2 are 140 and 160 s^{-1}, respectively. For the measurement of SiV centers an interference filter (IF740) was inserted into the setup to suppress background light, such as the excitation laser and its Raman scattering. IF740 was turned to an angle of 85° to the optical axis in order to avoid optical crosstalk between the APDs. The transmission curve of IF740 is shown in figure 4.2(b).

As discussed in §2.1.3 the intensity correlation between the two output arms has to be measured to get the second-order correlation function of the input field. Experimentally it is realized by recording a histogram of time differences τ between two subsequent detection events of APD 1 and APD 2. At the detection of a photon, APD 1 gives a TTL signal which is defined as a "start" signal. A "stop" signal is given by APD 2. A long cable is used to introduce a delay of about 61 ns to the stop signals so that $g^{(2)}(\tau)$ can also be measured for negative τ. The start and stop signals are added together by a &-gate. The &-gate generates an artificial stop signal at 120 ns after a start signal, in case no photon is detected for the stop signal during the time span. This function leads to a more efficient measurement [88, p. 40], however it also limits the measurable time range.
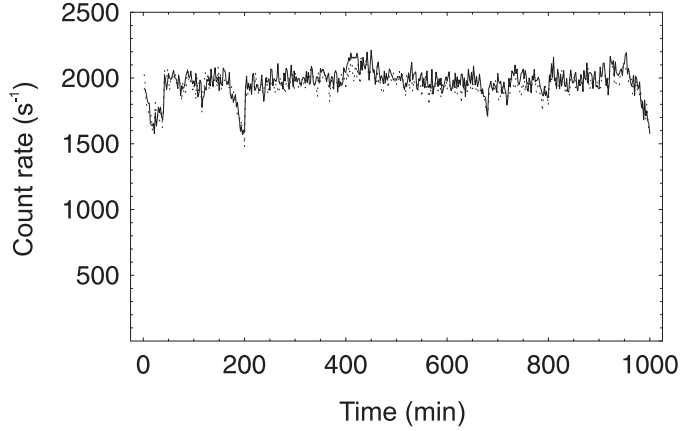
Figure 4.5: Count rate of a single SiV center registered over night.

Since the luminescence lifetime of the investigated color centers is of the order of several nanoseconds, the time window of 120 ns is an acceptable compromise. A time to digital converter (TDC) of the model GP-1 from Acam-Messelektronik is used for measuring time intervals between start and stop signals and recording histograms. Finally, the data is read out by a computer.

In case the average distance between two subsequent photons is large compared with the τ of interest, the registered histogram is equal to $\langle \hat{a}^\dagger(t)\hat{a}^\dagger(t+\tau)\hat{a}(t)\hat{a}(t+\tau)\rangle \cdot T \cdot t_{bin}$, where $\hat{a}^\dagger$ and $\hat{a}$ are creation and destruction operators of the input field respectively, T the integration time and t_{bin} the length of the time bins [89]. In order to obtain $g^{(2)}(\tau)$ defined in eqn (2.21), the histogram is normalized by a factor of $r_1 \cdot r_2 \cdot T \cdot t_{bin}$, where r_1 and r_2 are the average count rate of APD 1 and APD 2, respectively.

Due to the low intensity of a single quantum emitter, it takes long time to measure $g^{(2)}(\tau)$, therefore it is crucial to keep the position of the sample stable with a precision of a half micrometer over days. In practice the whole measurement time is divided into short periods, typically 40 minutes long. Between the periods the position of the sample is adjusted automatically. The count rate of a single SiV center registered over 17 hours is shown in figure 4.5. At some points the count rate drops, because the center drifts out of the focus. However, owing to the automatic adjustment the count rate is kept constant.

Theoretically a single photon source exhibits a vanishing value of $g^{(2)}(0)$, however experimentally measured second-order correlation function often shows some residual value at $\tau = 0$, which essentially depends on the nature of the source. For single color centers the random background emission
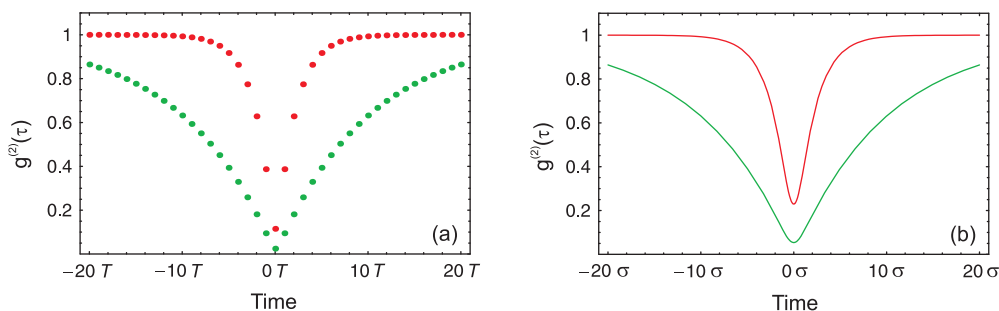
Figure 4.6: Impact of systematic errors on measurement results of $g^{(2)}(\tau)$ due to the finite time resolution T of the DTC (a), where the red dots are calculated for $\tau_0 = 2t_{bin}$ and the green dots for $\tau_0 = 10t_{bin}$, and due to the time jitter of photon detection σ (b), where the red line is plotted for $\tau_0 = 2\sigma$ and the green line for $\tau_0 = 10\sigma$.

of the diamond sample plays a crucial role. Its impact on $g^{(2)}(\tau)$ is discussed in §5.2. On the other hand, imperfections of the setup can also contribute to $g^{(2)}(0)$. We treat this effect extensively here, since $g^{(2)}(0)$ is the ultimate criterion to demonstrate the single photon characteristics, according to eqn (2.19). The systematic errors mainly occur in the determination of the time intervals between start and stop signal. We consider two major error sources: time resolution of the TDC and time jitter of the APDs.

We assume that the TDC uses a time bin of t_{bin}. In histograms all events within the time interval $[\tau_i - t_{bin}/2, \quad \tau_i + t_{bin}/2]$ are all summed up for $g^{(2)}(\tau_i)$, where τ_i are the discrete time points. For an ideal $g^{(2)}(\tau)$ defined in eqn (2.43) the value of $g^{(2)}(\tau_i)$ is calculated as

$$g^{(2)}(\tau_i) = \frac{1}{t_{bin}} \int_{\tau_i - t_{bin}/2}^{\tau_i + t_{bin}/2} (1 - e^{-|\tau|/\tau_0}) d\tau. \qquad (4.9)$$

The measurement results predicted by eqn (4.9) are calculated for two $g^{(2)}(\tau)$ with τ_0 equal to $2t_{bin}$ and $10t_{bin}$, respectively, and are shown in figure 4.6(a). If $\tau_0 \gg t_{bin}$, the effect of finite time resolution is negligible. However, if τ_0 is comparable to t_{bin}, considerable deviation of $g^{(2)}(0)$ from zero appears.

The used TDC provides three lengths of time bin for recording histograms: 150 ps, 300 ps and 600 ps. However, the width of a single "least significant bit" (LSB) varies periodically. A narrow LSB follows a broad LSB and vice versa. This effect becomes stronger and results in a worse differential non-linearity for shorter time bins. Only the time bin of 0.6 ps delivers satisfactory results [88, pp. 41-44]

The time jitter of the photon detection is defined as the variation of the time intervals between arrival of one photon at the APD and recognition of
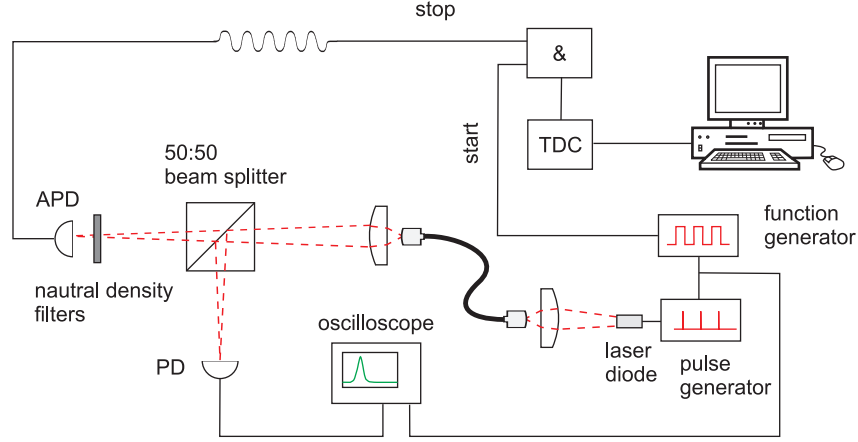
Figure 4.7: Experimental setup for determination of the time jitter in photon detection.

the corresponding TTL signal by the TDC. It introduces additional uncertainties into the measurements. Mathematically this effect is considered as a convolution of $g^{(2)}$ with a response function j of the system. The measured $g_m^{(2)}$ is thus expressed as

$$g_m^{(2)}(\tau) = \int_{\infty}^{\infty} g^{(2)}(\tau')j(\tau - \tau')\mathrm{d}\tau'. \qquad (4.10)$$

We assume a Gaussian response function for the system, i.e.

$$j(\tau - \tau') = \frac{1}{\sqrt{2\pi}\sigma}e^{-\frac{(\tau-\tau')^2}{2\sigma^2}}. \qquad (4.11)$$

σ is a parameter which is to be determined experimentally. $g_m^{(2)}(\tau)$ is plotted in figure 4.6(b) for $\tau_0 = 2\sigma$ and $\tau_0 = 10\sigma$. The impact on $g_m^{(2)}(\tau)$ is significant, in case τ_0 is comparable to σ.

The experimental setup to determine the parameter σ is shown in figure 4.7. A high speed pulse generator from AVTECH was triggered by a function generator which delivers a square waveform with a repetition rate of 700 kHz. For each trigger signal the high speed pulse generator creates a short voltage pulse with a height of 2.5 V and a FWHM of about 200 ps. Added onto an offset, the voltage pulses were used to drive a laser diode. The offset keeps the laser diode just under its lasing threshold so that it can be driven fast. To avoid reflection of electric signals, the differential resistance of the laser diode was matched to be 50 Ω.
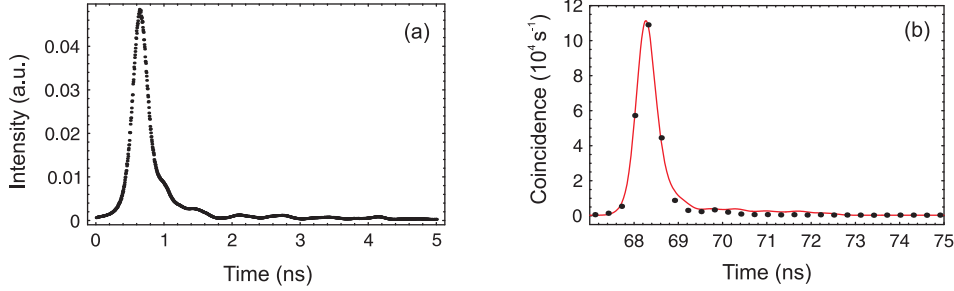
Figure 4.8: (a) Averaged form of the laser pulses. (b) Histogram of time intervals between trigger signals and output signals of APD 1 (dots) and the fitting function (line).

The laser pulses are split up by a 50:50 beam splitter. At one output arm there is a fast photodiode which monitors the laser pulses. The form of the laser pulses was displayed by an oscilloscope. The oscilloscope was also used to register a histogram of arrival times of the laser pulses in respect to the trigger signals. A standard deviation of 32.8 ps was determined for the arrival time of the laser pulses. As shown below this uncertainty is negligible compared with the time jitter of the APDs. An APD stands at the other output arm. The laser pulses which reach the APD were attenuated strongly so that the average photon number per pulse was much smaller than 1, so that the response of the APD reflects the form of the incoming laser pulses.

The same electronics used in the HBT setup was employed to record a histogram of the time intervals between trigger signals and output signals of the APD. This histogram reflects the form of the laser pulses including the time jitter of photon detection. An averaged form of the laser pulses recorded by the oscilloscope is presented in figure 4.8(a). It defines a discrete function $p(t_i)$. The measured histogram for APD 1 is shown in figure 4.8(b), and to fit the data a function $p'(t)$ was defined as

$$p'(t) = a \sum_i p(t_i) \cdot \frac{1}{\sqrt{2\pi}\sigma} e^{-\frac{(t-b-t_i)^2}{2\sigma^2}} (t_{i+1} - t_i), \tag{4.12}$$

where a, b and σ are fitting parameters. The integral of the convolution in eqn (4.10) is replaced by a sum, since $p(t)$ was measured in discrete values. A least square fitting gives $\sigma_1 = 163 \pm 0.5$ ps. The fitting function is presented by the line in figure 4.8(b). Analogously, $\sigma_1 = 160 \pm 0.5$ ps was determined for APD 2. According to Gaussian error propagation, the parameter σ in eqn (4.11) is calculated as

$$\sigma = \sqrt{\sigma_1^2 + \sigma_2^2} = 228.4\,\text{ps} \tag{4.13}$$

For a realistic estimation of the residual value of $g^{(2)}(0)$ caused by systematic errors, we consider it for an ideal second-order correlation function with $\tau_0 = 1.2$ ns, which is a typical value for single SiV centers. With a time bin of 0.6 ns $g^{(2)}(0)$ is calculated as

$$g^{(2)}(0) = \frac{1}{0.6} \int_{-0.3}^{0.3} \left(\int_{-\infty}^{\infty} (1 - e^{-|\tau'|/1.2}) \frac{1}{\sqrt{2\pi}0.23} e^{-\frac{(\tau-\tau')^2}{2\cdot 0.23^2}} \mathrm{d}\tau' \right) \mathrm{d}\tau = 0.14$$

(4.14)

4.3   Spectrometer

As discussed in §3.2.2, photoluminescence spectra are often employed to identify color centers. In order to measure the fluorescence spectra of single color centers a grating spectrometer was built using a Si-APD for photon detection. The setup is shown in figure 4.9(a).

The fluorescence light is coupled into the spectrometer via a single mode fiber. The beam is expanded by an achromatic lens to an diameter of 14 mm. The light illuminates a ruled diffraction grating with grooves of 1200 lines/mm. The blaze angle of the grating ensures a high efficiency in the range from 600 nm to 800 nm. The grating is mounted on a motorized rotation stage, which is controlled by a computer. The light in the 1. order of diffraction is reflected by a silver mirror, and then focused by a lens with a focus length of 750 mm. At the focus there is an APD which detects the light intensity. Signals from the APD are also guided to the computer. By registering the rotation stage position and the corresponding intensity measured by the APD, a spectrum of the incoming light can be constructed.

An important issue of a spectrometer is its spectral resolution. There are two factors limiting the performance of a grating spectrometer. Physically, the spectral resolution of a grating is predicted according to the Reyleigh criterion as [90, p. 703]

$$\frac{\lambda}{\Delta\lambda} = mN,$$

(4.15)

where λ is the wavelength of incoming light, m the diffraction order and N the numbers of illuminated lines of the grating. The experimental conditions lead to a resolution of 0.44 nm at 740 nm.

In the experimental implementation the spectral resolution is transformed into the resolution of geometric angles. The APD used has a chip size of 0.5 mm. Combined with the focus length of the lens, it defines the smallest resolvable angle $\Delta\theta$ as 0.038°. For a grating with a distance d between two adjacent groves, the equation describing the first order diffraction is
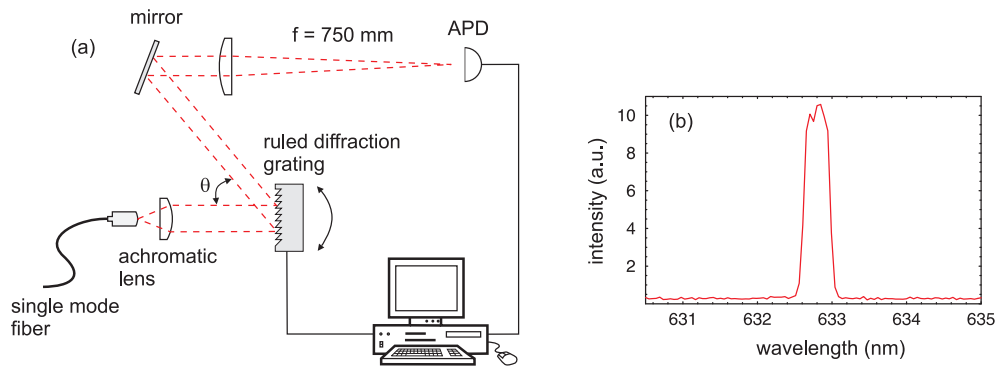
Figure 4.9: (a) Experimental setup of the grating spectrometer. (b) Spectrum of a He-Ne laser measured by the spectrometer.

$\lambda = d \cdot sin\theta$, according to which the measured full width of a monochromatic laser line by this spectrometer is given by

$$W = d \cdot cos\theta \, \Delta\theta. \tag{4.16}$$

To calibrate the spectrometer a He-Ne laser was employed. The full width of the laser line located at 632.8 nm is calculated to be 0.50 nm, which agrees well with the measured value, as shown in figure 4.9(b). The plateau in the spectrum indicates the finite size of the APD-chip. Considering the physical limitation of the spectral resolution, $\Delta\theta$ is fine enough.

The width of the ZPL of color centers at room temperature is of the order of several nanometers, therefore the resolution of the grating spectrometer is sufficient for the measurements.

Chapter 5

Single SiV centers

Spectroscopy of single SiV (silicon vacancy) centers in diamond is the major subject of this thesis. The SiV centers have several advantageous properties for the usage as a single photon source. A brief introduction of these properties is given as a start. Single SiV centers have been fabricated in single-crystalline natural IIa diamond and their capability of emitting single photons has been demonstrated [28]. However the efficiency of single photon generation was found to be rather low. In order to improve the efficiency different approaches have been tested. On the one hand, since SiV centers have non-fluorescing charge states causing emission intermittency, nitrogen doping was carried out to manipulate the occupancy of the charge states. On the other hand, methods to improve the collection efficiency of fluorescent light were investigated, including the use of a solid immersion lens (SIL) for bulk samples as well as diamond nanocrystals.

5.1 Properties of SiV centers

Strong narrow-line luminescence with an emission energy of 1.681 eV (738 nm) was first observed in 1981 by Vavilov *et al.* in cathodoluminescence (CL) investigations of CVD homoepitaxial diamond layers and polycrystalline diamond films [91]. Since then, this luminescence has been reported in films grown by a variety of CVD methods including hot-filament [92], oxygen-acetylene combustion [93] and microwave-plasma [94]. The appearance is so universal that the color center responsible for this luminescence is considered to be characteristic of CVD diamond.

For a long time there had been confusion about the origin of the color center. It had been incorrectly regarded as the GR 1 center (neutral vacancy), since the GR 1 center has a ZPL at a similar energy (1.673 eV) [92, 93].

However, Ruan et al. showed that the 1.681-eV line is stable up to 1350 °C [94], while the GR 1 center is destroyed by a 600 °C annealing in natural diamond [95]. Zaitsev *et al.* observed the CL spectrum in natural diamond after silicon implantation, and they suggested a model consisting of two silicon atoms for the center, since the luminescence intensity was observed to be proportional to the square of the silicon dose [91]. Collins *et al.* also implanted diamond with ^{29}Si atoms and confirmed that silicon is involved in the color center [96]. Furthermore, Collins *et al.* proposed that the center is formed by trapping a vacancy at a silicon impurity. This conclusion was derived from the observation that the intensity of the 1.681-eV line increased when the photoluminescence (PL) line of the GR 1 center is annealed [97]. In 1995, Clark *et al.* verified unambiguously that the color center is related to silicon impurity. They showed that the absorption and PL spectra have a 12-line fine structure which can be divided into three groups. The relative strengths of the optical absorption lines for the groups are the same as the ratio of the abundances of the natural isotopes of silicon, ^{28}Si, ^{29}Si and ^{30}Si [98]. For the structure of the color center Goss *et al.* proposed a model with a Si atom at the center of a split vacancy as shown in figure 5.1(a), and calculated a radiative lifetime which seems to agree with the experimental data [99]. Therefore this center is also denoted as VSiV by some investigators. However, polarization-resolved PL measurements reveal instead of a C_3, as expected for the model of Goss *et al.*, a C_2 symmetry [100]. Clearly, more measurements, such as electron spin resonance (ESR) and optically detected magnetic resonance (ODMR), should be used to clarify the structure of this color center. To avoid confusion we consistently use the term "SiV center" to label the color center responsible for the 1.681-eV line.

The most striking property of the SiV center is that it exhibits a very weak vibronic structure both in luminescence and absorption, with no mirror symmetry relative to the ZPL [101]. Even at room temperature the majority of the emission is concentrated in the ZPL with a FWHM of about 6 nm. Collins *et al.* determined a Huang-Rhys factor of 0.24±0.02 for the SiV center [97]. The Huang-Rhys factor is a measure for the linear electron-phonon coupling in the system and can be calculated from the ratio of the intensity of the one-phonon peak to the the intensity of the ZPL. For comparison, the Huang-Rhys factor for NV centers is 3.21 [27]. Temperature resolved PL and absorption measurement revealed a ground state splitting of 0.2 meV and an excited state splitting of 1.07 meV. Tunneling between two degenerated states could account for the level doubling [98].

Another extraordinary property of the SiV center is the short luminescence lifetime. It was measured to be 4 ns at 5 K and 2.7 ns at room temperature in the homoepitaxial CVD diamond film and about 1 ns nearly
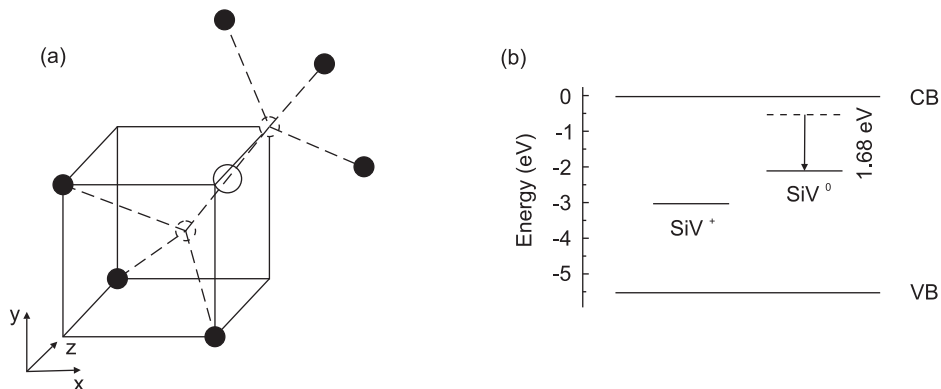
Figure 5.1: (a) A schematic representation of the geometry of the SiV center. the solid circles represent carbon atoms, the empty circle the relaxed silicon site, and the dashed circles the diamond lattice sites. Figure is drawn according to [99]. (a) The position of the charge states of the SiV center in the band gap.

independent of temperature in a polycrystalline CVD diamond film. The measured fluorescence decay curves are all monoexponential over at least one and a half decades [50]. The known lifetimes of some other point defects are significantly larger, for example, the 2.156-eV center with 29 ns, the 2.463-eV center (H3) with 16.7 ns and the 2.985-eV center (N3) with 40 ns [102, p. 178]. The short luminescence lifetime is often ascribed to the existence of non-radiative transitions, which is confirmed by the observation of Feng *et al.* that the intensity of the ZPL of SiV centers drops with increasing temperature [103]. The origin of the non-radiative transitions is not clear yet. Turukhin *et al.* measured the luminescence quantum yield of the SiV center at 77 K by comparing the steady-state PL spectra of CVD diamond films with a dye solution with a known quantum yield. A quantum yield of 0.05 was determined, and combined with a measured luminescence lifetime of 950 ps a radiation transition time constant of $\tau_r = 19$ ns was derived. They found out as well that the non-radiative transitions are not related to the disordered carbon phase and other defects [104].

The charge state of the SiV center is predominantly considered to be neutral, since SiV centers show similar behavior in measurements of photochromism as the neutral NV centers [73]. The fact that the intensity of the ZPL of SiV centers can be increased up to ten times by UV illumination indicates the existence of a more positively charged state. However, no narrow-line absorption, which could be ascribed to that state, could be found

in the range 0.5-5.5 eV [63]. Photoluminescence excitation (PLE) spectra of SiV show oscillatory behavior which can be interpreted as caused by resonant transitions of an electron from the conduction band to the excited state of the SiV center. From the threshold of PLE oscillation the position of the ground state of the SiV center can be derived as $E_c - 2.05$ eV [105]. Photoluminescence quenching spectra reveal the position of the positively charged state as $E_v + 2.5$ eV. The position of both charge states in the band gap is shown in figure 5.1(b).

5.2   SiV centers created by ion implantation

Although the SiV center is considered to be one of the characteristic defects of CVD diamond, its appearance in natural diamond is quite rare. The search for single SiV centers was started in CVD diamond. However, previous investigation of free-standing CVD diamond windows showed a concentration of SiV centers that is too high to address single ones optically [88]. Therefore we chose the method of ion implantation of natural diamond to create SiV centers in a reproducible manner. Ion implantation allows a precise control of the position as well as the concentration of the created defects. The procedure for the fabrication of SiV centers via ion implantation had been developed before [106]. In the scope of this work, the ion dose, at which the optical addressing of single SiV centers by the confocal microscope become feasible, was determined.

   The ion implantation was carried out in the Dynamitron Tandem Laboratory (DTL) of the Ruhr-University of Bochum. The implanted samples are natural IIa diamond windows with dimensions of 0.5 x 0.5 x 0.25 mm^3. The top and bottom faces are polished along the (100) plane. One of the main faces was implanted with 10 MeV Si^{2+} ions at room temperature. The high ion energy was chosen to achieve a large penetration depth to avoid the influence of any surface effects on the SiV centers. The longitudinal range and range straggling of the silicon ions were estimated by a computer simulation with SRIM[1] (Stopping and Range of Ions in Matter) to be 2.35 ± 0.083 μm [107]. The results are shown in figure 5.2. Post-implantation annealing was carried out at 1000 °C for 5 min in vacuum. Samples were washed in a solution of $K_2Cr_2O_7$:H_2SO_4 at 180 °C for 2 min to remove the graphite layer formed during the annealing process.

   The samples were mounted in the confocal microscope with the implanted surface perpendicular to the optical axis. According to the results of the SRIM simulation the position of the SiV centers is expected to be very close

---

[1]downloaded from www.srim.org

to the surface. Therefore two-dimensional scans were carried out on the implanted surface of a sample which had been implanted by an ion dose of 10^9 cm^{-2}.

A 2D scan of a single SiV center is shown in figure 5.3. To determine the size of the point-like image, the fluorescence intensity along the white line in the 2D scan was registered and shown in figure 5.4(a). The data can be well described by a Gaussian curve with a FWHM of 622 ± 25 nm, which agrees with the expected diffraction-limited transverse resolution of the confocal microscope. At the position of maximal intensity in the 2D scan, a scan along the optical axis was made as well. This scan is shown in figure 5.4(b). Outside the sample (left of the central peak), the measured count rates correspond to the dark counts of the APDs. Additional counts on the right side of the peak are mostly due to Raman scattering of the excitation laser in the bulk diamond. The position of the central peak indicates that this SiV center is indeed located near the surface. Fluorescence spectra were measured at the maximum and at a dark region in the 2D scan and are shown in figure 5.5(a). The ZPL of the SiV center at 738 nm is clearly visible. Due to the low fluorescence intensity the vibronic sidebands are not resolved.

To evaluate the photon statistics of the fluorescence light, the second-order correlation function was measured by the Hanbury-Brown-Twiss setup.
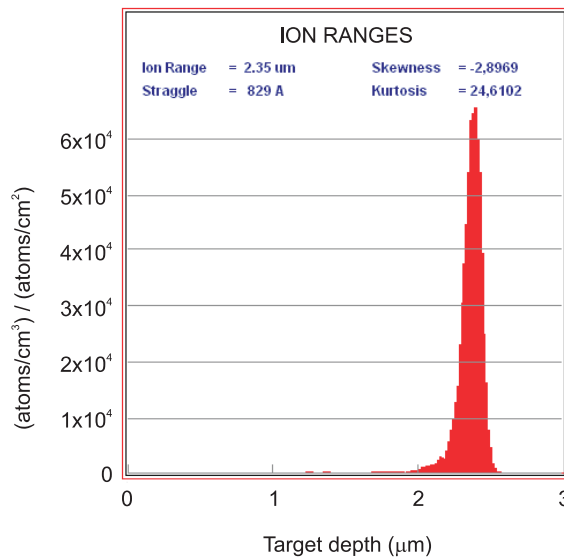
Figure 5.2: Results of a SRIM simulation of the longitudinal ion range for 10 MeV silicon ions implanted in diamond. The position of the diamond surface is located at zero on the x-axis.
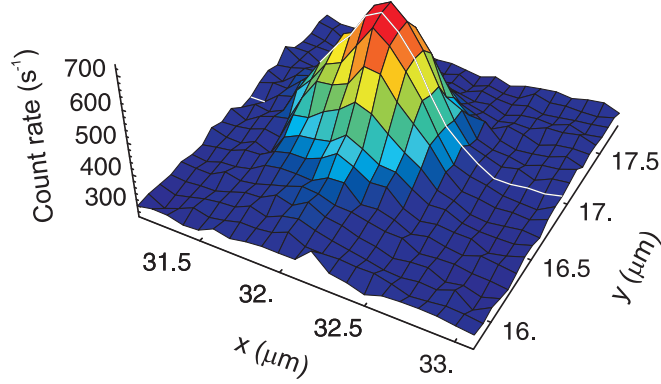
Figure 5.3: A two-dimensional scan on a single SiV center.

The normalized photon coincidence rate histogram is presented in figure 5.5(b). The minimum at the time delay of 60 ns, for a simultaneous detection of two photon, indicates the single photon characteristic. However, the effect of correlated emission is clearly visible as well. Therefore we employ the three-level system discussed in §2.3 to describe the internal structure of the SiV center.

Because the photon detection events are not only contributed by the fluorescence light, but also by the dark counts of the APDs and scattering processes in the diamond, the $g^{(2)}(\tau)$ derived in eqn (2.61) must be modified to fit the experimental data. Assuming that background detection events follow a Poissonian distribution, we introduce a fit function given by the
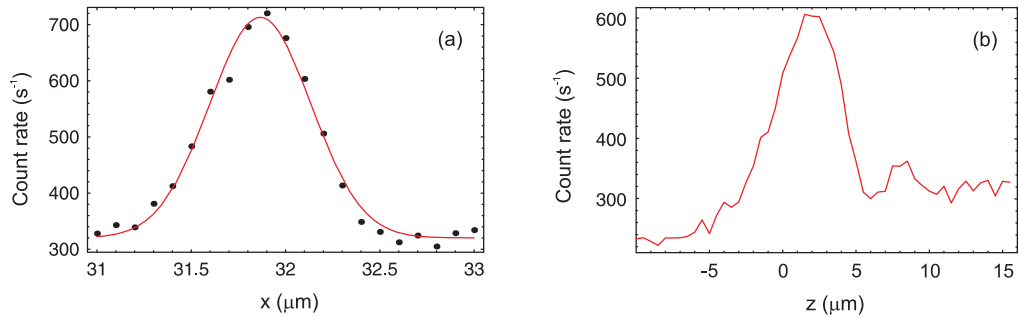
Figure 5.4: (a) Fluorescence intensity profile in a transverse direction of s single SiV center. The red line represents the Gaussian fit function. (b) Scan of the SiV center along the optical axis. the diamond surface is located around $z = 0$ μm.
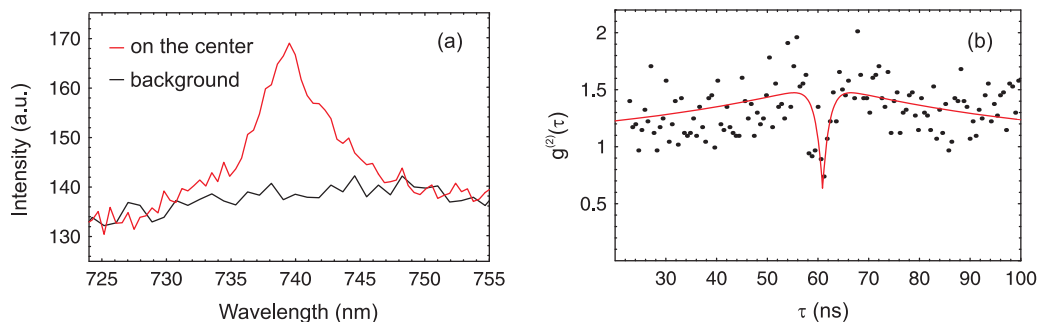
Figure 5.5: (a) Spectrum of the SiV center (red line) and the background (black line) (b) Normalized coincidence rate histogram measured by the HBT setup. The solid line shows the least square fit to the data using a three-level model.

expression

$$g^{(2)}(\tau) = 1 - p_f^2 + p_f^2(1 + c\,\mathrm{e}^{-(\tau-\tau_0)/\tau_1} - (1+c)\,\mathrm{e}^{-(\tau-\tau_0)/\tau_2}). \qquad (5.1)$$

The parameters c, τ_1 and τ_2 are defined in eqns (2.61) - (2.65). The parameter p_f is the probability that a detection event is due to fluorescence of the single SiV center, and τ_0 represents the time delay for the stop signal in the HBT setup (see §4.2). From the least square fit (the red line in figure 5.5(b)) we obtain the values $p_f = 0.62 \pm 0.11$, $c = -2.5 \pm 0.98$, $\tau_1 = 1.34 \pm 0.54$ ns and $\tau_2 = 46 \pm 11.3$ ns. From the 2D scan we calculate the ratio of the fluorescence of the SiV center to total detection events to be about 0.64, which agrees with the value of p_f. Therefore our results are compatible with perfect photon antibunching. The time constants τ_1 and τ_2 are determined with considerably large errors. On the one hand, due to the low fluorescence intensity the statistical errors in the measurement are still significant even after a measurement time of more than four days. On the other hand, the measured value of the short time constant τ_1 is strongly influenced by the time jitter in photon detection as discussed in §4.2, and the long time constant τ_2 is comparable with the range of the whole measurement.

The fit parameters c, τ_1 and τ_2 provide three equations involving the four transition rate coefficients in the three-level model. In order to resolve the value of the coefficients, additional measurements are required. For this purpose the saturation behavior of the fluorescence light and the fluorescence decay lifetime were measured. In figure 5.6(a), the photon count rate on and beside the SiV center is shown as a function of the excitation power. While the background increases linearly with the excitation power (green line), the
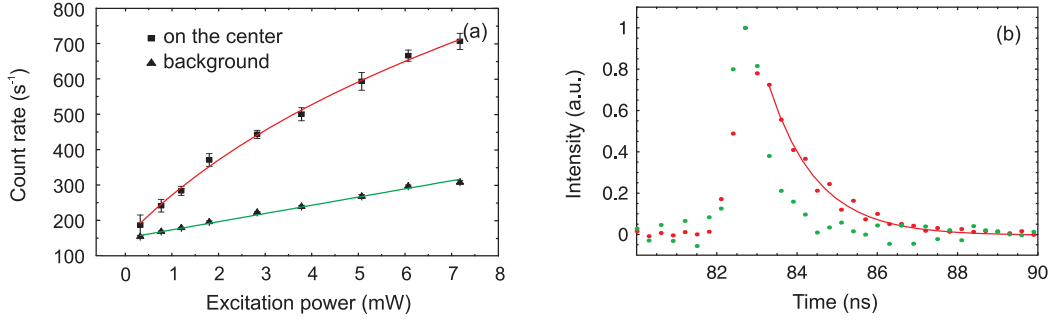
Figure 5.6: (a) Saturation of the fluorescence of the SiV center. The squares represent the count rates measured on the SiV center and triangles that beside it. (b) Fluorescence decay lifetime measurement. The red dots represent the normalized histogram of the time delay between the laser pulse and the fluorescence detection, and the green dots that between the laser pulse and the detection of the laser light reflected by the diamond surface.

dependence of the fluorescence on the excitation power can be well described by the function

$$R(P_e) = \frac{R_0 P_e}{P_e + P_{sat}} \tag{5.2}$$

(red line), which was derived in §2.3 for the three-level model. The saturation power P_{sat} was estimated to be 6.87 ± 0.99 mW. Due to the limited power of the excitation laser diode, the saturation behavior at very strong excitation could not be investigated, which leads to the large uncertainty in the determination of P_{sat}.

To measure the fluorescence decay lifetime, a similar experimental arrangement as in the measurements of the time jitter of our APDs was used. The SiV centers were excited by laser pulses with a duration of 200 ps (FWHM) and a repetition rate of 50 kHz. Histograms of the time delay between laser pulse and fluorescence detection were measured. One histogram is shown in figure 5.6(b), which was measured in a sample with a high concentration of SiV centers for better statistics. By removing the interference filter (IF 740) in front of the APDs, the same measurement was performed for the laser light reflected by the diamond surface. These results are represented by the green dots in figure 5.6(b) for comparison. The fluorescence clearly decays more slowly than the reflected laser light. We assume a simple exponential decay including time jitter in the photon detection. From the least square fit shown in figure 5.6(b) we determined a time constant $\tau_f = 1.20 \pm 0.04$ ns, in good agreement with the values reported in literature [50, 104].

Although the results of the measurement of the second-order correlation function combined with the knowledge of τ_f allow theoretically to resolve all the transition rate coefficients, the large errors in the determination of the fit parameters in $g^{(2)}(\tau)$ make it in practice impossible. Straightforward solution of the set of four simultaneous equations delivers negative values for the coefficients, which is physically meaningless. However, a slight change of τ_1 within the error bars, for example, leads to reasonable results. Therefore the experimental results are not considered to be in conflict with the three-level model. Nevertheless, one coefficient, k_{31}, can be easily determined, as its calculation involves only c, τ_1 and τ_2. For the single SiV center presented here it was found to be 8 ± 2.1 MHz.

The large drawback of single SiV centers for the usage as a single photon source is the low photon emission rate. For an ideal two-level system with a fluorescence decay lifetime of a few nanoseconds, the total photon emission rate at an excitation power comparable to P_{sat} is on the order of 10^8 s^{-1}. Considering the total detection efficiency of the confocal microscope of about 10^{-3}, we expected a photon count rate of 10^5 s^{-1} under the given experimental conditions, which is higher than the observed value by a factor of 200. Non-radiative transitions are one reason for the low photon emission rate. The measured fluorescence decay lifetime is similar to that determined in the measurement of the quantum yield of SiV centers [104], therefore we also assume a quantum yield of 0.05 for the single SiV centers. Another mechanism suppressing the photon emission is probably the existence of a shelving level.

5.3 SiV centers with nitrogen doping

It has been reported that the photoluminescence of SiV centers was much stronger after silicon implantation in synthetic diamonds with a high concentration of isolated nitrogen compared to the diamonds with a low nitrogen concentration. The luminescence of SiV centers was not detectable in natural semiconducting diamond with negligible nitrogen content [96]. This observation is often interpreted as follows: the isolated nitrogen atoms act as donors in diamond and pin the Fermi-level to a position near to the conduction band. The SiV center has a more positively charged state which is not optically active. With higher position of the Fermi-level the fraction of SiV centers in the optically inactive charge state becomes smaller, and consequently the emission of SiV centers increases.

An interesting question is which influence a change of the Fermi-level in the sample has on an individual SiV center. In the previous section we ob-
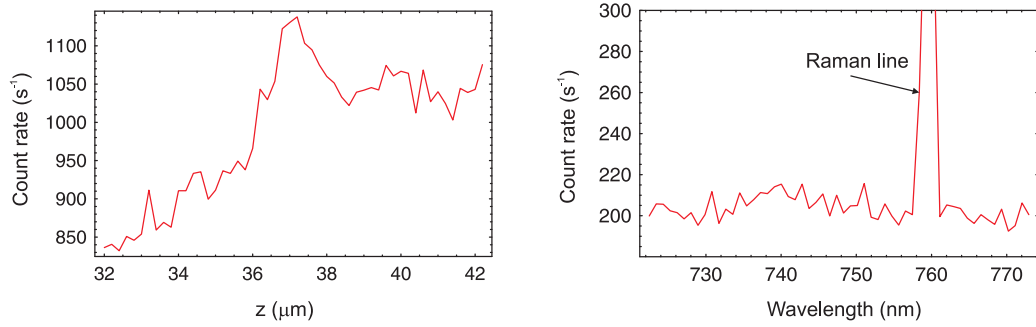
Figure 5.7: (a) Scan along the optical axis across the surface of a IIa diamond sample, which exhibits weak background emission after nitrogen implantation with a dose of 10^{13} cm^{-2} and annealing at 1400 °C for 30 min. The central peak indicates the position of the surface. (b) Spectrum of the background emission.

served a rather low photon emission rate of single SiV centers in IIa diamond samples. An optically inactive charge state can provide a channel for non-radiative transitions or act as a shelving level. Understanding the role of this charge state in the photon emission process of a single SiV center may point out a way to improve the efficiency of SiV center as a single photon source.

5.3.1   Sample preparation

An intuitive approach for the preparation of the samples is silicon ion implantation of Ib diamond which naturally has a high concentration of isolated nitrogen. However, strong background emission was observed on the implanted surface even for very small silicon ion doses [106]. No significant change of the background emission was observed after an additional annealing process at 1400 °C for an hour. Since the strong background made a detection of single SiV centers impossible, ion implantation of Ib diamond samples was not further investigated.

The only effective method to dope diamonds after their synthesis process is ion implantation. Therefore, another way to prepare SiV centers in nitrogen rich environment is to implant both silicon and nitrogen ions into IIa diamond. Figure 5.2 shows that the implanted ions have a quite narrow distribution in the longitudinal direction, therefore it is crucial to choose appropriate ion energies to ensure that both silicon and nitrogen ions are located in the same depth after implantation. SRIM simulations were carried out, showing that an ion energy of 4.4 MeV for silicon ions corresponds to an ion range of 1.41 ± 0.08 μm and 2.9 MeV for nitrogen ions corresponds
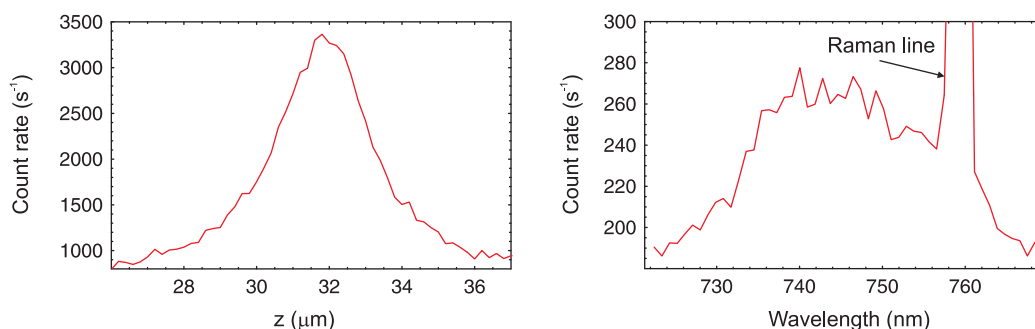
Figure 5.8: (a) Scan along the optical axis across the surface of a IIa diamond sample, which exhibits strong background emission after nitrogen implantation with a dose of 10^{13} cm^{-2} and annealing at 1400 °C for 30 min. (b) Spectrum of the background emission.

to an ion range of 1.43 ± 0.06 μm. The doses of silicon ions were chosen such that single SiV centers can be addressed by the confocal microscope. In contrast, the nitrogen ion doses were much higher to achieve significant effects of doping.

In practice several aspects turned out to be important for the results of the ion implantation. First, the ion sources should have a high purity. Since the nitrogen ion doses were higher than the silicon ion by a factor of 1000, tiny contamination of the nitrogen ion source with silicon can cause a too high concentration of SiV centers. At the beginning, a sputter source of siliciumnitrid was used as source for both silicon and nitrogen ions for simplicity. The implanted samples showed a high concentration of SiV centers independent of the silicon ion dose. After checking every experimental parameter we found out that the contaminated nitrogen source was responsible for these results. Second, compared with the samples with only silicon ion implantation, the conversion rate of silicon impurities to SiV centers is lower after nitrogen doping. It is considered to be due to the competition for vacancies between silicon and nitrogen impurities. Finally, the nitrogen implantation induces a certain degree of background emission around 740 nm whose strength depends on the sample itself. Figure 5.7 and 5.8 show the results of the nitrogen implantation for two IIa diamond samples. Although they were prepared using the identical procedures, they exhibit quite differently strong background emission. Therefore, only samples with low background emission were selected for the investigation of single SiV centers.

Different schemes for the ion implantation were investigated, including silicon implantation – annealing at 1000 °C for 10 min – nitrogen implantation – annealing at 1400 °C for 30 min, nitrogen implantation – annealing at

1400 °C for 30 min – silicon implantation – annealing at 1000 °C for 10 min
and silicon implantation – nitrogen implantation – annealing at 1400 °C for
30 min. No significant differences in the results were observed for the three
schemes. The results presented in this section were measured using two samples. Sample 1 was implanted with 10^{10} cm^{-2} silicon ions and subsequently
with 10^{13} cm^{-2} nitrogen ions. Then it was tempered at 1400 °C for 30 min.
Sample 2 was first tempered at 1000 °C for 10 min after the silicon implantation with a dose of 10^{10} cm^{-2}. Afterwards the nitrogen implantation with
a dose of 10^{13} cm^{-2} and annealing at 1400 °C for 30 min were carried out.

5.3.2 Single SiV centers with different brightnesses

Figure 5.9(a) shows a two-dimensional scan measured on the implanted surface of sample 1. There are four point-like emitters in this scan. Although
they are only separated by about 2 μm, they exhibit different brightnesses.
The count rate at position A is higher than that at position B by a factor of
2.8. Scans along the optical axis were carried out at the positions A, B and
C, and are shown in figure 5.9(b). The position C is considered to be dark
and represents the background emission due to the nitrogen implantation.
The positions of the maxima in those scans agree with each other within the
accuracy of measurement, thus the emitters at position A and B are located
at the same depth as the background emission, which agrees with the SRIM
simulation.

Spectra were measured at position A, B and C as well, and are shown in
figure 5.10. The spectra at A and B are similar except for the strength of the
ZPL of the SiV center. At position C no spectral characteristic of SiV center
emission is visible. The measured $g^{(2)}(\tau)$ of the fluorescence at position A is
shown in figure 5.11. Using the fit function introduced in eqn (5.1) a value
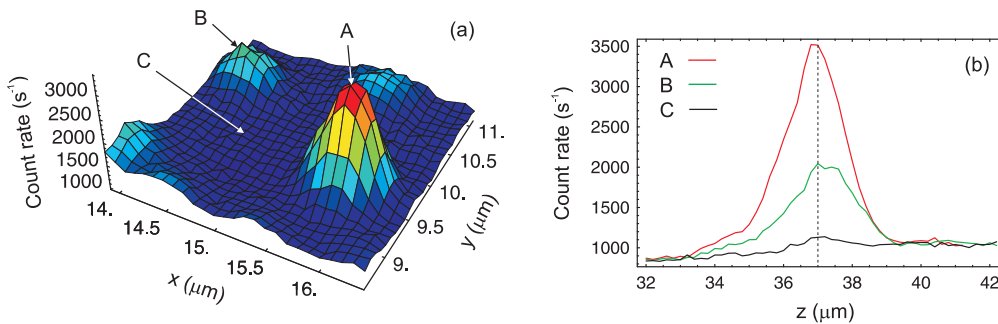
Figure 5.9: (a) 2D scan in the implanted surface of sample 1. (b) Scans along
the optical axis at position A, B and C.
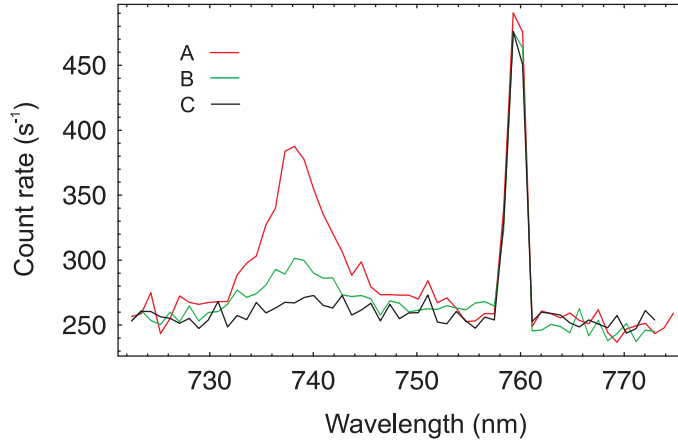
Figure 5.10: Spectra at the position A, B and C.

of 0.64 ± 0.11 was determined for $g^{(2)}(0)$, comparable with the value of 0.59 expected due to the ratio of fluorescence to background. Therefore only a single SiV center but with higher photon emission rate is located at position A. The existence of single SiV centers with significantly different brightness close to each other indicates that the influence of single nitrogen atom on the Fermi-level in diamond is strongly localized. This observation agrees with the predictions of the Fermi-level in diamond by Collins [74].

To understand the origin of the improvement in the photon emission rate of individual SiV centers, careful analysis of the second-order correlation function is required. As a first impression, the effect of correlated emission seems to be reduced for $g^{(2)}(\tau)$ of the bright center compared to the case
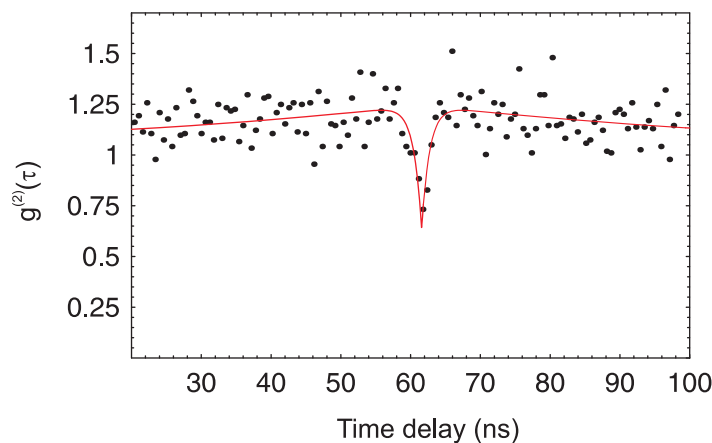
Figure 5.11: Second-order correlation function measured for the fluorescence at position A.

without nitrogen doping shown in figure 5.5(b).

Several bright single SiV centers were also found in sample 2. The background emission due to the nitrogen implantation is stronger in this sample. In figure 5.12 sets of data of two point-like emitters, including 2D scan, spectrum and second-order correlation function, are presented. Their spectra
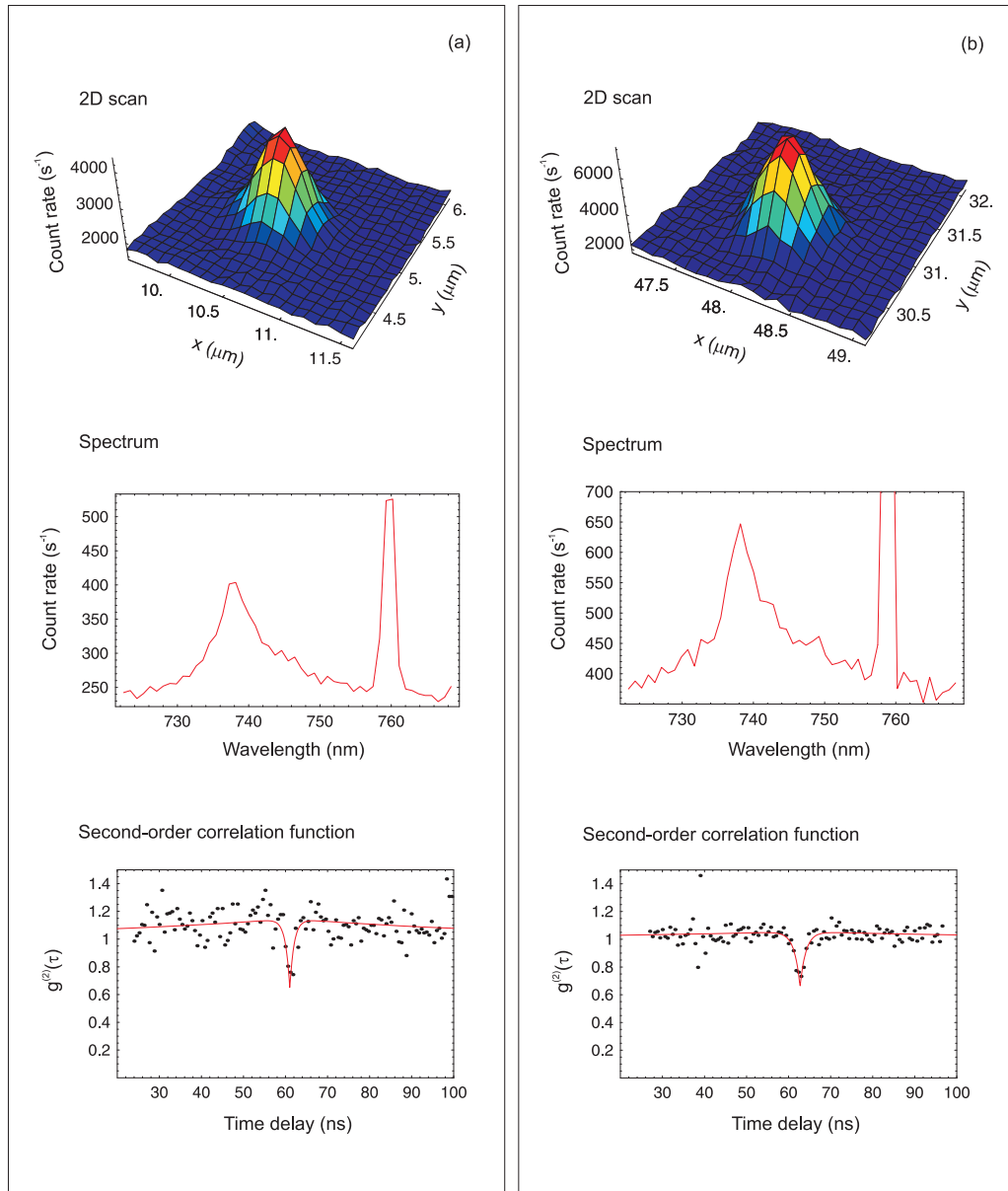
Figure 5.12: 2D scans, spectra and second-order correlation functions of two bright single SiV centers.

show both the ZPL of the SiV center. The value of $g^{(2)}(0)$ proves that they both are single centers. The SiV center presented in figure 5.12(b) is one of the brightest SiV centers ever found. The high photon emission rate allowed a measurement of $g^{(2)}(\tau)$ with small statistical errors, which reveals the impact of experimental conditions on the measured value of $g^{(2)}(0)$. The ratio of fluorescence to background suggests $g^{(2)}(0) = 0.52$, while a value of 0.66 ± 0.05 was determined experimentally. In the case of two identical emitters $g^{(2)}(0) = 0.76$ is expected, therefore the possibility that the point-like emitter consists of two SiV centers at the same position is quite low. As discussed in §4.2, the uncertainty in the determination of the time difference between two detection events in the HBT setup causes a additional value for $g^{(2)}(0)$ which is observed here.

For a clear comparison the brightness and results of the least square fit of $g^{(2)}(\tau)$ of the four single SiV centers which are presented so far are listed in the following table:

count rate (s^{-1})	τ_1 (ns)	τ_2 (ns)	$-c$	k_{31} (MHz)
$600 \pm 32^*$	1.34 ± 0.54	46 ± 11.3	2.5 ± 0.98	8.9 ± 2.1
2212 ± 93	1.14 ± 0.32	62 ± 19	1.68 ± 0.23	9.6 ± 2.98
2514 ± 97	1.01 ± 0.36	61 ± 23	1.41 ± 0.17	11.8 ± 4.5
5118 ± 199	1.37 ± 0.38	66 ± 83	1.16 ± 0.08	12.9 ± 16

*This center is in the sample wihtout nitrogen doping.

These measurements have been performed at comparable experimental conditions. As they were carried out over a time period of more than one year, a slight change in the total photon detection efficiency of the confocal microscope is possible, although the setup was calibrated from time to time using a sample with known concentration of SiV centers. While τ_1 remains unchanged within the error bars, $-c$ decreases with increasing count rate. The time constant τ_2 and consequently the coefficient k_{31} were determined with too large errors, so that no clear trend can be recognized.

Since the condition $\tau_1 \ll \tau_2$ is satisfied for all the SiV centers, it applies that

$$\mathrm{e}^{-\tau/\tau_1} \approx 0 \quad \text{and} \quad \mathrm{e}^{-\tau/\tau_2} \approx 1 \qquad (5.3)$$

for certain times τ which satisfies $\tau_1 \ll \tau \ll \tau_2$. For those τ the second-order correlation function reduces to

$$g^{(2)}(\tau) \approx 1 + c \cdot 0 - (1 + c) \cdot 1 = -c. \qquad (5.4)$$

Therefore $-c$ can be regarded as a measure of the effect of correlated emission. If $-c = 1$, the effect of correlated emission disappears. As discussed in §2.3 higher source efficiency corresponds to a smaller value of k_{23}/k_{31} and a weaker
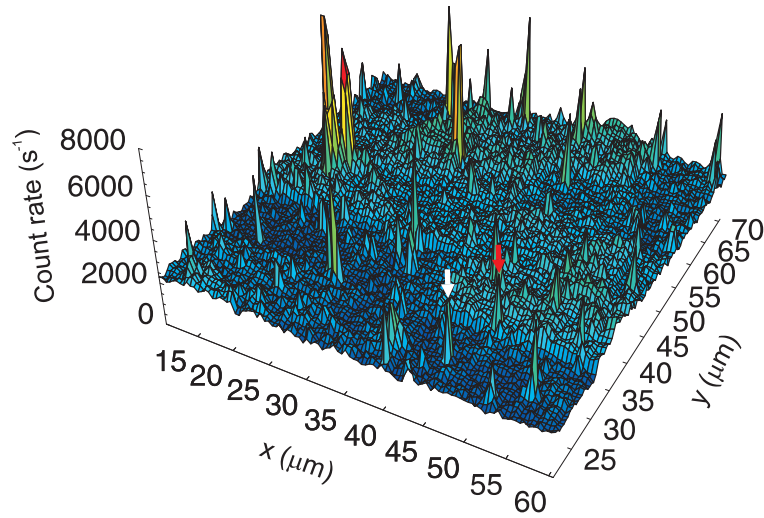
Figure 5.13: A 50x50 μm^2 scan in the implanted surface of the sample 2.

effect of correlated emission. The observed correlation of the photon emission rate of single SiV centers to the value of $-c$ confirms the theoretic predictions. Since k_{31} does not show significant changes, k_{23} must decrease with increasing count rate.

To study the distribution of the brightness of single SiV centers with nitrogen doping, a 50x50 μm^2 area on the implanted surface of sample 2 was thoroughly scanned. This large 2D scan shown in figure 5.13 was made up out of 25 10x10 μm^2 scans. This is necessary, because the sample was not
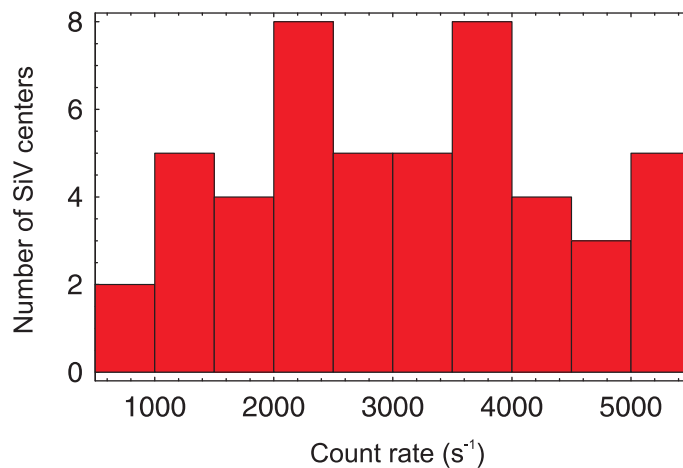
Figure 5.14: Histogram of the brightness of the SiV centers on the large 2D scan.

mounted exactly perpendicularly to the optical axis. A large scan in x- and y-direction causes the focus of the confocal microscope to leave the surface, and consequently the plane where the SiV centers are located. The large scan shows that the background emission is not homogeneous over the sample. The sharp peaks correspond mainly to point-like emitters. For example, the single SiV center presented in figure 5.12(b) is located at the position marked by a red arrow. There are also regions with very strong fluorescence which probably originates from dirt on the surface. The fluorescence intensity in these regions usually decays on a time scale of seconds. Each point-like emitter on the scan was investigated carefully by measuring its brightness and spectrum. The spectra of these emitters exhibit a surprising diversity. Details about the different single color centers with ZPL in the spectral range around 740 nm are presented in the next chapter. Only the fluorescence with a spectrum exhibiting a ZPL with a maximum at 738.2 ± 0.4 nm and a FWHM of 6 ± 1 nm are considered to be emitted by SiV centers.

A histogram of the brightness of the SiV centers is shown in figure 5.14. The brightest single SiV centers have a brightness about eight fold higher than that of the darkest, which exhibit a photon count rate similar to that of the SiV centers found in samples without nitrogen doping of about 600 s^{-1}. The possibility of finding a single SiV center with intermediate brightness is higher than that of finding the brightest or the darkest ones. This observation indicates the statistical nature of the influence of nitrogen atoms on a single SiV center. However, the histogram should be interpreted with caution. The diffraction-limited size of the fluorescence image does not guarantee that only one single SiV center was observed. Figure 5.15 shows a 2D scan at the position marked by a white arrow on the large scan shown in
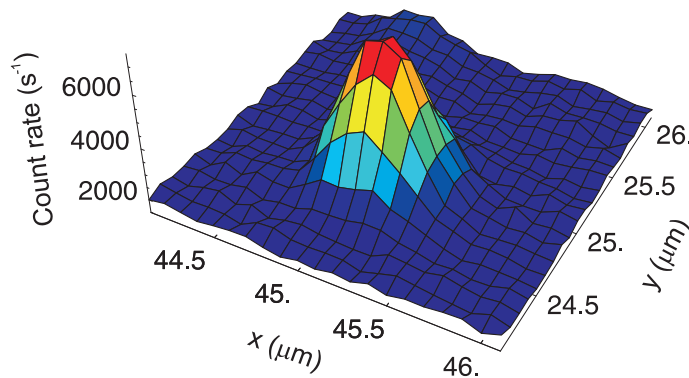
Figure 5.15: 2D scan at the position marked by a white arrow of the large scan in figure 5.13.
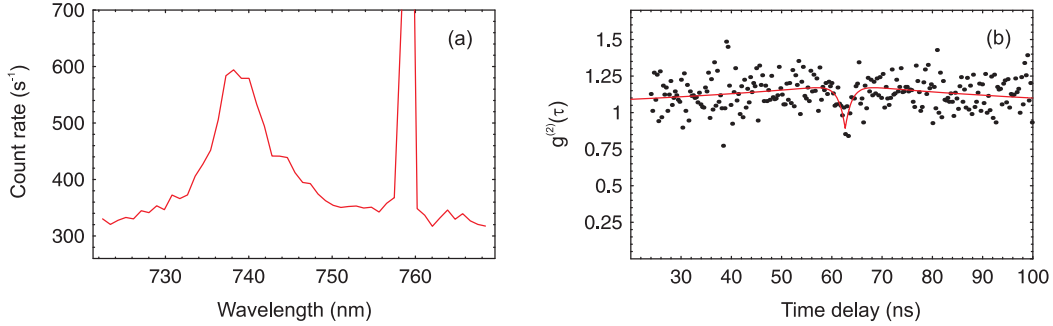
Figure 5.16: (a) Spectrum of the point-like emitter shown in figure 5.15. (b) Second-order correlation function of the corresponding fluorescence light.

figure 5.13. There is no difference to the fluorescence image of a single SiV center. The spectra presented in figure 5.16(a) shows that it is fluorescence originating from the SiV center, but the second-order correlation function in figure 5.16(b) exhibits only a weak photon antibunching effect. A value of 0.83 ± 0.7 was determined for $g^{(2)}(0)$, although 0.5 was expected for a single center. Therefore there are probably two SiV centers very close to each other. Thus, this observation is not presented in the histogram. Although due to the long measurement time $g^{(2)}(\tau)$ was only measured for some of the brightest SiV centers, the SiV centers contributing to the histogram are considered to be primarily single ones. The diffraction limited resolution of the confocal microscope is about 600 nm. If two SiV centers are separated by a distance lager than 200 nm, the fluorescence image of them deviates clearly from a perfect circle as expected for a single center. From the large 2D scan the average distance between two SiV centers is estimated to be about 7 μm. The possibility to find two SiV centers located so closely that they appear to be a point-like emitter is therefore quite small.

5.3.3   Conclusions

Summarizing we see that the SiV center has a ground state energy at $E_c -$ 2.05 eV, which results in an excited state close to the conduction band, making photothermal ionization possible. If the SiV center loses an electron, it becomes positively charged and consequently incapable of photon emission. Therefore, the positively charged state can be regarded as the shelving level in the three-level model. The transition from the excited to the positively charged state is governed by the Fermi-Dirac-statistics. For a low position of the Fermi-level the positively charged state is more strongly occupied, which is equivalent to a large value of k_{23}/k_{31} in the three-level model. This

is the case for the samples without nitrogen doping. The nitrogen atoms locally raise the Fermi-level in the diamond sample. How strongly a single SiV center is influenced by the change of Fermi-level depends on its distance to the nitrogen atoms in its vicinity. A high position of the Fermi-level reduces the population of the positively charged state, which is reflected in the decreasing value of k_{23}/k_{31}. Consequently, the effect of correlated emission is reduced and the brightness of the SiV centers increases. The parameter $-c$ of the second-order correlation function of the brightest SiV centers approaches unity, which suggests that these centers behave nearly as an ideal two-level system. In the previous section we estimated that the shelving level will reduce the photon emission rate by a factor of 10. This is in good agreement with the observed maximal improvement of fluorescence intensity of single SiV centers due to nitrogen doping. The parameter τ_1 is almost independent of the brightness, from which we can conclude that the fast fluorescence decay is not influenced by the change of Fermi-level. Therefore, the non-radiative transitions from the excited to the ground state do not involve the positively charged states.

5.4 Collection efficiency of the fluorescence light

Diamond has the highest refractive index among the transparent materials, which prevents an efficient collection of the fluorescence light of an emitter located in diamond. Besides employing optical resonators to avoid emission in 4π, there are two methods to overcome this obstacle: using solid immersion lens (SIL) to achieve a high numeric aperture [108] and reducing the sample size well below the fluorescence light wavelength to avoid refraction [109]. In this section we report on the results of applying the two methods on single SiV centers.

5.4.1 Solid immersion lens

Solid immersion microscopy, a technique similar to oil immersion microscopy, extends the diffraction limit by filling the object space with a high-refractive-index material. Since its introduction in 1990 [108], it has found applications in data storage [110], lithography [111], and the study of semiconductor nanostructures [112]. Two types of SILs are used. One is a simple hemisphere [108] and the other is a standard Weierstrass optic in which the height of the truncated sphere is equal to $(1 + 1/n)r$, where n is the refractive index of the

material and r the radius of curvature. Theoretically, imaging can be performed near the center of the bottom of SILs without geometric aberration [108].

Originally, SIL-microscopy was developed as a technique to enhance the spatial resolution of conventional microscopy, since the FWHM of a diffraction-limited spot scales like the factor $1/NA$ [113], where NA is the numeric aperture of microscope objective. In the case of the collection efficiency of fluorescence light, improving the NA leads to a larger solid angle Ω of the fluorescence collection. As the fluorescence light is assumed to be emitted equally in all spatial directions, Ω is equal to the ratio between the collected and total fluorescence light and can be expressed in term of NA as

$$\Omega = \frac{\int_0^{2\pi}(\int_0^{arcsin\text{NA}} sin\theta \mathrm{d}\theta)\mathrm{d}\phi}{\int_0^{2\pi}(\int_0^{\pi} sin\theta \mathrm{d}\theta)\mathrm{d}\phi} = \frac{1 - cos(arcsin\text{NA})}{2}. \qquad (5.5)$$

In our experiment a half-ball diamond lens with a diameter of 0.9 mm purchased from Element Six was used as a SIL. The half-ball lens was set onto a IIa diamond sample which had been implanted only with silicon ions with an energy of 4.4 MeV and a dose of 10^9 cm^{-2}. Figure 5.17 shows the procedure of mounting the SIL on the sample. To ensure the function of the SIL, the thickness of the air gap between sample and half-ball lens should be significantly below the wavelength of the fluorescence light. Therefore
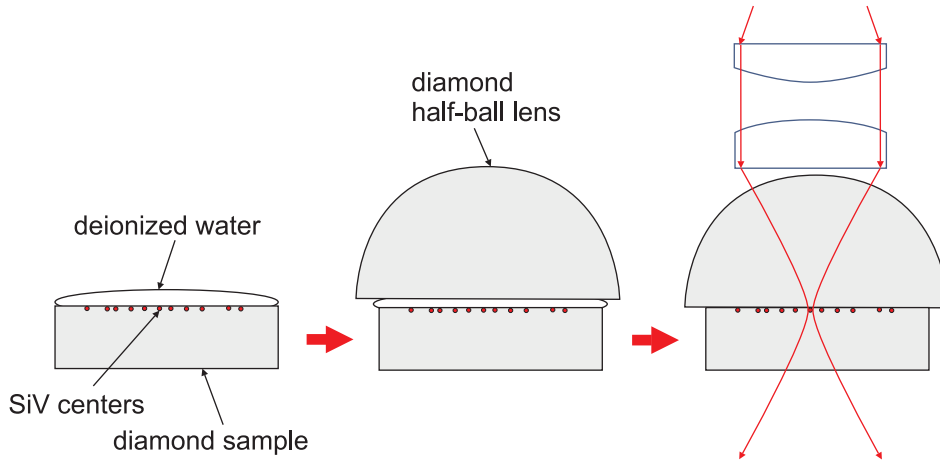
Figure 5.17: Working procedure of setting the half-ball lens on the sample. The surface of the diamond sample is moistened by deionized water before the SIL is set onto it. After evaporation of the water the SIL is held on the sample by Van-der-Waals forces.
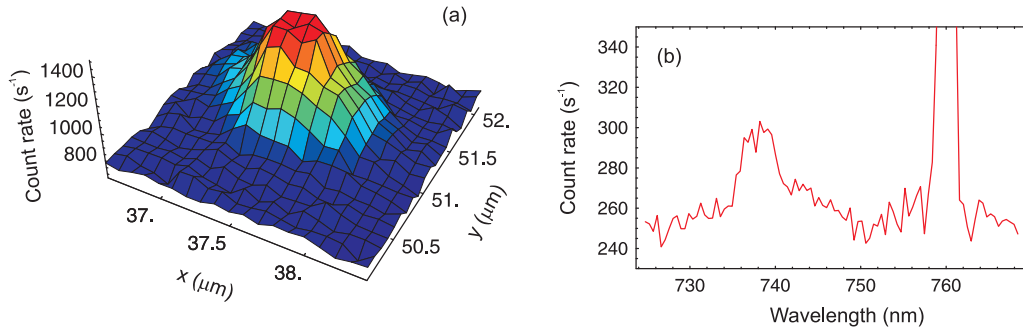
Figure 5.18: (a) 2D scan of a dark SiV center found with SIL. (b) Spectrum of the fluorescence light.

considerable efforts have been made to avoid dirt on the surfaces. The sample surface with SiV centers was first polished using polishing powder to remove adhesive dirt and then cleaned in an ultra-sonic bath with distilled water, acetone and isopropanol. In a clean room a drop of deionized water was put onto the sample surface, whereupon the half-ball lens was placed on the sample. After 5 minutes the deionized water evaporates completely. The sample and half-ball lens are pressed by the atmospheric pressure so close to each other that the lens is held on the sample by Van-der-Waals forces. Finally the sample with the half-ball lens was mounted into the confocal microscope for further investigation.

For comparison, the sample was first thoroughly investigated without the SIL. Six 10x10 μm^2 scans ware made at different positions on the implanted surface. Altogether, 13 point-like emitters with a spectrum of the SiV center were found. The brightness of the emitters was found to be identical. A photon count rate of about 600 s^{-1} was registered at an excitation power of 8.2 mW for each of them. Since the sample had been implanted by an ion beam with a diameter significantly larger than the size of the sample, the concentration of SiV centers is assumed to be homogeneous over the sample. The average distance between the SiV centers is so large that the possibility of finding two SiV centers separated by a distance well below the wavelength is negligible. Therefore the found point-like emitters are considered to be single SiV centers and the concentration of them was determined to be 0.02 μm^{-2}.

With the half-ball lens on the sample, an area of 40x40 μm^2 at the center of the bottom of the lens was scanned. Only 10 SiV centers were found, which corresponds to a clearly lower concentration of SiV centers than observed in the same sample without SIL. Additionally, the SiV centers exhibit different brightnesses. A dark SiV center is shown in figure 5.18, while figure 5.19
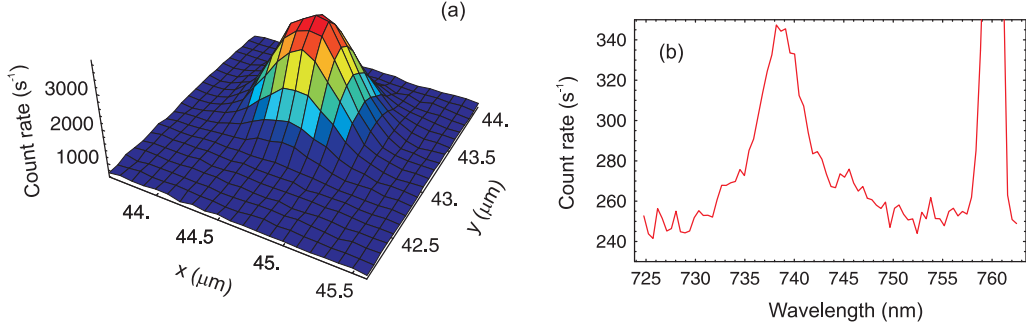
Figure 5.19: (a) 2D scan of one of the brightest SiV centers found with SIL. (b) Spectrum of the fluorescence light.

presents the brightest SiV center observed in this scan. The brightest SiV center was investigated in detail. The fluorescence intensity profile of this center along the x-direction is shown in in figure 5.20(a). The FWHM was determined to be 686 ± 13 nm. The saturation behavior of this center was analyzed and the results are presented in figure 5.20(b). We obtained a saturation power of 7.63 ± 0.66 mW.

The second-order correlation function of the fluorescence light was also measured, and is shown in figure 5.21. Since the improvement of the photon count rate is not accompanied by increasing background emission as for the bright SiV centers with nitrogen doping, the photon antibunching effect in $g^{(2)}(\tau)$ is much more pronounced and thus verifies unambiguously the single photon characteristics. The parameters of the least square fit were determined as $c = -3.1 \pm 0.57$, $\tau_1 = 1.34 \pm 0.18$ ns and $\tau_2 = 43.6 \pm 2.9$ ns.

The observed size of the diffraction-limited fluorescence image of the sin-
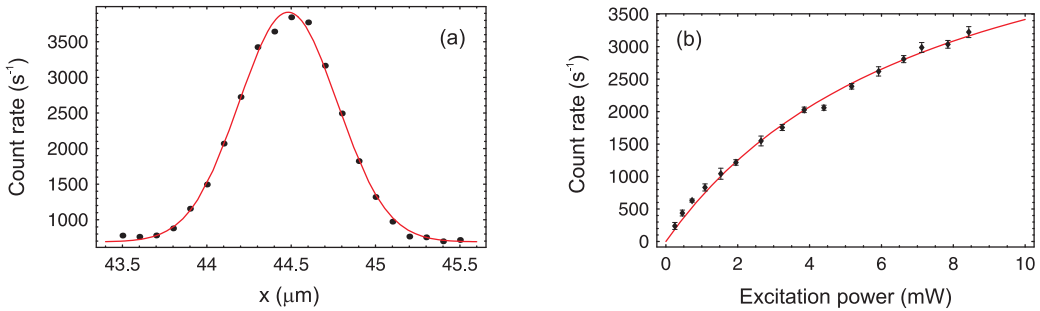
Figure 5.20: (a) Fluorescence intensity profile of the bright SiV center along the x-direction. (b) Fluorescence saturation behavior of the bright SiV center.
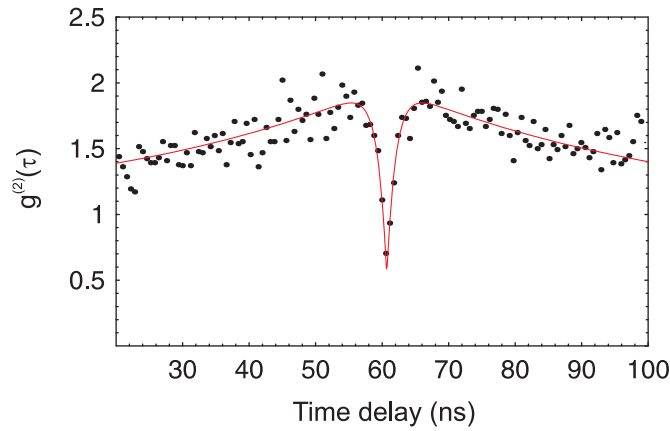
Figure 5.21: Second order correlation function of the fluorescence light of the bright SiV center shown in figure 5.19.

gle SiV center is comparable with that without SIL, although theoretically a smaller FWHM by a factor of the refraction index of diamond $n_{diam} = 2.41$ is expected. The reason for this observation is that in the confocal microscope the SIL was moved with the sample during the scanning process. Figure 5.22 shows this situation. O denotes the center of the half-ball lens. If the lens is moved from the optical axis by a small displacement $\overline{OF'}$, the real position of the focus is at F instead of F' as expected for the case without lens. Because the displacement is significantly smaller than the radius of the half-ball, the relation $\overline{AF'} \approx \overline{AF} \approx \overline{AO}$ applies. For small angles α and α' shown in the
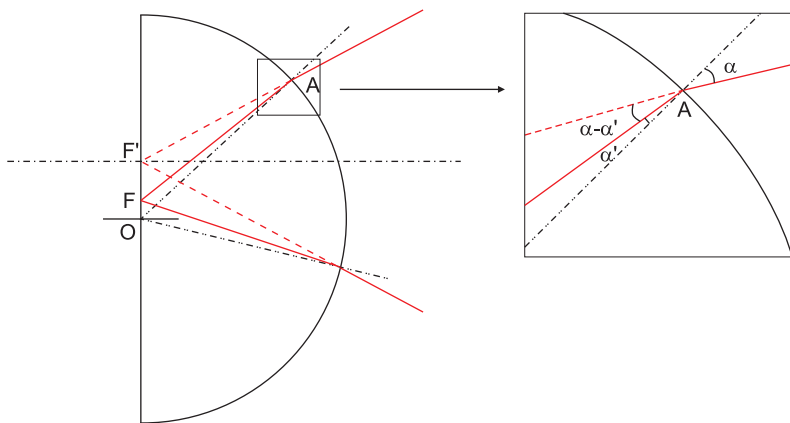
Figure 5.22: A schematic representation of the influence of the half-ball lens on the optical path during the scanning.

inset of figure 5.22, the ratio between $\overline{F'F}$ and $\overline{FO}$ is expressed as

$$\frac{\overline{F'F}}{\overline{FO}} = \frac{sin(\alpha - \alpha')}{sin\alpha'}. \tag{5.6}$$

On the other hand the relation between α and α' is determined by the Snell's law as

$$\frac{sin\alpha}{sin\alpha'} = n_{diam}. \tag{5.7}$$

Using the approximation for small angles $sin\alpha \approx \alpha$ the relation between displacement of the sample $\overline{OF'}$ and the displacement of the focus $\overline{OF}$ is found to be

$$\frac{\overline{OF'}}{\overline{OF}} \approx n_{diam}. \tag{5.8}$$

Thus the real displacement of the focus during the scanning is scaled by a factor of $1/n_{diam}$. This effect compensates exactly the enhancement of the optical resolution due to the SIL. Therefore the size of the fluorescence image of a single SiV center remains unchanged, although we have in fact a smaller focus. This explains also the apparently lower concentration of SiV centers observed with the half-ball lens on the sample, since the actually scanned area is smaller.

The measurement of the saturation behavior reveals a saturation power which is comparable to that measured without SIL for the single SiV centers. This indicates that the relation between the excitation power and the pump rate coefficient is similar for both cases, therefore the improvement of the photon count rate at the same excitation power is considered primarily due to the larger collection solid angle. According to eqn (5.5) an improvement of the collection efficiency of a factor of 6.82 is predicted. Experimentally, a maximal enhancement of a factor of about 5 was observed, which approaches the ideal case quite well. The fit parameters of $g^{(2)}(\tau)$ agree excellently with those determined in §5.2. Therefore we can conclude that there is no change in the emission properties of the single SiV center and the higher photon count rate is only due to the enhancement of the collection efficiency of the fluorescence light.

However, the improvement is not uniform for all SiV centers. Since the surfaces are not exactly flat, the surface roughness may lead to a variation of the width of the air gap between the sample and the SIL. If the width of the air gap is comparable to the wavelength at some places, the brightness of the SiV centers there appears weaker.
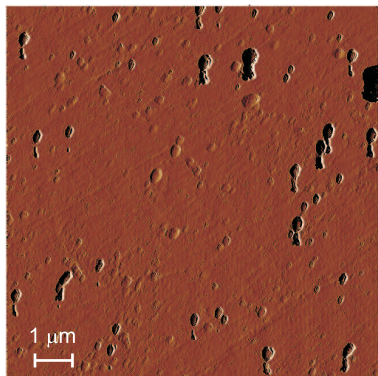
Figure 5.23: A picture of the sample with CVD diamond nanocrystals recored by an AFM.

5.4.2 SiV centers in diamond nanocrystals

Another possibility to improve the collection efficiency of the fluorescence is to avoid the refraction. If color centers are contained in diamond nanocrystals, the subwavelength size of the nanocrystals renders refraction irrelevant. Thus those color centers can be considered as light sources emitting in air. However, the improvement of the collection solid angle is accompanied by a reduction of the radiative transition rate from the excited to the ground state. This effect is caused by the change of the refractive index of the surrounding medium from bulk diamond to air. In a simple approach the radiative lifetime of an optical dipole is expressed as

$$\tau_n = n\tau_v, \tag{5.9}$$

where τ_v is the radiative lifetime in vacuum and τ_n is that in the material with a refractive index of n [109].

The investigated nanocrystals were grown on a fused silica substrate using the CVD method by James Rabeau of the University of Melbourne, Australia. A picture of the sample recorded by atomic force microscopy is presented in figure 5.23. The lateral size of the diamond nanocrystals varies from 100 nm to 1000 nm, and height from 10 nm to 120 nm.

Although in bulk CVD diamond the concentration of SiV centers had been found to be so high that the optical addressing of single centers is impossible, it is reasonable to assume that the CVD diamond nanocrystals may contain single SiV centers, as the size of those nanocrystals is significantly smaller than the diffraction-limited spot of the confocal microscope. Figure 5.24(a) shows a 20x20 μm^2 scan on the sample. Strong and localized fluorescence
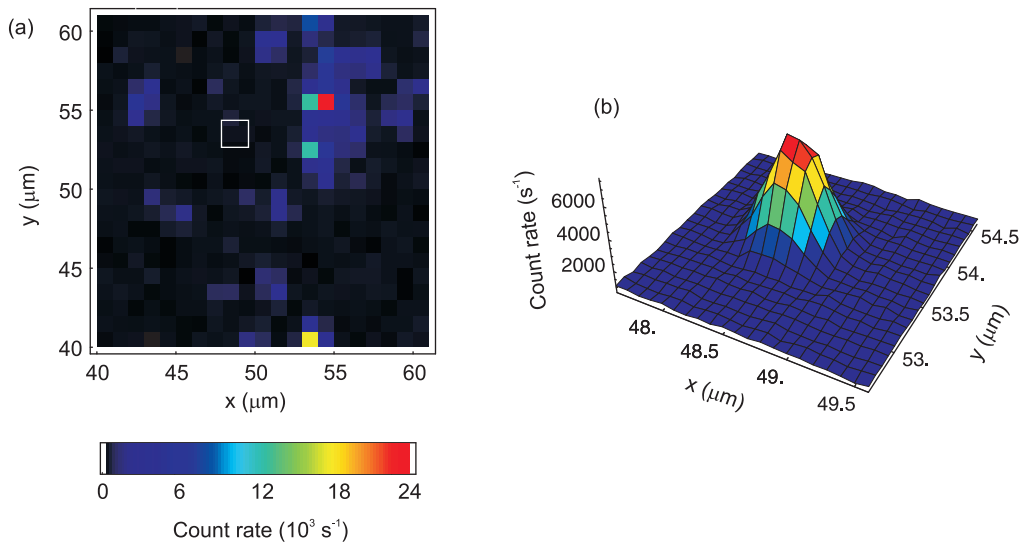
Figure 5.24: (a) 2D scan over an area of 10x10 μm^2 on the sample with diamond nanocrystal. (b) A point-like emitter found at the position marked by the white square in (a).

from SiV centers was observed, which corresponds to the large crystals with a high content of SiV centers. In a dark region which is marked by the white square on this scan a point-like emitter was found as presented in figure 5.24(b).

The spectrum of this point-like emitter is presented in figure 5.25 and the ZPL of the SiV center is clearly visible. The Raman spectrum of diamond disappears due to the small size of the crystal. Despite the high brightness of this emitter, the second-order correlation function shown in figure 5.26 ex-
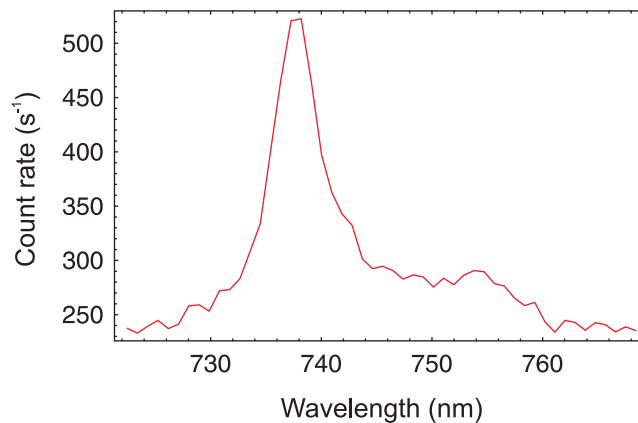
Figure 5.25: Spectrum of the fluorescence light of the point-like emitter presented in figure 5.24
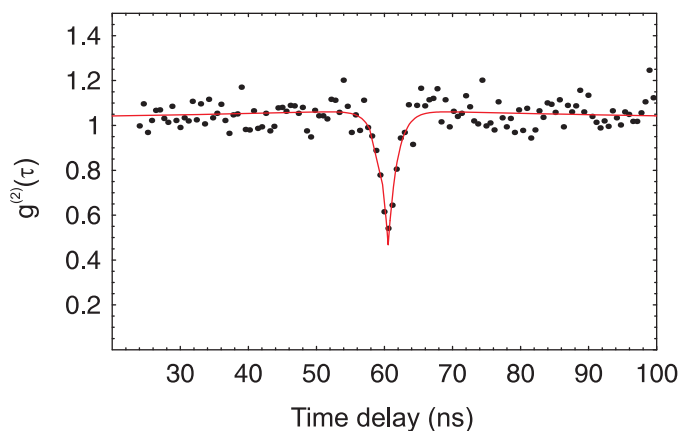
Figure 5.26: Second-order correlation function of the fluorescence light of a single SiV center in a CVD diamond nanocrystal.

hibits a strong photon antibunching effect, which indicates that the presence of only a single SiV center in the nanocrystal. Differently from the bright single SiV centers observed with SIL, almost no effect of correlated emission effect is present in $g^{(2)}(\tau)$, which suggests a high position of the Fermi-level in the diamond nanocrystals. The fit parameters were determined as follows: $c = -1.13 \pm 0.03$, $\tau_1 = 1.35 \pm 0.21$ ns and $\tau_2 = 84.1 \pm 55$ ns.

Compared with the single SiV centers in undoped bulk samples with the same excitation power, the photon count rate of this SiV center is higher by a factor of 11, although according to eqns (5.5) and (5.9) only an improvement of 2.8 is expected due to the small size of the nanocrystal. On the other hand, the second-order correlation function reveals a change in the emission characteristics of the SiV center. The results of the least square fit of $g^{(2)}(\tau)$ are similar to those of the brightest SiV center in the samples with nitrogen doping. Thus the Fermi-level in the nanocrystal is probably close to the conduction band so that the possibility to populate the positively charged state is negligible. This is possible since nitrogen is a dominant impurity in CVD diamond, and the size of the nanocrystals ensures a short distance between SiV centers and nitrogen impurities. Another important information contained in the second-order correlation function is that the short time constant τ_1 remains unchanged in nanocrystals. τ_1 is considered to be primarily determined by the transition rate from the excited to the ground state. According to eqn (5.9) the radiative lifetime should be enlarged by n_{diam} in nanocrystals. This observation confirms that the transition from the excited to the ground state of the SiV center is dominated by non-radiative channels.

Chapter 6

Other color centers

There is a surprising variety of color center species in diamond. Due to the low quantum yield at room temperature, the SiV center is not ideal for single photon generation in any practical applications. Therefore, the possibility of using other color centers was explored. For this purpose photoluminescence investigations of xenon and nickel implanted diamond samples have been carried out.

Furthermore, series of single color centers were observed in IIa diamond during the extensive scanning, although due to the limitation of the setup only the fluorescence in the spectral range from 730 nm to 760 nm is visible. Because of their low concentration such color centers are hidden in macroscopical luminescence investigation of diamond, therefore no report of them can be found in literature. The determination of the origin of those color centers is beyond the scope of this thesis. Here, we merely document the observed single color centers.

6.1 Xenon implantation

Xenon ion implantation has been widely used to study ion-beam-induced transformation of isolating diamond to a conductive form of carbon [114, 115]. Photonluminescence spectra of xenon implanted natural Ia diamond exhibit a single ZPL at 811.6 nm at a temperature of 8 K. With increasing temperature a second ZPL at 793.3 nm appears and grows, while the ZPL at 811.6 nm becomes less intense. This behavior indicates that these two ZPLs originate from two sub-levels of the same excited state. A spectrum of the Xe-related center at 200 K is presented in figure 6.1. The Huang-Rhys factor was determined to be $S = 0.69 \pm 0.14$, which reflects a moderately low electron-phonon coupling [116]. Thus the Xe-related center could be
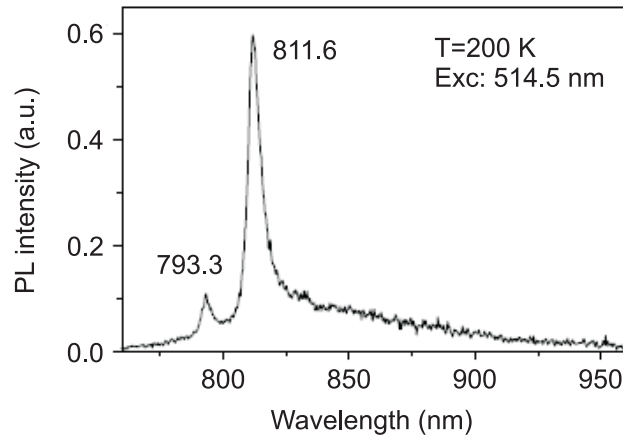
Figure 6.1: Spectrum of the Xe-related center at 200 K [116].

interesting for single photon generation.

The investigated samples were two natural IIa diamonds implanted by 2 MeV Xe ions at room temperature with a dose of 10^{13} cm^{-2} (sample Xe1) and 10^{11} cm^{-2} (sample Xe2). Post-implantation annealing was carried out at 1400 °C in vacuum for 1 hour. For the photoluminescence investigation the confocal microscope was modified. Basically the dichroic mirror DICH690 was replaced and an interference filter IF810 was inserted in front of the APDs. The transmission curves of the dichroic mirror and IF810 are shown in figure 6.2. For the excitation, the 690 nm laser diode was used.

A scan along the optical axis of the implanted surface of the sample Xe1 was recorded and is shown in figure 6.3(a). The sharp peak corresponds to
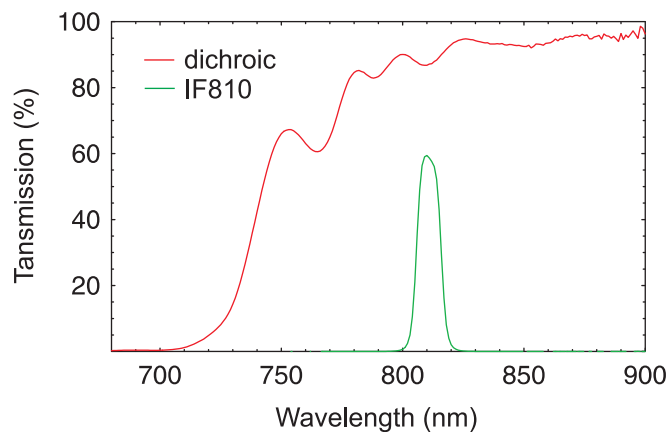
Figure 6.2: Transmission of the dichroic mirror (red line) and the interference filter IF810 (green line) used for analysis of the Xe-related center.
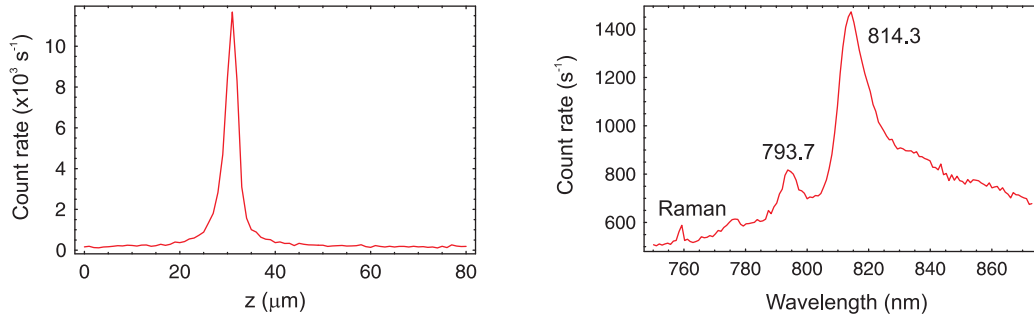
Figure 6.3: (a) Scan along the optical axis on the implanted surface of the sample Xe1. (b) Spectrum of the fluorescence.

very intense fluorescence from the diamond surface. In order to avoid saturation of the APDs, a neutral density filter with a transmission of 0.04 was set into the optical path to attenuate the fluorescence light. The spectrum of the fluorescence is shown in figure 6.3(b). The characteristic two ZPLs of the Xe-related center are clearly visible. While the ZPL with higher energy is found at 793.7 nm, which agrees well with the value in [116], the ZPL at 814.3 nm shows slight deviation from the literature value. Homogeneous distribution of the fluorescence light intensity was found on the surface, which indicates a high concentration of the Xe-related centers.

The intensity of the fluorescence light from the implanted surface of the sample Xe2 is much lower. Figure 6.4(a) shows a longitudinal scan of the surface recorded without the neutral density filter. The background emission from the diamond sample is not negligible compared to the peak which corresponds to the fluorescence of the Xe-related centers. The spectra of the
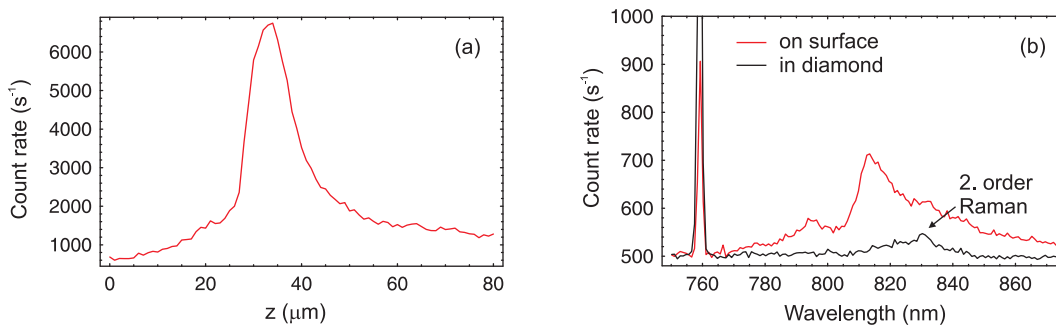

Figure 6.4: (a) Scan along the optical axis on the implanted surface of the sample Xe2. (b) Spectrum of the fluorescence (red line) and background emission of the diamond sample (blackline).
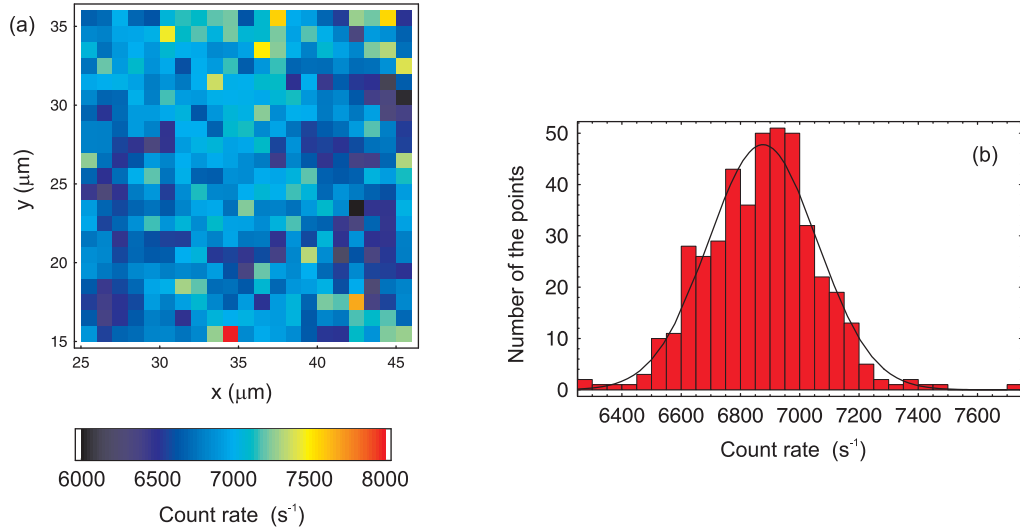
Figure 6.5: (a) 2D scan on the implanted surface of the sample Xe2, recorded with a integration time of 3 s for each point. (b) Histogram of the photon count rate for the area shown in (a).

fluorescence and the background emission are shown in 6.4(b). The background emission originates primarily from the second-order Raman scattering of the diamond lattice which is much broader than the first-order Raman line [117]. In order to compare the concentration of the Xe-related centers in the two samples, the intensities of the ZPL at 814.3 nm in the spectra were normalized by the first-order Raman line. We found out that the sample Xe1 has a higher concentration of Xe-related centers than the sample Xe2 by a factor of 21.

The results presented above demostrate the fabrication of Xe-related centers by ion implantation, although the concentration of Xe-related centers is too high to detect single ones. Before preparing samples with lower xenon ion dose, it is reasonable to consider the photon emission rate expected for a single Xe-related center. The answer to this question requires a quantitative estimation of the concentration of the Xe-related centers in the samples. The experimental measurable value is the photoluminescence intensity instead of the concentration of the color centers in the sample. As the ion range in the direction of the optical axis is significantly smaller than the optical resolution, the spatial concentration of the Xe-related centers is equivalent to their areal density on the surface which is proportional to the photon count rate recorded by the confocal microscope. On the other hand, according to the conditions of the ion implantation we assume a homogeneous distri-

bution for the xenon ions in the sample and consequently for the created Xe-related centers. Thus, the concentration of Xe-related centers exhibits a spatial fluctuation of $\sqrt{\bar{\rho}}$, where $\bar{\rho}$ is the average concentration. Therefore, we can determine the average concentration of Xe-related centers by measuring the spatial fluctuation of their fluorescence intensity over the implanted diamond surface.

Figure 6.5(a) shows a 2D scan over a 20x20 μm^2 of the implanted surface of the sample Xe2 recorded at the maximal excitation power. During scanning several sources of the photon count rate fluctuation were considered, including statistical errors in the photon counting, the stability of the excitation power and the position of the surface, and their contributions were found to be negligible. A histogram of the photon count rate for this area was measured and is presented in figure 6.5(b). The solid line in figure 6.5(b) is a least square fit using a Gaussian function. The fit function suggests an average value of $\bar{c} = 6876 \pm 7.2$ s^{-1} and a standard deviation of $\Delta c = 184 \pm 7.2$ s^{-1} for the photon count rate. The longitudinal scan shown in figure 6.4(a) which was recorded at the same excitation power suggests a background count rate of $b = 1500 \pm 50$ s^{-1}, including emission from the diamond and dark counts of the APDs. From these data an average number of Xe-related centers within the focus of the confocal microscope was estimated as

$$\left(\frac{\bar{c} - b}{\Delta c} \right)^2 = 851 \pm 34. \tag{6.1}$$

The focus has a FWHM of about 0.7 μm and the areal density of the xenon atoms is 1000 μm^{-2}. Therefore, the possibility that a xenon atom forms a Xe-related center is nearly unity. The average photon count rate of a single Xe-related center was determined to be about 7 s^{-1}.

Several reasons are responsible for this extremely low value. First of all, only a part of the fluorescence light was detected due to the interference filter IF810. Secondly, the excitation might not reach the saturation power. Finally, the focus of the confocal microscope has a Gaussian profile. If a single Xe-center is located at the middle of the focus, it will exhibit higher photon emission rate. Nevertheless, the Xe-related center is not an efficient source for single photon generation. Therefore, no further investigation of this color center was carried out.

6.2   Nickel implantation

Nickel impurities are often present in HPHT (High Pressure High Temperature) diamond, since nickel is usually used as catalyst for diamond synthesis.
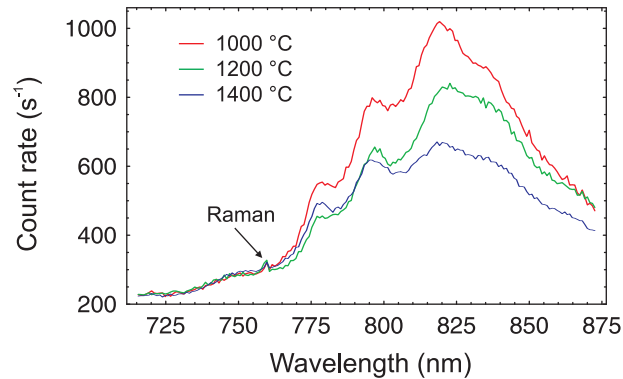
Figure 6.6: Spectra of the nickel implanted Ia diamond samples and annealed at different temperature.

For many years, the only experimental evidence of the presence of the heavy metal element in diamond was the ESR (Electron Spin Resonance) spectrum of nickel which originates from the hyperfine structure of ^{61}Ni [118]. Nickel exists not only as single disperse atoms in diamond. It can also form a variety of complexes with nitrogen atoms at high annealing temperatures. The nickel-nitrogen defects with different configurations were identified by ESR experiments and labeled as NE1-NE5. Nadolinny et al. reported on a new line in the ESR spectra of ^{13}C enriched diamond and denoted it as NE8. The structure of the NE8 center is considered to consist of one nickel atom surrounded by four nitrogen atoms. Photoluminescence investigations of the samples revealed a ZPL at 793.6 nm which is stable up to 2300 K just like the ESR line of NE8, thus this ZPL was ascribed to the optical transition of NE8 [119]. The Huang-Rhys factor of the 793.6 nm center is determined as $S = 3.5$ [120, p. 149].

Recently the observation of single color centers with sharp ZPLs around 800 nm has been reported by several groups. Gaebel *et al.* reported on a color center in untreated natural IIa diamond. It has a sharp ZPL at 802 nm and a luminescence lifetime of 11.5 ns [26]. Wu *et al.* found also another color center in natural IIa diamond with a ZPL at 782 nm and a luminescence lifetime of about 2.1 ns [29]. Rabeau *et al.* presented a color center incorporated in CVD diamond nanocrystals. The ZPL of that center is at 797.6 nm and the Huang-Ryhs factor is determined to be $S = 0.35$ [27]. Although the color centers have different optical properties, they are claimed to be the NE8 center. As there are many unknown color centers present in diamond in vanishing concentration (see §6.3), those reported single color centers might also have different origins.

To prove the possibility to fabricate the nickel-nitrogen center in bulk
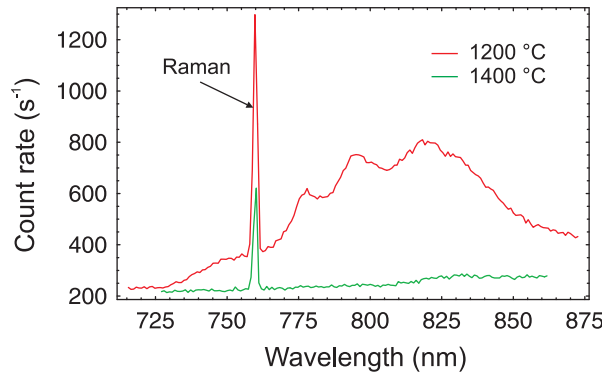
Figure 6.7: Spectra of the nickel implanted IIa diamond samples and annealed at different temperature.

diamond sample, nickel ion implantation of diamond was carried out. As host materials both Ia and IIa diamonds were chosen. Ia diamond contains nitrogen impurities in aggregate form which could be advantageous for the formation of nickel-nitrogen centers. Three Ia diamond samples were implanted by 2 MeV nickel ions with a dose of 10^{13} cm^{-2}. Post-implantation was carried out in vacuum for half an hour at 1000 °C, 1200 °C and 1400 °C, respectively. Two IIa diamond samples were implanted at similar conditions, and annealed at 1200 °C and 1400 °C.

The photoluminescence spectra of the implanted surface of the Ia diamond samples are shown in figure 6.6. The fluorescence light probably originates from the neutral vacancies produced by ion implantation. The neutral vacancy is responsible for the GR1 band with a ZPL at 740 nm. At room temperature the ZPL is weak compared with the vibronic sidebands, and it is as well suppressed by the dichroic mirror in the confocal microscope. Therefore, it is not visible in the spectrum. The intensity of the GR1 band, normalized by the Raman line, decreases with increasing annealing temperature.

The photoluminescence spectra recorded from IIa diamond samples are presented in figure 6.7. The sample annealed at 1200 °C exhibits the same spectrum as the Ia diamonds, although with much lower intensity, while the GR1 band almost completely disappears in the sample annealed at 1400 °C.

Generally, the dependence of the results of the annealing process on the temperature can be understood by analyzing the mobility of vacancies. The vacancies in IIa diamond seem to have a higher mobility than in Ia diamond, because the IIa diamond samples show a lower intensity of the GR1 band than the Ia diamond samples after same implantation and annealing process. The reason of the different mobility of vacancies in the two types of diamond

is unknown. It might depend on the content of impurities in the samples. No sharp ZPL around 800 nm was observed in both Ia and IIa diamond, although the concentration of nickel impurities in the implanted region is considerably high. This indicates that due to the complex structure the NE8 center is much more difficult to be created than the SiV or the Xe-related center. The nitrogen atoms in diamond start to diffuse at much higher temperature than vacancies. The formation of the NE8 center in synthetic diamonds with high content of nitrogen and nickel can only be observed after heating above 1600 °C [120, p. 149]. This might explain the failure of out attempts. Since the higher annealing temperatures are associated with considerable technical complexity, no further work has been done to fabricate the nickel-nitrogen center in this work.

6.3   Unknown single color centers

During the investigation of SiV centers the diamond samples were extensively scanned. A variety of single color centers were observed. The spectra of some color centers are so similar to that of the SiV center that they were mistaken for SiV centers. Since the concentration of those color centers is negligible for conventional methods used for investigating the color center, almost no report on them is present in literature up to now. The origin of those centers could not be determined in the scope of this thesis, although some of those color centers exhibit advantageous properties for single photon generation.

6.3.1   A blinking center

Figure 6.8(a) shows the fluorescence image of an intense point-like emitter in a IIa diamond sample. Its spectrum exhibits a sharp peak at 736.8 nm with a FWHM of about 1.3 nm. No vibronic sidebands are visible in the spectrum. Unlike the other single color centers observed during this thesis the fluorescence of this center exhibits fluctuations at a time scale of a few seconds. The fluorescence intensity of this center was registered at different excitation powers, and each trace was recorded for 2000 seconds. The parts of two traces recorded at 0.83 mW and 3.04 mW respectively are presented in figure 6.9. At constant excitation power the photon count rate switches between a certain value and the dark count of the APDs, as if the emitter would be turned on and off incessantly. This behavior can be explained by transitions between two internal states of this center, labeled as on- and off-state. In the on-state this center is able to emit photons and in the off-state not.
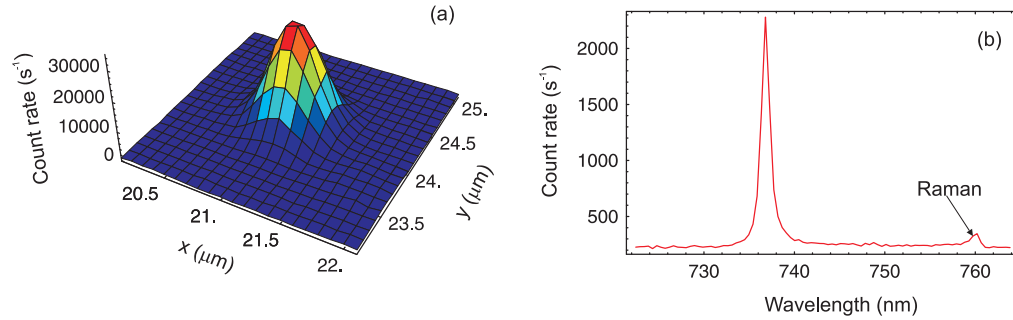
Figure 6.8: (a) 2D scan of an intense point-like emitter in a IIa diamond sample. (b) Spectrum of the fluorescence.

Comparing the two traces in figure 6.9, it is obvious that the switching of the fluorescence intensity becomes faster at higher excitation power. In order to investigate the dependence of the transition rate on the excitation power, histograms of the length of the on- and off-periods were calculated for the traces recorded at different excitation powers. The two histograms for the red trace in figure 6.9 are presented in figure 6.10(a) and (b). The distributions of the length of the on- and off-periods can both be well described by an exponential function as shown by the solid lines in the histograms. For the transition from the on- to the off-state a time constant of 7.32 ± 0.42 s was determined, while for the transition from the off- to the on-state a time constant of 1.9 ± 0.14 s is measured.

The transition rates as a function of the excitation power are shown in figure 6.11(a) and (b). The transition rate from the on- to the off-state
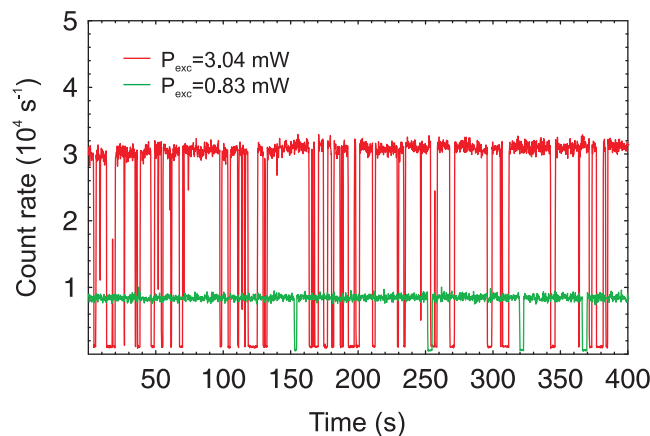

Figure 6.9: Fluorescence intensity fluctuation of the blinking center at different excitation powers.
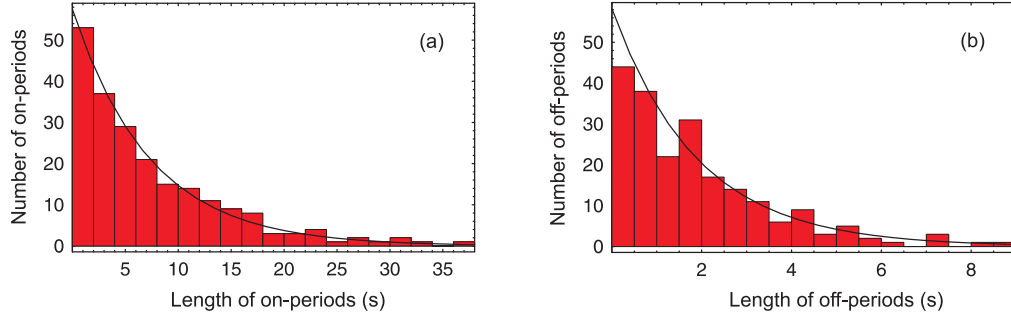
Figure 6.10: (a) Histogram of the length of the on-periods at the excitation power of 3.04 mW. (b) Histogram of the length of the off-periods in the same measurement.

converges to zero at low excitation power. As shown in figure 6.11(a) the data is well described by a quadratic fit function which indicates that two-photon absorption is involved in this transition. The rate of the transition from the off- to the on-state approaches a non-vanishing value at low excitation power, which indicates that this transition can take place without involving photons. Thus the on-state is considered to have lower energy and in the absence of excitation the system relaxes to the on-state. At strong excitation the rate of the transition from the off- to the on-state seems depend on the excitation power. However, due to the limited excitation power this dependence could not be further explored.

In figure 6.12 the photon count rates in the on-periods are presented in dependence of the excitation power. Using the fit function in eqn (5.2) a saturation power of 7.43 ± 1.15 mW was determined. Compared with
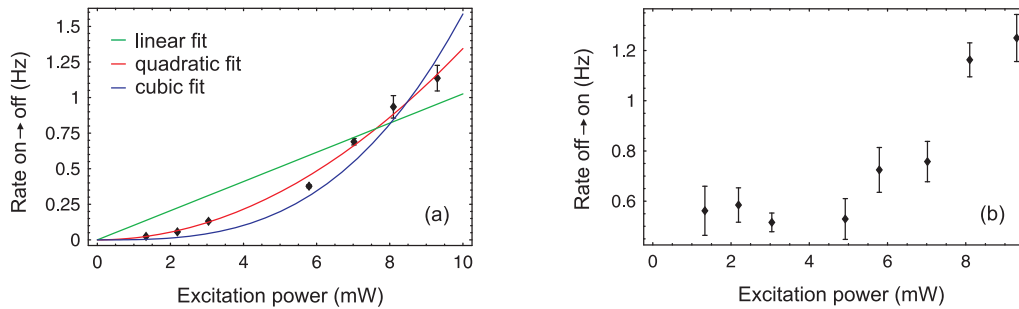

Figure 6.11: (a) Transition rate from the on- to the off-state at different excitation powers. The solid lines represent the least square fits using different functions. (b) Transition rates from the off- to the on-state at different excitation powers.
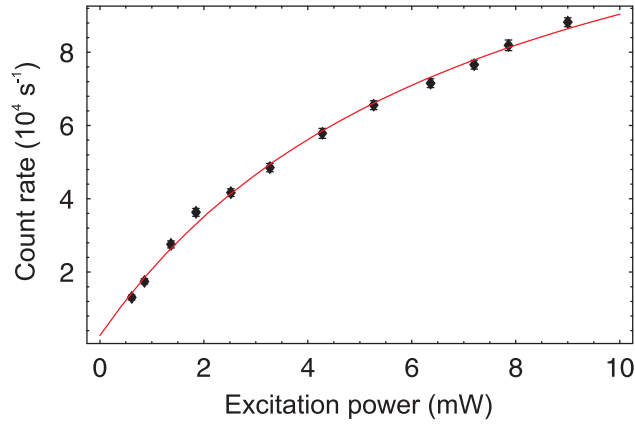
Figure 6.12: Saturation behavior of the blinking center.

the single SiV centers in IIa diamond sample without nitrogen doping, the brightness of this centers at the saturation power is higher by a factor of about 140.

Finally the second-order correlation function of the fluorescence light was measured and is shown in figure 6.13. The pronounced photon antibunching clearly verifies that this is a single center. Although the background detection events are negligible compared with the intense fluorescence, $g^{(2)}(0)$ has still a residual value due to the limited time resolution of the photon detection. For large τ, $g^{(2)}(\tau)$ exceeds clearly unity which reflects the intensity fluctuation shown in figure 6.9.

If the off-state is considered as a shelving level, this center can also be modeled by the three-level system introduced in §2.3. For this center it
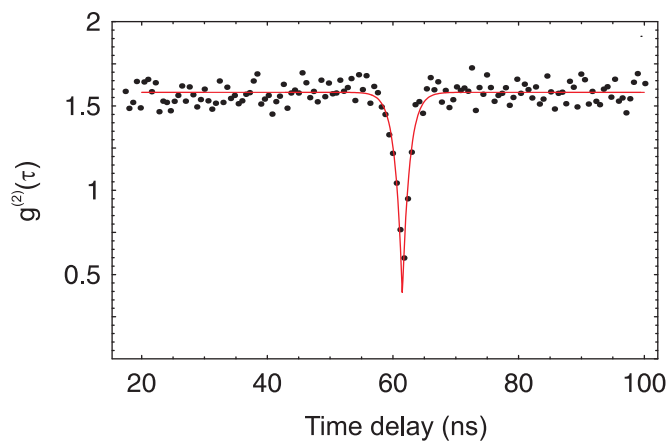

Figure 6.13: Second-order correlation function of the fluorescence light from the blinking center.

applies that $k_{23}, k_{31} \ll k_{21}, k_{12}$. As a consequence, the short time constant τ_1 of $g^{(2)}(\tau)$ expressed in eqn (2.62) is reduced to

$$\tau_1 \approx \frac{1}{k_{12} + k_{21}}. \tag{6.2}$$

The values of $1/\tau_1$ determined at different excitation power are shown in figure 6.14. As suggested by eqn (6.2), $1/\tau_1$ is equal to k_{21}, the reciprocal luminescence lifetime of this center, at zero excitation power. Extrapolating the linear fit to zero excitation power leads to $k_{21} = 395 \pm 14$ MHz which corresponds to a luminescence lifetime of 2.53 ± 0.09 ns.

One possible interpretation of the on- and off-state could be two different charge states of the center. By a two-photon absorption the center is ionized and transfered into a more positively charged state in which it is not able to emit photons. The non-fluorescent charge state has a higher energy and the center tends to get an electron and relax to the energetically favored on-state. This interpretation fits quite well to properties of the SiV center. Additionally, this blinking center was found near the implanted surface of a nitrogen doped sample. Therefore it was incorrectly regarded as a SiV center exchanging an electron with a nitrogen atom in its neighborhood. However the differences of the spectrum and luminescence lifetime suggest that this center has rather a different origin.

This blinking center has been investigated continuously for two weeks and no change of the emission characteristics was observed. However, during one measurement it turned out and could not be found again.
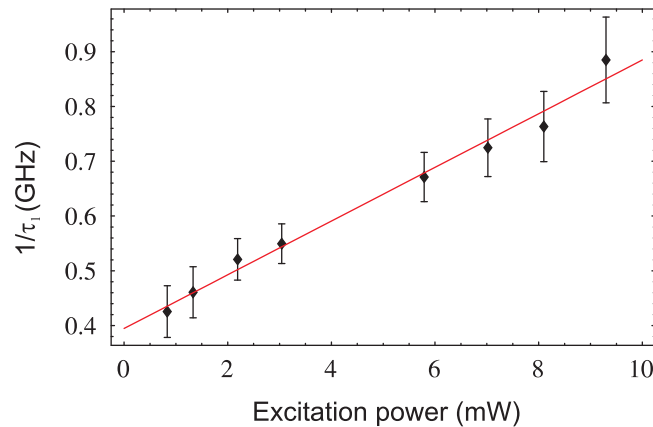

Figure 6.14: Evolution of $1/\tau_1$ as a function of excitation power together with a linear fit (red line).

6.3.2 A 737.3 nm center

In the IIa diamond sample with nitrogen doping another intense color center was observed near the implanted surface. It is named as 737.3 nm center due to the spectral position of its ZPL.

The fluorescence image of a 737.3 nm center is shown in figure 6.15(a). At the same excitation power, the brightness of this center is higher than that of a single SiV center in undoped IIa diamond by a factor of about 35. Unlike the blinking center the fluorescence of this center exhibits constant intensity. The scans along the optical axes on and aside this center are presented in figure 6.15(b). The maximum of the scan recorded nest to this center indicates the position of the implanted ions (see §5.3). Figure 6.15(b) shows that this center lies about 1 μm away from the implanted ions. Since the straggling of the ion ranges was determined by SRIM as 74 nm, this center probably does not originate from the implantation process.

The spectrum of this center is shown in figure 6.16(a) and consists of a ZPL at 737.3 nm with a FWHM of 5 nm and negligible sidebands. The spectrum exhibits such an amazing similarity to that of the SiV center that this center had been regarded as SiV center. The spectrum of the SiV center measured in a sample with high concentration of SiV centers is also presented in figure 6.16(a). Compared with the spectrum of the SiV center the ZPL of this center is slightly blue shifted and has a narrower line width.

Figure 6.16(b) shows the second-order correlation function of the fluorescence. Using the least square fit, the two time constants of $g^{(2)}(\tau)$ were determined as $\tau_1 = 0.66 \pm 0.06$ ns and $\tau_2 = 8.6 \pm 0.23$ ns, respectively. Due to the short τ_1 the impact of the errors in the time difference measurement on $g^{(2)}(0)$ becomes much stronger, which results in the large value of $g^{(2)}(0)$. Nevertheless, the dip in $g^{(2)}(\tau)$ shows unambiguously that it is a single cen-
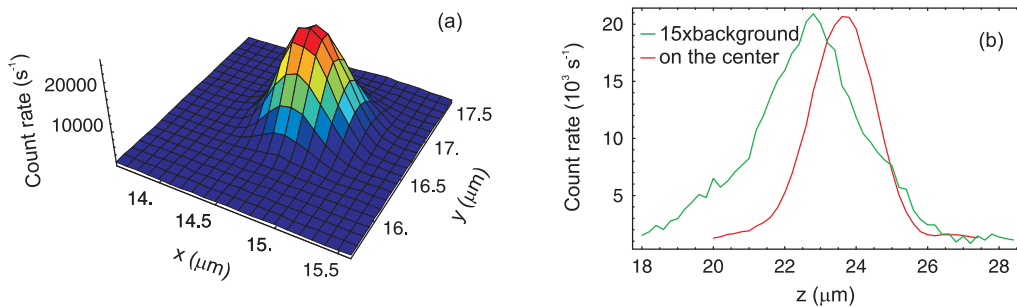

Figure 6.15: (a) Fluorescence image of a 737.3 nm center. (b) Scans along the optical axes on and aside the center. The green curve is multiplied by a factor 15 for better comparison.
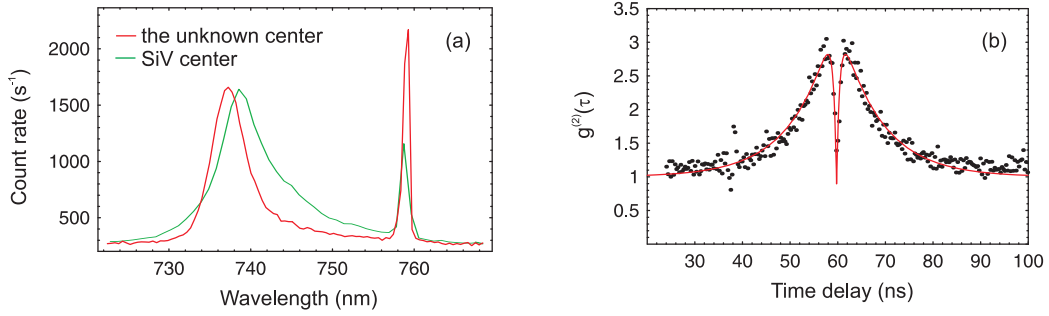
Figure 6.16: (a) Spectrum of the 737.3 nm center (red) and the SiV center (green). (b) Second-order correlation function of the fluorescence light from the 737.3 nm center.

ter. More remarkable is the effect of correlated emission, which indicates the existence of a shelving level. Compared with the $g^{(2)}(\tau)$ of SiV centers, the τ_2 is short as well, which suggests fast transitions between the shelving level and the excitation-and-decay cycle.

The attempt to explain the observations in frame of the three-level model for the SiV center failed. At the same excitation power higher photon emission rate is accompanied by a stronger effect of correlated emission, which is contradictory to the theoretic predictions. When more centers with the same properties were found deep in the sample, it became clear that the implanted silicon ions are not involved in the formation of this center and its higher brightness and stronger effect of correlated emission are not due to the nitrogen doping. The 737.3 nm center probably has a different origin as the SiV center despite the similar spectrum. In the investigated IIa diamond sample, the average distance between two 737.3 nm centers was found to be about 60 μm.

6.3.3 Different single centers

The two single color centers presented above (the blinking and 737.3 nm center) were investigated in detail, since they both exhibit some similarities with the SiV center. More different single color centers were also observed in IIa diamond samples. Here only the spectra and the second-order correlation functions of the fluorescence light from these centers are presented.

Figure 6.17(a) shows the spectrum of a single center whose brightness is higher than that of a single SiV center in undoped IIa diamond by a factor of 22. The left part of the spectrum matches the transmission curve of the dichroic mirror, therefore the part of the spectrum with shorter wavelengths
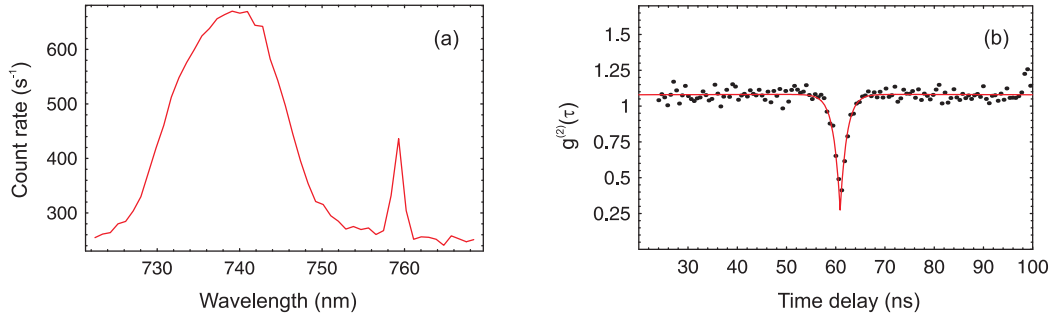
Figure 6.17: (a) Spectrum of a single color center. (b) Second-order correlation function of the fluorescence light from this center.

is cut off and the ZPL can not be observed. Therefore, it can not be identified. Since the excitation laser has a wavelength of 690 nm, the ZPL is probably located between 690 nm and 730 nm.

The second-order correlation function shown in figure 6.17(b) suggests that this center can be well described by a single two-level system, since the effect of correlated emission is negligible. From a least square fit of $g^{(2)}(\tau)$ we obtained $\tau_1 = 1.32$ ns, which is comparable with the SiV center. The much stronger emission is probably due to a higher quantum yield.

The fluorescence of another single color center exhibits a similar second-order correlation function (see figure 6.18(b)), but a completely different spectrum (see figure 6.18(a)). The ZPL of this center is located at 740 nm just like the GR1 emission band of a neutral vacancy. However, the GR1 emission has much stronger sidebands at room temperature. The brightness of this center is 13 folds of that of a single SiV center in undoped IIa diamond.

The spectrum in figure 6.19(a) consists of only a sharp ZPL line at 741 nm. The fluorescence also originates from a single center as demonstrated
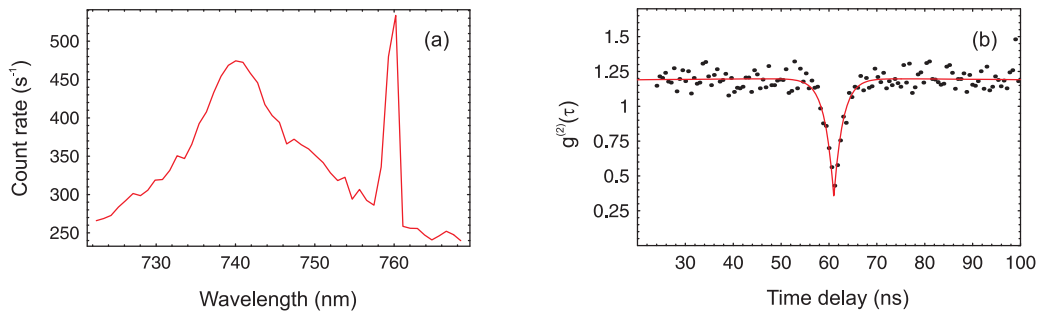

Figure 6.18: (a) Spectrum of a single color center. (b) Second-order correlation function of the fluorescence light from this center.
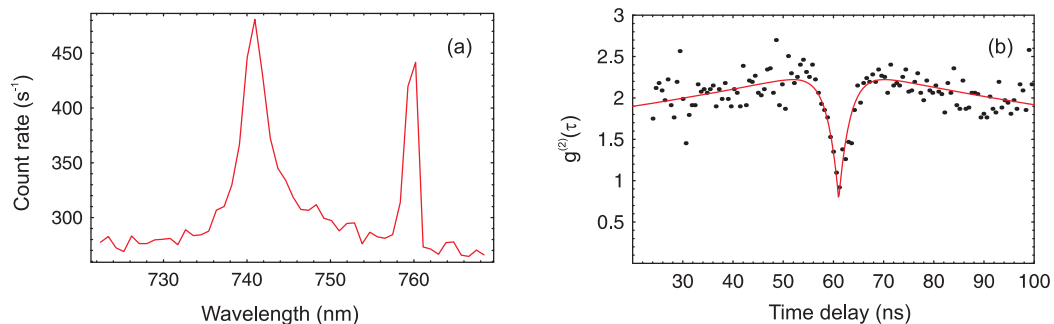
Figure 6.19: (a) Spectrum of a single color center. (b) Second-order correlation function of the fluorescence light from this center.

by the second-order correlation function in figure 6.19(b). This center has obviously a shelving level. It has been reported that the cathodoluminescence of a Cr-related center shows a ZPL at 741 nm [120, pp. 157-159]. However, the CL spectra of the Cr-related center also exhibits a line at 754 nm due to a quasilocal vibration mode which is not to see in this spectrum. Therefore, this center is probably not the Cr-related center.

The single color centers documented in this section might not be good candidates for a single photon source, as long as little is known about their identity and the way to fabricate them deterministically. In any case, they demonstrate the impressing variety of the color centers in diamond and may motivate the further search for the "perfect" color center.

Chapter 7

Summary and outlook

In this work the prospects of building a simple and reliable solid state single photon source based on the color centers in diamond were analyzed. For this purpose different aspects were examined. First of all, optical spectroscopy of single color centers, primarily the SiV center, was carried out. Secondly, the fabrication methods of color centers were explored. Finally, the possibilities of enhancing the collection efficiency of the fluorescence light emitted by single color centers were investigated.

The SiV center was considered to have several advantageous properties for single photon generation, e.g. the narrow spectrum and short luminescence lifetime. However, the rather low brightness of the single SiV centers found in bulk IIa diamond revealed a poor quantum yield. Additionally, the second-order correlation function of the fluorescence light indicates the existence of a shelving level, which further reduces the photon emission rate at a given excitation.

In nitrogen-doped samples single SiV centers with different brightnesses were observed. The brightness of individual SiV centers was found to be related to the effect of correlated emission which is visible in the $g^{(2)}(\tau)$. This phenomenon can be explained by the inhomogeneous Fermi-level induced by the nitrogen doping. If a single SiV center is located at a position with high Fermi-level, the coupling to the shelving level is reduced resulting in a weaker effect of correlated emission. Consequently the brightness of the SiV center is enhanced. From this we conclude that the shelving level should correspond to the positively charged state of the SiV center, which exhibits no fluorescence. With proper control of the Fermi-level the population of the positively charged state can be neglected and the SiV centers act as ideal two-level systems.

Besides the SiV center, several unknown single color centers with remarkable properties were observed during this thesis. Since they appear in

diamond only in a vanishing concentration, no reports on them can be found in literature. Nevertheless, they demonstrate the impressing variety of the color centers in diamond and might give motivation for the search for a color center more suitable for single photon generation.

The ability to create color centers in a controllable manner is essential for practical applications. Recently, fabrication of color centers has attracted great interest [121, 27, 28, 122]. Therefore methods for the fabrication of single color centers were also developed in this thesis. Ion implantation is an efficient way to create color centers in bulk samples. It allows a precise control of the localization and concentration of the created color centers. However, only the color centers consisting of an impurity atom and vacancies can be easily created. In contrast, color centers with a more complicated structure can be formed during the CVD process [27]. Diamond nanocrystals grown by the CVD method were found to contain single color centers. Modification of the Fermi-level is feasible for the both methods.

In order to improve the collection efficiency of the fluorescence light, which is another important issue for practical applications, two methods have been investigated. On the one hand, a diamond solid immersion lens has been used to increase the solid angle of the fluorescence light collection. Due to the surface roughness an a air gap exists between the SIL and sample, therefore the enhancement of the photon collection efficiency is not uniform for individual SiV centers. The highest improvement of the fluorescence light collection of a single SiV center was found to be a factor of 5 compared to the case without SIL, which agrees with the theoretical predictions quite well. On the other hand, the small size of diamond nanocrystals promises to remove the refraction which prevents an efficient collection of the fluorescence light. The most intense SiV center observed in this thesis, with an enhancement of a factor of 11 compared to the SiV centers in undoped IIa diamond samples, was found in a diamond nanocrystal. The high brightness is due to the enhanced photon collection efficiency combined with the high Fermi-level in the CVD diamond.

The SiV center exhibits a poor quantum yield at room temperature due to the dominant non-radiative transitions between the excited and the ground state, therefore it is not ideal for a simple single photon source. Nevertheless, the investigation of the single SiV centers might help to understand the internal structure. Although the origin of the non-radiative transitions is still unknown, it was shown that they can be frozen out at low temperature [103]. Therefore it is advisable to carry out the further investigations of the SiV center at low temperatures.

Strong control of the interaction between color centers and photons is desirable for using color centers in quantum information processing. It can be

realized by coupling a single color center to an optical cavity. There are two different approaches. On the one hand, color centers with suitable properties can be created by ion implantation in an optical cavity made of diamond. Recently it has been shown that diamond based photonic crystal microcavities might be feasible despite the relatively small refractive index [123]. For this purpose holes with a diameter below 100 nm and a depth of about 500 nm must be fabricated in diamond. The realization of such structures is a very challenging task due to the extreme hardness of diamond. Available methods of micromachining of single crystalline diamond includes ion-beam-assisted lift-off technique [77] and anisotropic plasma etching [124]. The other possibility is to deposit diamond nanocrystals containing color centers in a given optical cavity. Strong coupling between NV centers in diamond nanocrystals and the whispering gallery modes in a silica microsphere has been observed [125]. In this approach the addressing of single individual color centers is however a highly non-trivial issue.

Diamond nanocrystals also open up new opportunities to manipulate color centers. Considering a $p - i - n$ semiconductor structure with the diamond nanocrystals embedded in the i-layer, the charge state of the color centers in the diamond nanocrystals might be controlled by the applied voltage in analogy to quantum dots [126]. If the mean free path length of the electrons in the i-layer is long enough so that they can gain sufficient kinetic energy, electronic excitation of single color centers could be feasible according to the principle of cathodoluminescence. This could result in a much more compact single photon source.

In many aspects color centers in diamond provide easy to handle quantum systems which are not only desirable for single photon generation. For practical applications in quantum information processing more knowledge about the color centers is required. This work may hopefully contribute to a better understanding of the properties of the color centers and how to fabricate and manipulate them.

Bibliography

[1] C. Bennett and G. Brassard, "Quantum cryptography: Public key distribution and coin tossing," *Proceedings of IEEE international conference on computers, systems, and signal processing, Bangalore, India*, pp. 175–179, 1984.

[2] E. Knill, R. Laflamme, and G. J. Milburn, "A scheme for efficient quantum computation with linear optics," *Nature*, vol. 409, pp. 46–52, 2001.

[3] H. J. Kimble, M. Dagenais, and L. Mandel, "Photon antibunching in resonance fluorescence," *Phys. Rev. Lett.*, vol. 39, pp. 691–695, 1977.

[4] F. Diedrich and H. Walther, "Nonclassical radiation of a single stored ion," *Phys. Rev. Lett.*, vol. 58, pp. 203–206, 1987.

[5] T. Baschè, E. W. Moerner, M. Orrit, and H. Talon, "Photon antibunching in the fluorescence of a single dye molecule trapped in a solid," *Phys. Rev. Lett.*, vol. 69, pp. 1516–19, 1992.

[6] P. Michler, A. Imamoglu, M. D. Mason, P. J. Carson, G. F. Strouse, and S. Buratto, "Quantum correlation among photons from a single quantum dot at room temperature," *Nature*, vol. 406, pp. 968–970, 2000.

[7] C. Kurtsiefer, S. Mayer, P. Zarda, and H. Weinfurter, "Stable solid-state source of single photons," *Phys. Rev. Lett.*, vol. 85, pp. 290–293, 2000.

[8] A. Kuhn, M. Hennrich, and G. Rempe, "Deterministic single-photon source for distributed quantum networking," *Phys. Rev. Lett.*, vol. 89, p. 067901, 2002.

[9] C. W. Chou, S. V. Polyakov, A. Kuzmich, and H. J. Kimble, "Single-photon generation from stored excitation in an atomic ensemble," *Phys. Rev. Lett.*, vol. 92, p. 213601, 2004.

[10] C. K. Hong and L. Mandel, "Experimental realization of a localized one-photon state," *Phys. Rev. Lett.*, vol. 56, pp. 58–60, 1986.

[11] S. Fasel, O. Alibart, S. Tanzilli, P. Baldi, A. Beveratos, N. Gisin, and H. Zbinden, "High-quality asynchronous heralded single-photon source at telecom wavelength," *New J. Phys.*, vol. 6, p. 163, 2004.

[12] G. Brassard, N. Lütkenhaus, T. Mor, and B. C. Sanders, "Limitations on practical quantum cryptography," *Phys. Rev. Lett*, vol. 85, pp. 1330–33, 2000.

[13] W. Hwang, "Quantum key distribution with high loss: Toward global secure communication," *Phys. Rev. Lett*, vol. 91, p. 057901, 2003.

[14] H. K. Lo, X. Ma, and K. Chen, "Decoy state quantum key distribution," *Phys. Rev. Lett*, vol. 94, p. 230504, 2005.

[15] T. Schmitt-Manderbach, H. Weier, M. Fürst, R. Ursin, F. Tiefenbacher, T. Scheidl, J. Perdigues, Z. Sodnik, C. Kurtsiefer, J. G. Rarity, A. Zeilinger, and H. Weinfurter, "Experimental demonstration of free-space decoy-state quantum key distribution over 144 km," *Phys. Rev. Lett.*, vol. 98, p. 010504, 2007.

[16] A. Beveratos, R. Brouri, T. Gacoin, A. Villing, J. P. Poizat, and P. Grangier, "Single photon quantum cryptography," *Phys. Rev. Lett.*, vol. 89, p. 187901, 2002.

[17] E. Waks, K. Inoue, C. Santori, D. Fattal, , J. Vuckovic, G. S. Solomon, and Y. Yamamoto, "Secure communication: Quantum cryptography with a photon turnstile," *Nature*, vol. 420, p. 762, 2002.

[18] P. W. Shor, "Polynormial-time algorithms for prime factorization and discrete algorithms on a quantum computer," *SIAM. J. Comput.*, vol. 26, pp. 1484–1509, 1997.

[19] L. K. Grover, "Quantum mechanics helps in searching for a needle in a haystack," *Phys. Rev. Lett.*, vol. 79, pp. 325–328, 1997.

[20] J. Cirac, P. Zoller, H. J. Kimble, and H. Mabuchi, "Quantum state transfe and entanglement distribution among distant nodes in a quantum network," *Phys. Rev. Lett.*, vol. 78, pp. 3221–23, 1997.

[21] C. Braig, P. Zarda, C. Kurtsiefer, and H. Weinfurter, "Experimental demonstration of complementarity with single photons," *App. Phys. B*, vol. 76, pp. 113–116, 2003.

[22] N. Schlosser, G. Reymond, I. Protsenko, and P. Grangier, "Sub-poissonian loading of single atoms in a microscopic dipole trap," *Nature*, vol. 411, pp. 1024–27, 2001.

[23] M. Weber, J. Volz, K. Saucke, C. Kurtsiefer, and H. Weinfurter, "Analysis of a single-atom dipol trap," *Phys. Rev. A*, vol. 73, p. 043406, 2006.

[24] B. Lounis and W. Moerner, "Single photons on demand from a single molecule at room temperature," *Nature*, vol. 407, pp. 491–493, 2000.

[25] R. Brouri, A. Beveratos, J. P. Poizat, and P. Grangier, "Photon anti-bunching in the fluorescence of individual color centers in diamond," *Opt. Lett.*, vol. 25, pp. 1294–96, 2000.

[26] T. Gaebel, I. Popa, A. Gruber, M. Domhan, F. Jelezko, and J. Wrachtrup, "Stable single-photon source in the near infrared," *New J. Phys.*, vol. 6, p. 98, 2004.

[27] J. R. Rabeau, Y. L. Chin, S. Prawer, F. Jelezko, T. Gaebel, and J. Wrachtrup, "Fabrication of single nickel-nitrogen defects in diamond by chemical vapor deposition," *Appl. Phys. Lett*, vol. 86, p. 131926, 2005.

[28] C. Wang, C. Braig, C. Kurtsiefer, H. Weinfurter, and B. Burchard, "Single photon emission from SiV centres in diamond produced by ion implantation," *J. Phys. B*, vol. 39, pp. 37–41, 2006.

[29] E. Wu, V. Jacques, H. Zhang, P. Grangier, F. Treussart, and J. F. Roch, "Narrow-band single-photon emission in the near infrared for quantum key distribution," *Opt. Exp.*, vol. 14, pp. 1296–1303, 2006.

[30] J. Kim, O. Benson, H. Kan, and Y. Yamamoto, "A single photon turnstile device," *Nature*, vol. 397, pp. 500–503, 1999.

[31] C. Santori, M. Pelton, G. Solomon, Y. Dale, and Y. Yamamoto, "Triggered single photons from a quantum dot," *Phys. Rev. Lett.*, vol. 86, pp. 1502–05, 2001.

[32] Z. Yuan, B. E. Kardynal, R. M. Stevenson, A. Shields, C. J. Lobo, K. Cooper, N. S. Beattie, D. A. Ritchie, and M. Pepper, "Electrically driven single-photon source," *Science*, vol. 295, pp. 102–105, 2002.

[33] J. Vuckovic, D. Fattel, C. Santori, G. Solomon, and Y. Yamamoto, "Enhanced single-photon emission from a quantum dot in a micropost microcavity," *Appl. Phys. Lett.*, vol. 82, pp. 3596–98, 2003.

[34] D. Englund, D. Fattel, E. Wakes, G. Solomon, B. Zhang, T. Nakaoka, Y. Arakawa, Y. Yamamoto, and J. Vuckovic, "Controlling the spontaneous emission rate of single quantum dots in a two-dimensional photonic crystal," *Phys. Rev. Lett.*, vol. 95, p. 013904, 2005.

[35] C. Santori, D. Fattel, J. Vuckovic, G. Solomon, and Y. Yamamoto, "Indistinguishable photons from a single-photon device," *Nature*, vol. 419, pp. 594–597, 2002.

[36] M. Keller, B. Lange, K. Hayasaka, W. Lange, and H. Walther, "Continuous generation of single photons with controlled waveform in an ion-trap cavity system," *Nature*, vol. 431, pp. 1075–78, 2004.

[37] M. Fleischhauer, A. Imamoglu, and J. P. Marangos, "Electromagnetically induced transparency: Optics in coherent media," *Rev. Mod. Phys.*, vol. 77, pp. 633–673, 2005.

[38] M. D. Eisaman, A. André, F. Massou, M. Fleischhauer, A. S. Zibrov, and M. D. Lukin, "Electromagnetically induced transparency with tunable single-photon pulses," *Nature*, vol. 438, pp. 837–841, 2005.

[39] T. B. Pittman, B. C. Jacobs, and J. D. Franson, "Heralded single photon from pulsed parametric down-conversion," *Opt. Com.*, vol. 246, pp. 545–550, 2005.

[40] A. Zaitsev, "Vibronic spectra of impurity-related optical centers in diamond," *Phys. Rev. B*, vol. 61, pp. 12909–22, 2000.

[41] H. Fearn and R. Loudon, "Theory of two-photon interference," *J. Opt. Soc. Am. B*, vol. 6, pp. 917–927, 1989.

[42] C. Cohen-Tannoudji, J. Dupont-Roc, and G. Grynberg, *Photons and Atoms: Introduction to Quantum Electrodynamics*. Wiley-Interscience, New York, 1989.

[43] R. Loudon, *The Quantum Theory of Light*. Oxford University Press, New York, 2000.

[44] R. J. Glauber, "The quantum theory of optical coherence," *Phys. Rev.*, vol. 130, pp. 2529–39, 1963.

[45] R. Hanbury Brow and R. Q. Twiss, "A new type of interferometer for use in radio astronomy," *Phil. Mag.*, vol. 45, pp. 663–682, 1954.

[46] R. Hanbury Brown and R. Q. Twiss, "Correlation between photons in two coherent beams of light," *Nature*, vol. 177, pp. 27–29, 1956.

[47] L. Mandel and E. Wolf, *Optical coherence and quantum optics.* Cambridge University Press, Cambridge, 1995. chap.17.

[48] C. C. Hong, Z. Y. Ou, and L. Mandel, "Measurement of subpicosecond time intervals between two photons by interference," *Phys. Rev. Lett.*, vol. 59, pp. 2044–47, 1987.

[49] A. Dräbenstedt, L. Fleury, C. Tietz, F. Jelezko, S. Kilin, A. Nizovtev, and J. Wrachtrup, "Low-temperature microscopy and spectroscopy on single defect centers in diamond," *Phys. Rev. B*, vol. 60, pp. 11503–08, 1999.

[50] H. Sternschult, K. Thonke, R. Sauer, P. C. Münzinger, and P. Michler, "1.681-ev luminescence center in chemical-vapor-deposited homoepitaxial diamond films," *Phys. Rev. B*, vol. 50, pp. 14554–60, 1994.

[51] J. E. Field, ed., *The Properties of Natural and Synthetic Diamond.* Academic Press, London, 1992.

[52] R. H. Wentorf, "Diamond growth rate," *J. Phys. Chem.*, vol. 75, pp. 1833–37, 1971.

[53] S. Matsumoto, Y. Sato, M. Tsutsumi, and N. Setaka, "Growth of diamond particles from methane-hydrogen gas," *J. Mater. Sci.*, vol. 17, pp. 3106–12, 1982.

[54] M. Kamo, Y. Sato, S. Matsumoto, and N. Setaka, "Diamond synthesis from gas phase in microwave plasma," *J. Crystal Growth*, vol. 62, pp. 642–44, 1983.

[55] P. K. Bachmann and H. Lydtin, "Characterization of plasma processes," *Mater. Res. Soc. Symp. Proc.*, vol. 165, p. 181, 1990.

[56] P. W. May, "CVD diamond - a new technology for the future?," *Endeavour Magazine*, vol. 19, pp. 101–06, 1995.

[57] H. Okushi, "High quality homoepitaxial CVD diamond for electronic devices," *Diam. Rel. Mater.*, vol. 10, pp. 281–88, 2001.

[58] K. Hayashi, Y. Yokota, T. Tachibana, K. Kobashi, J. Achard, A. Gicquel, C. Olivero, M. Castex, and A. Treshchalov, "Temporal response of UV sensors made of highly oriented diamond films by 193 and 313 nm laser pulses," *Diam. Relat. Mater.*, vol. 10, pp. 1794–98, 1991.

[59] S. Koizumi, K. Watanabe, M. Hasegawa, and H. Kanda, "Ultraviolet emission from a diamond pn junction," *Science*, vol. 292, pp. 1899–1901, 2001.

[60] K. Okano, S. Koizumi, S. R. P. Silva, and G. A. J. Amaratunga, "Low-threshold cold cathodes made of nitrogen-doped chemical-vapour-deposited diamond," *Nature*, vol. 381, pp. 140–41, 1996.

[61] H. Umezawa, K. Tsugawa, S. Yamanaka, D. Takeuchi, H. Okushi, and H. Kawarada, "High-performance diamond metal-semiconductor field-effect transistor with 1 μm gate length," *Jpn. J. Appl. Phys.*, vol. 38, pp. 1222–1224, 1999.

[62] T. N. Rao and A. Fujishima, "Recent advances in electrochemistry of diamond," *Diam. Relat. Mater.*, vol. 9, pp. 384–89, 2000.

[63] K. Iakoubovskii, *Optical Study of Defects in Diamond*. PhD thesis, Catholic University of Leuven, Belgium, 2000.

[64] T. Evans and Z. Qi, "The kinetics of the aggregation of nitrogen atoms in diamond," *Proc. R. Soc. A*, vol. 381, pp. 159–178, 1982.

[65] J. Wagner, C. Wild, and P. Koidl, "Resonance effects in raman scattering from polycrystalline diamond films," *Appl. Phys. Lett.*, vol. 59, pp. 779–781, 1991.

[66] J. H. N. Loubser and J. A. van Wyk, "Electron spin resonance in the study of diamond," *Rep. Prog. Phys.*, vol. 41, pp. 1201–48, 1978.

[67] J. Wrachtrup and F. Jelezko, "Processing quantum information in diamond," *J. Phys.: Condens. Matter*, vol. 18, pp. S807–S824, 2006.

[68] J. Walker, "Optical absorption and luminescence in diamond," *Rep. Prog. Phys.*, vol. 42, pp. 1605–59, 1979.

[69] M. Lax and E. Burstein, "Infrared lattice absorption in ionic and homopolar crystals," *Phys. Rev.*, vol. 97, pp. 39–52, 1955.

[70] G. S. Woods, J. A. van Wyk, and A. T. Collins, "The nitrogen content of type Ib synthetic diamond," *Phil. Mag. B*, vol. 62, pp. 589–95, 1990.

[71] G. Davies, *Properties and Growth of Diamond*. INSPEC, The Institution of Electrical Engineers, London, 1994. EMIs Data Review Series.

[72] G. Davies and M. F. Hamer, "Optical studies of the 1.945 ev vibronic band in diamond," *Proc. R. Soc. A*, vol. 348, pp. 285–98, 1976.

[73] K. Iakoubovskii, G. J. Adriaenssens, and M. Nesladek, "Photochromism of vacancy-related centres in diamond," *J. Phys.: Condens. Matter*, vol. 12, pp. 189–99, 2000.

[74] A. T. Collins, "The Fermi level in diamond," *J. Phys.: Condens. Matter*, vol. 14, pp. 3743–50, 2002.

[75] F. Jelezko, T. Gaebel, I. Popa, A. Gruber, and J. Wrachtrup, "Observation of coherent oscillations in a single electron spin," *Phys. Rev. Lett*, vol. 92, p. 076401, 2004.

[76] J. F. Prins, "Ion implantation of diamond for electronic applications," *Semicond. Sci. Technol.*, vol. 18, pp. S27–S33, 2003.

[77] P. Olivero, S. Rubanov, P. Reichart, B. C. Gibson, S. T. Huntington, J. Rabeau, A. D. Greentree, J. Salzman, D. Moore, D. N. Jamieson, and S. Prawer, "Ion-beam-assisted lift-off technique for three-dimensional micromachining of freestanding single-crystal diamond," *Adv. Mater.*, vol. 17, pp. 2427–30, 2005.

[78] J. Lindhard, M. Scharff, and H. E. Schiøtt, "Range concepts and heavy ion ranges," *Mat. Fys. Medd. Dan. Vid. Selsk.*, vol. 33, no. 14, pp. 1–42, 1963.

[79] S. Eichler, *Untersuchung zu leerstellenartigen Kristalldefekten nach Ionenimplantationen in Halbleitern.* PhD thesis, Martin-Luther-Universität Halle-Wittenberg, Germany, 1998.

[80] S. P. Ahlen, "Theoretical and experimental aspects of the energy loss of relativistic heavily ionizing particles," *Rev. Mod. Phys.*, vol. 52, pp. 121–173, 1980.

[81] R. Kalish, "Ion implantation in diamond; damage, annealing and doping," in *The Physics of Diamond* (A. Paoletti and A. Tucciarone, eds.), pp. 373–409, IOS Press, Amsterdam, 1997.

[82] J. P. Biersack and L. G. Haggmark, "A Monte Carlo computer program for the transport of energetic ions in amorphous targets," *Nucl. Instrum. Methodes*, vol. 174, pp. 257–69.

[83] C. Uzan-Saguy, C. Cytermann, R. Brener, V. Richter, M. Shaanan, and R. Kalish, "Damage threshold for ion-beam induced graphitization of diamond," *Appl. Phys. Lett.*, vol. 67, pp. 1194–96, 1995.

[84] J. O. Orwa, K. W. Nugent, D. N. Jemieson, and S. Prawer, "Raman investigation of diamond caused by deep ion implantation in diamond," *Phys. Rev. B*, vol. 62, pp. 5461–72, 2000.

[85] W. Lukosz, "Optical systems with resolving powers exceeding the classical limit," *J. Opt. Soc. Am.*, vol. 56, pp. 1463–72, 1966.

[86] S. Meyer, "NV Zentren als Einzel-Photon-Quelle," Master's thesis, Ludwig-Maximilians-Universität München, 2000.

[87] L. Kaminska, "Efficiency Measurement and Time Jitter Measurement of APDs with Down Converted Photons," Master's thesis, Ludwig-Maximilians-Universität München, 2007.

[88] C. Braig, "Festkörperbasierte Einzelphotonenquelle," Master's thesis, Ludwig-Maximilians-Universität München, 2001.

[89] S. Reynaud, "Resonance fluorescence - the dressed atom approach," *Ann. Phys. (Paris)*, vol. 8, pp. 315–370, 1983.

[90] E. Hecht, *Optik.* Oldenbourg Verlag, München Wien, 2001.

[91] V. S. Vavilov, A. A. Gippius, A. M. Zaitsev, B. V. Derjaguin, B. V. Spitsyn, and A. E. Aleksenko, "Investigation of the cathodoluminescence of epitaxial diamond films," *Sov. Phys. Semicond.*, vol. 14, pp. 1078–79, 1981.

[92] L. H. Robins, L. P. Cook, E. N. Farabaugh, and A. Feldman, "Cathodoluminescence of defects in diamond films and particles grown by hot-filament chemical-vapor deposition," *Phys. Rev. B*, vol. 39, pp. 13367–77, 1989.

[93] J. A. Freitas, J. E. Butler, and U. Strom, "Photoluminescence studies of polycrystalline diamond films," *J. Mater. Res.*, vol. 5, pp. 2502–06, 1990.

[94] J. Ruan, W. J. Choyke, and W. D. Partelow, "Si impurity in chemical vapor deposited diamond films," *Appl. Phys. Lett.*, vol. 58, pp. 295–97, 1991.

[95] G. Davies, S. C. Lawson, A. T. Collins, A. Mainwood, and S. J. Sharp, "Vacancy-related centers in diamond," *Phys. Rev. B*, vol. 46, pp. 13157–70, 1992.

[96] A. T. Collins, M. Kamo, and Y. Sato, "A spectroscopic study of optical centers in diamond grown by microwave-assisted chemical vapor deposition," *J. Mater. Res.*, vol. 5, pp. 2507–14, 1990.

[97] A. T. Collins, L. Allers, C. J. H. Wort, and G. A. Scarsbrook, "The annealing of radiation damage in De Beers colorless CVD diamond," *Diam. Relat. Mater.*, vol. 3, pp. 932–35, 1994.

[98] C. D. Clark, H. Kanda, I. Kiflawi, and G. Sittas, "Silicon defects in diamond," *Phys. Rev. B*, vol. 51, pp. 16681–88, 1995.

[99] J. P. Goss, R. Jones, S. J. Breuer, P. R. Briddon, and S. Öberg, "The twelve-line 1.682 ev luminescence center in diamond and the vacancy-silicon complex," *Phys. Rev. Lett.*, vol. 77, pp. 3041–44, 1996.

[100] S. W. Brown and S. C. Rand, "Site symmetry analysis of the 738 nm defect in diamond," *J. Appl. Phys.*, vol. 78, pp. 4069–75, 1995.

[101] K. Iakoubovskii and A. Stesmans, "Chemical vapour desposition diamond studied by optical and electron spin resonance techniques," *J. Phys.: Condens. Matter*, vol. 14, pp. R467–99, 2002.

[102] J. E. Field, ed., *The Properties of Diamond*. Academic Press, London, 1979.

[103] T. Feng and B. D. Schwartz, "Characteristics and origin of the 1.681 eV luminescence center in chemical-vapor-deposited diamond films," *J. Appl. Phys.*, vol. 73, pp. 1415–25, 1993.

[104] A. V. Turukhin, C. H. Liu, A. A. Gorokhovsky, R. R. Alfano, and W. Philips, "Picosecond photoluminescence decay of Si-doped chemical-vapor-deposited diamond films," *Phys. Rev. B*, vol. 54, pp. 16448–51, 1996.

[105] K. Iakoubovskii and G. J. Adriaenssens, "Optical detection of defect centers in CVD diamond," *Diam. Relat. Mater.*, vol. 9, pp. 1349–56, 2000.

[106] C. Wang, "Festkörperbasierte Einzelphotonenquelle," Master's thesis, Ludwig-Maximilians-Universität München, 2001.

[107] J. F. Ziegler, P. Biersack, and U. Littmark, *The Stopping and Range of Ions in Solids.* Pergamon Press, New York, 1984.

[108] S. M. Mansfield and G. S. Kino, "Solid immersion microscope," *Appl. Phys. Lett.*, vol. 57, pp. 2615–16, 1990.

[109] A. Beveratos, R. Brouri, T. Gacoin, J. P. Poizat, and P. Grangier, "Nanclassical radiation from diamond nanocrystals," *Phys. Rev. A*, vol. 64, p. 061802, 2001.

[110] B. D. Terris, H. J. Mamin, D. Rugar, W. R. Studenmund, and G. S. Kino, "Near-field optical data storage using a solid immersion lens," *Appl. Phys. Lett.*, vol. 65, pp. 388–90, 1994.

[111] L. P. Ghislain, V. B. Elings, K. B. Crozier, S. R. Manalis, S. C. Minne, K. Wilder, G. S. Kino, and C. F. Quate, "Near-field photolithography with a solid immersion lens," *Appl. Phys. Lett.*, vol. 77, pp. 501–03, 1999.

[112] Q. Wu, R. D. Grober, D. Gammon, and D. S. Katzer, "Imaging spectroscopy of two-dimensional excitons in a narrow GaAs/AlGaAs quantum well," *Phys. Rev. Lett.*, vol. 83, pp. 2652–55, 1999.

[113] Q. Wu, G. D. Feke, R. D. Grober, and L. P. Ghislain, "Realization of numerical aperture 2.0 using a gallium phosphide solid immersion lens," *Appl. Phys.. Lett.*, vol. 75, pp. 4064–66, 1999.

[114] A. A. Gippius, "Luminescent characterization of radiation damage and impurities in ion-implanted natural diamond," *Diam. Relat. Mater.*, vol. 2, pp. 640–45, 1993.

[115] S. Prawer and R. Kalish, "Ion-beam-induced transformation of diamond," *Phys. Rev. B*, vol. 51, pp. 15711–22, 1995.

[116] V. A. Martinovich, A. V. Turukhin, A. M. Zaitsev, and A. A. Gorokhovsky, "Photoluminescence spectra of xenon implanted natural diamonds," *J. Luminescence*, vol. 102-103, pp. 785–90, 2003.

[117] S. A. Solin and A. K. Ramdas, "Raman spectrum of diamond," *Phys. Rev. B*, vol. 1, pp. 1687–98, 1970.

[118] J. H. N. Loubser and W. P. van Ryneveld, "Electron spin resonance of nickel in synthetic diamonds," *Nature*, vol. 211, p. 517, 1996.

[119] V. A. Nadolinny, A. P. Yelisseyev, J. M. Baker, M. E. Newton, D. J. Twitchen, S. C. Lawson, O. P. Yuryeva, and B. N. Feigelson, "A study of ^{13}C hyperfine structure in the EPR of nickel-nitrogen-containing centres in diamond and correlation with their optical properties," *J. Phys.: Condens. Matter*, vol. 11, pp. 7357–76, 1999.

[120] A. M. Zaitsev, *Optical Properties of Diamond: A Data Handbook.* Springer-Verlag, Berlin Heidelberg, 2001.

[121] J. Meijer, B. Burchard, M. Domhan, C. Wittmann, I. Gaebel, T.and Popa, F. Jelezko, and J. Wrachtrup, "Generation of single colour centers by focussed nitrogen implantation," *Appl. Phys. Lett.*, vol. 87, p. 261909, 2005.

[122] J. Meijer, T. Vogel, B. Burchard, I. W. Rangelow, L. Bischoff, J. Wrachtrup, M. Domhan, F. Jelezko, W. Schnitzler, S. Schulz, K. Singer, and F. Schmidt-Kaler, "Concept of deterministic single ion doping with sub-nm spatial resolution," *Appl. Phys. A*, vol. 83, pp. 321–27, 2006.

[123] S. Tomljenovic-Hanic, M. J. Steel, C. Martijn de Sterke, and J. Salzman, "Diamond based photonic crystal microcavities," *Opt. Exp.*, vol. 14, pp. 3556–62, 2006.

[124] Y. Nishibayashi, Y. Ando, H. Saito, T. Imai, T. Hirao, and K. Oura, "Anisotropic etching of a fine column on a single crystal diamond," *Diam. Rel. Mater.*, vol. 10, pp. 1732–35, 2001.

[125] Y. S. Park, A. K. Cook, and H. Wang, "Cavity QED with diamond nanocrystals and silica microspheres," *arXiv:cond-mat/0608493v1*, 2006.

[126] H. Drexler, D. Leonard, W. Hansen, J. P. Kotthaus, and P. M. Petroff, "Spectroscopy of quantum levels in charge-tunable InGaAs quantum dots," *Phys. Rev. Lett.*, vol. 73, pp. 2252–55, 1994.

publications

Single photon emission from SiV centres in diamond produced by ion implantation
C. Wang, C. Kurtsiefer, H. Weinfurter and B. Burchard
J. Phys. B **39**, 37 (2006)

Ultra short luminescence lifetime of ruby nanocrystal inclusions in Ib diamond
C. Wang, C. Kurtsiefer and H. Weinfurter
Proceeding of 10th microoptics conference, L-38 (2004)

Acknowledgments